Source, evolution, and properties of non-Parker-spiral IMF and its role on geomagnetic activity

by

Xiangyun Zhang

A dissertation submitted in partial fulfillment
of the requirements for the degree of
Doctor of Philosophy
(Atmospheric, Oceanic and Space Sciences)
in The University of Michigan
2015

Doctoral Committee:

Professor Mark Moldwin, Chair
Associate Professor Susan T. Lepri
Professor Michael W. Liemohn
Assistant Professor Benjamin W. Longmier
Research Associate Professor Ward B. Manchester IV

For Mom and Dad:

Thanks for being my biggest supporters.

This is for you.

ACKNOWLEDGEMENTS

I would never have been able to finish my dissertation without the guidance of my committee members, help from friends, and support from my family.

I would like to express my deepest gratitude to my advisor, Prof. Mark Moldwin, for his excellent guidance, caring, patience, and providing me with an excellent atmosphere for doing research. I would like to thank Dr. John Steinberg and Dr. Ruth Skoug, who let me experience the research of freashwater mussels in the field and issues beyond my own scope. I would also like to thank Prof. Lepri, Prof. Liemohn, Prof. Longmier and Prof. Manchester for guiding my process of accomplishing the dissertation and helping me to develop my knowledge in other fields.

Many thanks to Shasha Zou, Jie Zhu, Shaosui Xu, Xianjing Liu, Yuxi Chen, Zhenguang Huang, and the Moldwin's group members for helping me to practice the oral presentation and providing me greatly valuable suggestions throughout the years of my graduate life in Michigan. Many thanks to Fang Fang, Xing Meng, Meng Jin, Chunpeng Wang, and other colleagues in AOSS department for giving me selfless help whenever I was in difficulty. My research and life would not have been possible without their helps.

I would also like to thank all my family members, especially my parents and my fiance. They have always been supporting me and encouraging me with their best wishes.

TABLE OF CONTENTS

LIST OF FIGURES

Figure

ABSTRACT

Source, evolution, and properties of non-Parker-spiral IMF and its role on geomagnetic activity

by

Xiangyun Zhang

Chair: Mark Moldwin

The most important driver of geomagnetic activity has been shown to be out of ecliptic or non-Parker-spiral interplanetary magnetic field (IMF), especially large-amplitude and long-duration (LALD) southward IMF. However, neither current solar/heliospheric models provide accurate forecasts of IMF Bz component, nor they provide them at all. This thesis combines in situ observations of magnetic field, plasma, and ion composition with remote sensing measurements of solar features as well as predictive modeling of the solar wind and IMF to understand the source, evolution and properties of IMF Bz. We find that the integrated duration and number of Bs-events follow the sunspot number when Bz < -5 nT. We suggest that the emergence of the non-Parker-spiral is not the result of random fluctuations of the solar wind or IMF. We also find the major contribution to the LALD IMF Bs events is from solar wind transients (ICME, SIR, Alfvénic fluctuations), and that the low-latitude coronal hole (LLCH) with nearby solar activity in the closed magnetic field configuration is the solar source of CIR with LALD IMF Bs intervals. We analyze the correlation between the LALD IMF Bs-events and geomagnetic activity indices and

find that the strongest storms and substorms are not associated with the same type of event, and noted that great Bs events (Bz < -10 nT, t > 3 hrs) do not always induce large storms. We also point out that MC, ejecta, and SIR drive storms in different ways, and that while Alfvénic Bs-events are relatively weak in triggering geomagnetic storms, they are possible drivers for large-scale ULF wave oscillations in the Earth's magnetosphere. We also show that the probabilistic forecasting technique provides a tool for predicting the occurrence rate of geomagnetic activity based on a combination of solar wind quantities, obtainable from either measurements or models. We finally propose that the evolution of the active region adjacent to the LLCH, and the geometric parameters of the LLCH are important to determine the intensity of the IMF Bs intervals observed at 1 AU, which could be used to improve the current space weather forecasting.

CHAPTER I

Introduction

1.1 The solar wind and the interplanetary magnetic field (IMF)

The solar wind is a stream of charged particles that flows outward from the Sun's upper atmosphere. The Sun's outer layer - corona - is very hot, with a temperature of a million degrees, so the thermal particles move very fast. The particles with enough energy to escape the Sun form the solar wind (*Parker*, 1965). *Parker* (1958) developed a set of equations to describe the distribution of solar wind in the heliosphere and found that one of the two viable solutions was a plasma outflow which became supersonic after a critical point, and asymptotically approached a constant speed. The other solution is in the form of a subsonic solar breeze moving with decreasing speed with distance. However, the supersonic solution was then confirmed to be consistent with observations from Mariner 2 spacecraft in 1962 (*Neugebauer and Snyder*, 1966).

The Sun has a magnetic field and rotates every 27 days on the equator plane; the field lines emanating from the Sun are connected to the solar surface and also rotate. The extension of the solar magnetic field into the interplanetary medium can

be understood in terms of the magnetic induction equation (1.1):

$$\frac{\delta \mathbf{B}}{\delta t} = \bigtriangledown \times (\mathbf{u} \times \mathbf{B}) \tag{1.1}$$

(Here we neglected the diffusion term, since the effects of interparticle collisions are negligible in this case.) In the coordinate system corotating with the Sun, neglecting the differential rotation of the Sun, we obtain (' denotes parameter in corotating frame) Equation1.2

$$\frac{D_{\odot}\mathbf{B}}{D_{\odot}t} = \bigtriangledown \times (\mathbf{u}' \times \mathbf{B}) \tag{1.2}$$

If we consider a situation when the total time derivative of the magnetic field vector vanished in the corotating frame of reference, $D_{\odot}/D_{\odot}t = 0$. This corresponds to a steady-state axially symmetric physical situation. Using this assumption, we obtain Equation1.3

$$\bigtriangledown \times (\mathbf{u}' \times \mathbf{B}) = \mathbf{0} \tag{1.3}$$

One of the few basic physics principles for solar wind studies is the concept a 'frozen-in' magnetic field, which is formed because when you look at the dynamics of this interplanetary plasma, there is about as much energy density (pressure) in the gas component as there is in the magnetic field component, with the scales tipped in favor of the gas. This means that the gas drags the magnetic field around, and the magnetic field mostly follows after the gas as it flows out from the sun. Considering the solution for the solar wind velocity in the corotating frame is ${u_r}' = u_{sw}$, ${u_\phi}' = -\Omega_{\odot} r sin\Theta$, and that the magnetic field is consistent in different frames under non-relativistic

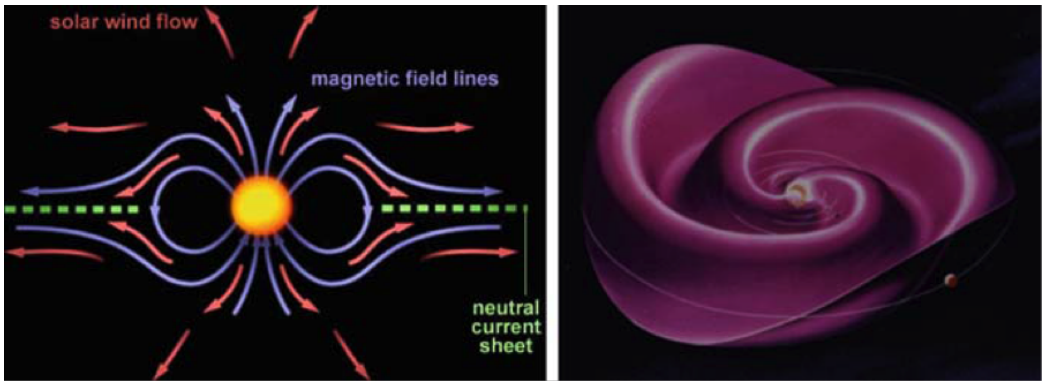

Figure 1.1: As the solar wind moves outward, the magnetic field is stretched so that a current sheet forms between the inward and the outward field lines (left panel). The rotation of the Sun causes the field lines to spiral outward and the tilt of the solar wind field causes the current sheet to move up and down (right panel). (*Richardson and Cane*, 2010)

transformation, the solution for magnetic field lines is Equation1.4

$$\mathbf{B} = \mathbf{B}_{\odot}\left(\frac{\mathbf{R}_{\odot}}{\mathbf{r}}\right)^{\mathbf{2}}\left[\mathbf{e_r} - (\mathbf{r}-\mathbf{R}_{\odot})\frac{\mathbf{\Omega}_{\odot}\mathbf{sin\Theta}}{\mathbf{u_{sw}}}\mathbf{e}_{\phi}\right]. \tag{1.4}$$

The magnetic field lines are stretched by the outflow of the solar wind (Figure 1.1, left panel) so that the heliospheric current sheet (HCS) forms. The HCS separates field lines from north and south of the Sun's magnetic equator; the field lines in these two sectors are in opposite directions, outward in one hemisphere and inward in the other. Since the feet of the field lines are anchored to the Sun and rotate with the Sun, magnetic field lines are swept into a spiral pattern, called the Parker spiral. The tilt of the solar dipole causes the HCS to become wrapped in heliolatitude, forming a wavy surface, which has been compared to a ballerina skirt (Figure 1.1, right panel).

The observation of sunspot numbers for centuries showed that solar activity has an average 11-year cycle (Figure 1.2). As defined, the sunspot number peaks at solar maximum and is the lowest at solar minimum. Since the direction of the Sun's magnetic dipole field changes every solar maximum, the solar cycle, in terms of a magnetic cycle, is with an average duration of 22 years (Figure 1.3). We have been

exploring the heliosphere for almost 50 years using spacecraft and obtained almost continuous observations of solar wind since the early 1970s. In the course of its 19 years of operations (1990 - 2009), the Ulysses spacecraft has completed three polar orbits of the Sun, spanning more than one complete sunspot cycle(Figure 1.4). The first orbit occurred during solar minimum and showed slow wind over the equator and a fast wind over the poles. (*McComas et al.*, 2000) The second orbit showed fast and slow winds at all latitudes, consistent with solar maximum activity. (*McComas et al.*, 2001) Ulysses has completed more than three quarters of the third orbit, shut down around the current solar cycle. Besides the variations of solar wind speed over a solar cycle, the magnitude of the interplanetary magnetic field (IMF) also changes by about a factor of two, peaking near solar maximum. At solar minimum, the solar magnetic field is roughly dipolar and the current sheet is closely aligned with the solar equator, whereas at solar maximum the field is highly tilted and has strong non-dipolar components (Figure 1.5). Table 1 shows average, median, maximum and minimum values of solar wind and IMF parameters measured by the Wind spacecraft near Earth from 1994 to 2007. The solar wind speed varies by almost a factor of 10, density by a factor of 1000, temperature by 500, and IMF strength by 300. Solar wind ions are mostly protons, but He++ is also observed with density ratios ranging from near 0 to 30%.

	Average	Median	Minimum	Maximum
Speed ($\mathrm{km\ s^{-1}}$)	440	415	260	2140
Density ($\mathrm{cm^{-3}}$)	7.3	5.7	0.1	135
Temperature (K)	83,000	69,000	6,000	3,800,000
B (nT)	6.7	5.9	0.26	72
$\mathrm{He^{++}/H^{+}}$ (%)	4.0	4.1	0.1	30

Table 1.1: Solar wind parameters: the average, median, minimum, and maximum values of the solar wind speed, density, temperature, magnetic field magnitude, and alpha/proton ratio observed by wind. (*Richardson and Cane*, 2010)

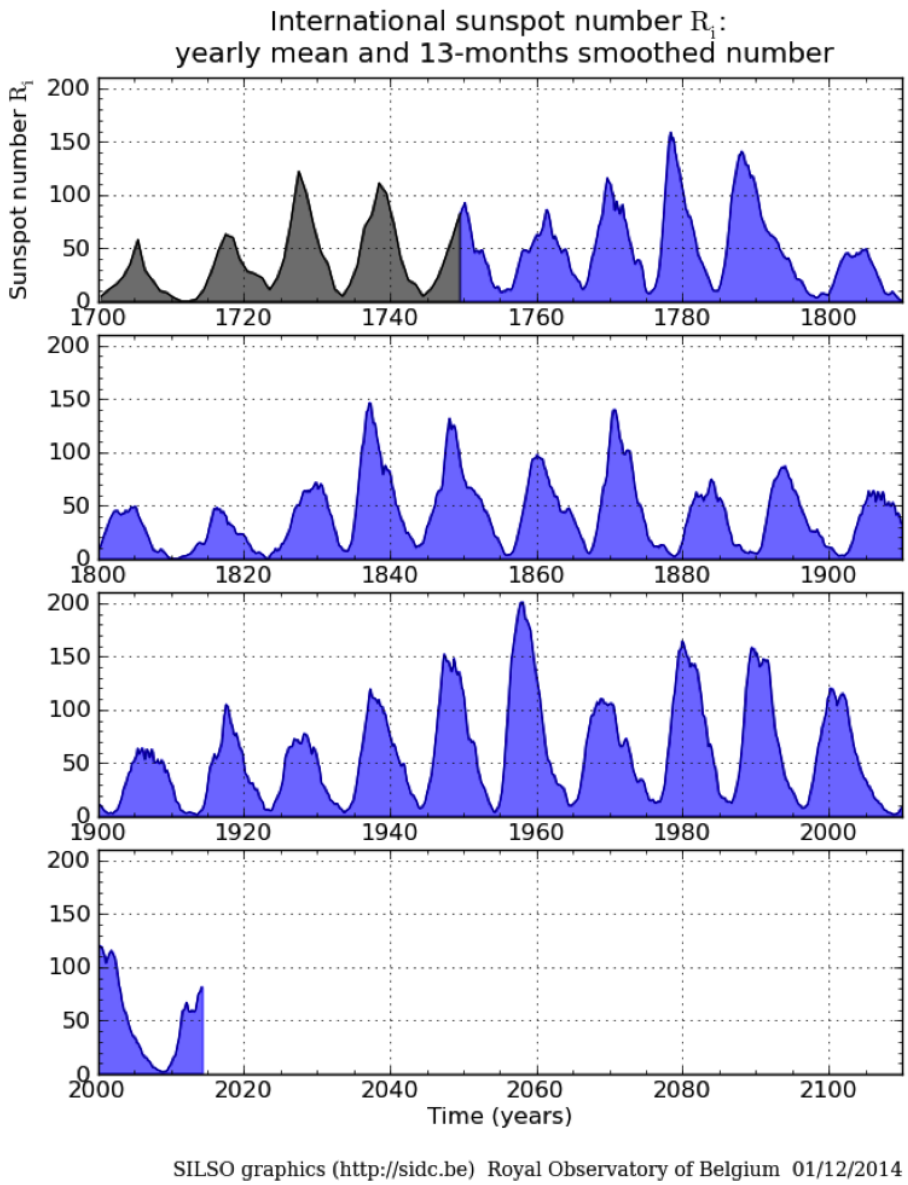

Figure 1.2: Yearly mean sunspot number (black) up to 1749 and monthly 13-month smoothed sunspot number (blue) from 1749 up to the present. [Credits: Sunspot Index and Long-term Solar Observations (SILSO)]

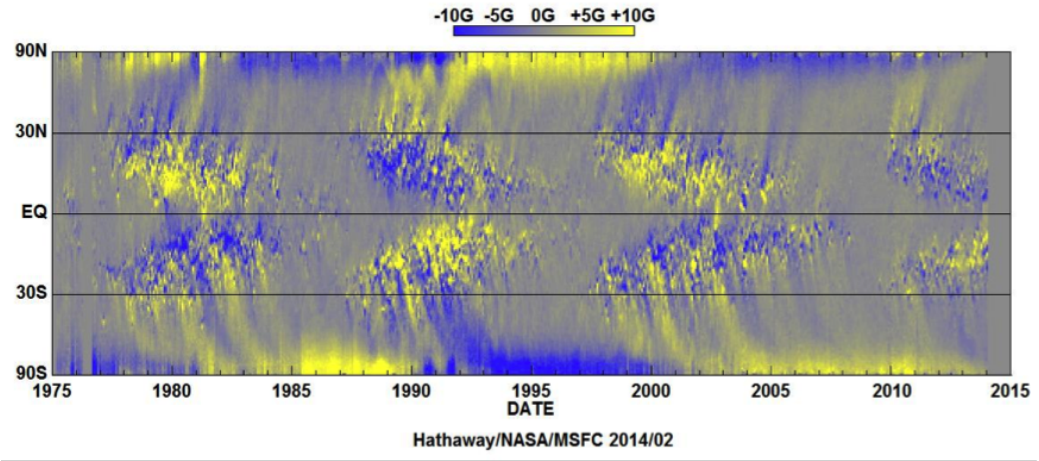

Figure 1.3: Time vs. solar latitude diagram of the radial component of the solar magnetic field, averaged over successive solar rotation. The "butterfly" signature of sunspots is clearly visible at low latitudes. [Credits: NASA]

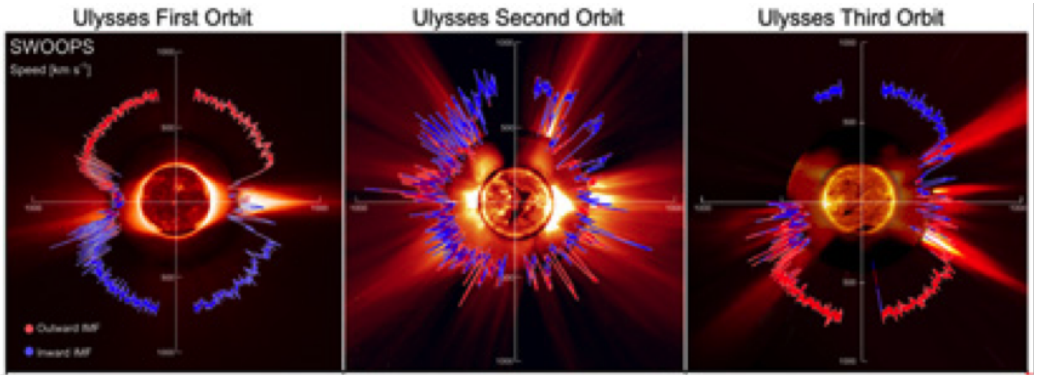

Figure 1.4: Plots of the solar wind speed over all three of Ulysses orbits. [Credits: Southwest Research Institute]

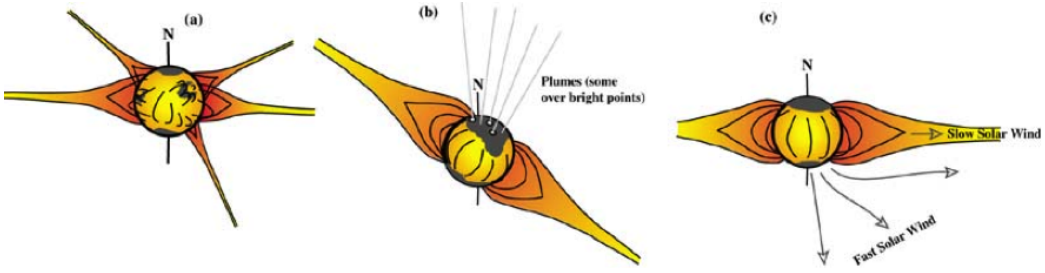

Figure 1.5: Schematic of evolution of the solar corona over the 11-year sunspot cycle. (a) Solar maximum; (b) Declining phase of solar cycle; (c) Solar minimum. [Credits: NASA]

1.2 Solar activity and transient solar wind structures

The corona evolves significantly over a solar cycle in both large and small scales. There is a significantly reduced fast component of the wind and the solar wind is more highly structured at solar maximum, with more active regions and a convoluted streamer belt. This change in the corona proceeds with plasma activity in a broad range of spatial and temporal scales, ranging from the quiescent heating of the corona, through the complex highly nonequilibrium processes of the flare, to a rich variety of mass ejections (*Low*, 1996).

The most important structure from a quiescent corona for space weather issues is the stream interaction region (SIR). SIRs are mainly created when fast solar wind (emanating from a low-latitude coronal hole) interacts with the slow solar wind associated with the HCS plasma sheet during the descending phase of the solar cycle. Coronal holes are areas of open magnetic field lines, with fast streams dominated by large amplitude Alfvén waves. When the polar holes migrate down to lower latitude, the streams emanating from the holes corotate at 27-day intervals as seen at the Earth, which defines the corotating interaction region (CIR), a subcategory of SIR. A schematic of the interplanetary structure of a CIR is given in Figure 1.6. The magnetic fields of the slower speed stream are more curved due to the lower speeds, and the fields of the higher speed stream are more radial because of the higher speeds. The stream interface (SI) is the boundary between the slow and fast stream plasmas and fields. The sunward side of the SI, the flow is high speed and with low density. At large heliospheric distances (> 1.5 AU), where these corotating structures are well developed, the compressions tend to evolve into a forward-reverse shock pair. However, a recent study proposed a different interpretation for intermediate-speed solar wind within CIR as an independent stream produced at the edge between active region and low-latitude coronal hole rather than a result of the corotating interaction between low- and the high-speed stream (*He et al.*, 2010).

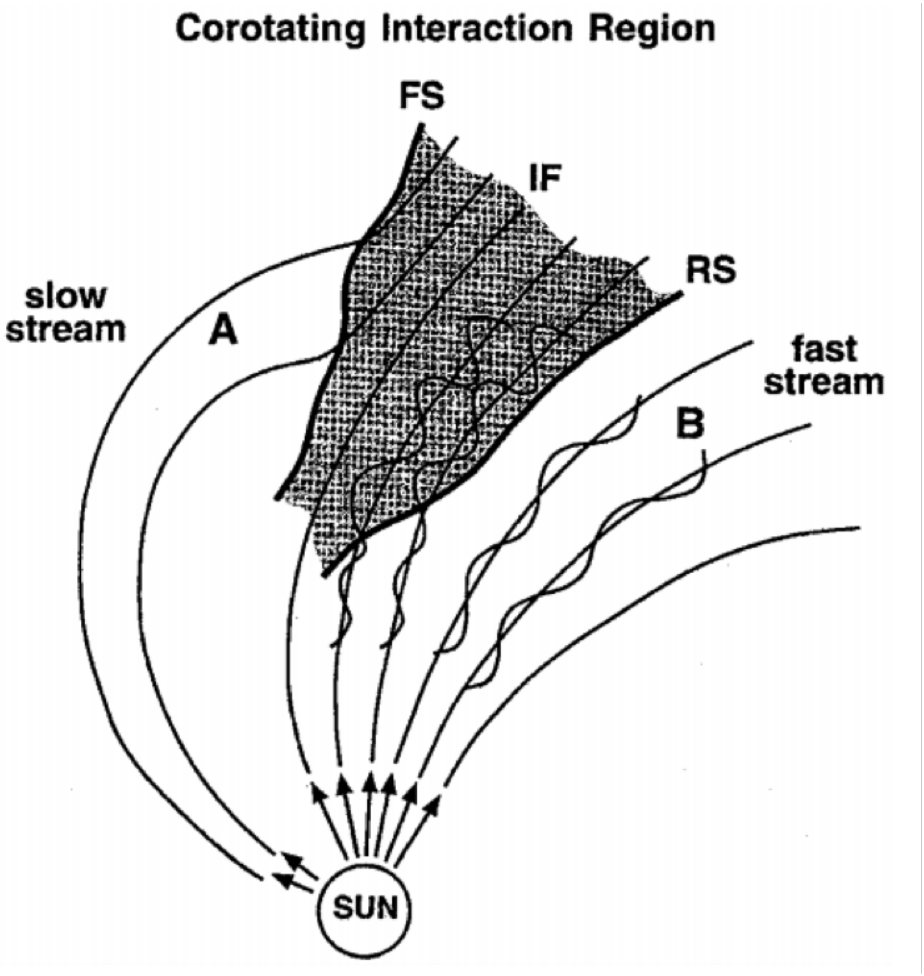

Figure 1.6: Schematic of the formation of corotating interaction regions (CIRs) during the descending phase of the solar cycle. The composition of the plasma and magnetic field fluctuations are also shown. (*Gonzalez et al.*, 1999)

This overall structure was first found in the Pioneer 10 and 11 data and was named CIR by *Smith and Wolf* (1976). CIRs exhibit enhanced densities and magnetic field strengths at their central interface. The trailing high speed solar wind contains large-amplitude Alfvén waves, which can have long duration intervals of southward IMF (*Eastwood et al.*, 2014). An example of a CIR and the effects on the magnetosphere are shown in Figure 1.7. As shown, the magnetic storm main phase is present from ∼0500 UT to ∼2100 UT on 25 January.

Solar eruptions are manifest in several forms, from flares seen across the spectrum (radio to hard X-ray) to organized outflows of plasma, from the corona in the form of filament eruptions to streamer blowouts. Solar eruptions originate most commonly from quiet structures of the Sun, including quiescent filaments and coronal streamers. However, the most energetic eruptions occur from solar active regions. Transient eruptions occur from closed field regions of all sizes, starting from bright points to large active regions. Usually moving features with an angular width of a few degrees or more are known as coronal mass ejections (CMEs), which is one of the most energetic solar activities and has the greatest potential for triggering great disturbance in the geomagnetic field. A CME is an observable expulsion of a coronal structure that (1) erupts on a time scale of a few minutes and several hours and (2) involves the appearance and outward motion of a discrete, bright, white-light feature in the coronagraph field of view (*Hundhausen et al.*, 1984; *Schwenn*, 1996). The modern view of CMEs has broadened considerably as the result of observations made by instruments other than coronagraphs at visual wavelengths. Figure 1.8 shows six different views of CMEs including one historical observation. CMEs originate from regions on the Sun where the magnetic field lines connect opposite polarities. These regions are the active regions and filament regions, where the magnetic field strength is elevated with respect to the quiet Sun. CMEs propagate far into the heliosphere causing observable effects along their path, sometimes all the way to the heliospheric termination

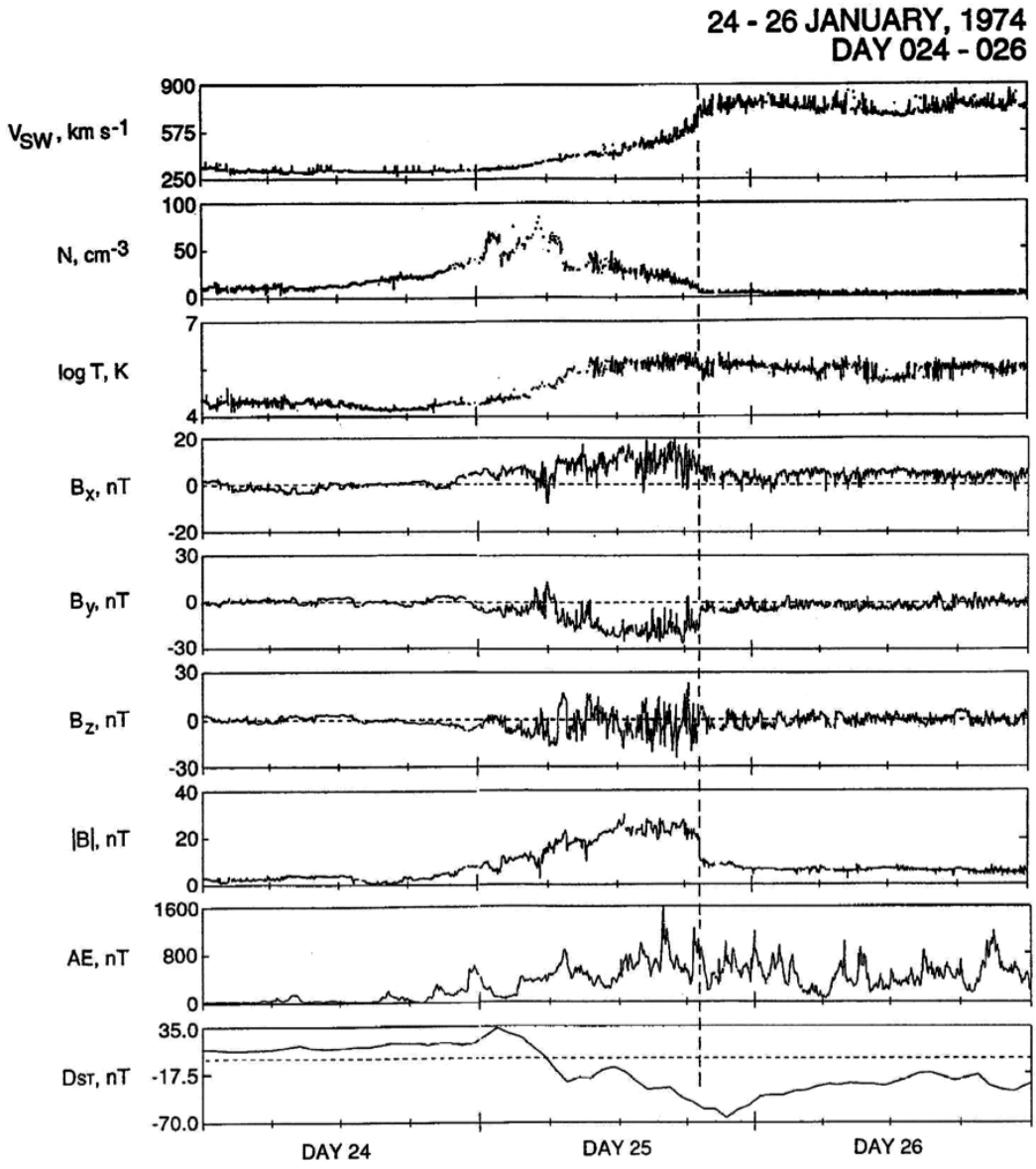

Figure 1.7: A CIR, high-speed stream proper in IMP-8 interplanetary data just upstream of the Earth. The above three interplanetary features are responsible for the magnetic storm initial phase, main phase, and recovery phase, respectively (*Tsurutani et al.*, 2006).

shock. There is still no consensus regarding the mapping of features seen in CME coronagraphic observations with the interplanetary phenomena - interplanetary CME (ICME) (*Forsyth et al.*, 2006), but there are many specific signatures. These range from magnetic clouds (MCs) (*Burlaga et al.*, 1982), with a highly organized flux-rope magnetic pattern, to solar energetic particles (SEPs) (*Cane and Richardson*, 2003; *Klecker et al.*, 2006a). The presence or absence of particular signatures varies from event to event.

The typical CME is made up of a three-part structure - a leading outward moving bright front, followed by a dark cavity, and finally a bright core of filament plasma at its trailing edge (Figure 1.8). It is generally assumed that the bright front corresponds to the sheath of compressed solar wind and the dark cavity comprises the flux rope structure observed in MCs, which also shows what is probably the most obvious signature of the solar origin of ICMEs (*Forsyth et al.*, 2006). Figure 1.9 shows the comparison between the magnetic field structure at the sites of solar prominences and that of interplanetary MCs (*Bothmer and Schwenn*, 1994). However, as mentioned, individual signatures may not be detected in all ICMEs, such as the fine-structure flux rope in IMF data, either because they are not present or as a result of instrumental limitations or data gaps. Several in situ signatures of ICMEs have been extensively discussed in the literature. Figure 1.10 illustrates the schematic of an ICME driving a shock ahead of it with several related in situ features (*Zurbuchen and Richardson*, 2006). Plasma signatures of ICMEs include abnormally low proton and electron temperature (*Richardson and Cane*, 1995; *Montgomery et al.*, 1974, e.g.), and bidirectional suprathermal electron strahls (*Zwickl et al.*, 1983; *Gosling et al.*, 1987, e.g.). In situ compositional anomalies have also been considered as ICME signatures, such as enhanced helium abundance to proton (*Hirshberg et al.*, 1972; *Borrini et al.*, 1982, e.g.), and enhanced Fe charge states (*Fenimore*, 1980; *Lepri et al.*, 2001, e.g.). Another in situ signature of ICMEs is the flux rope-like magnetic fields, identified as

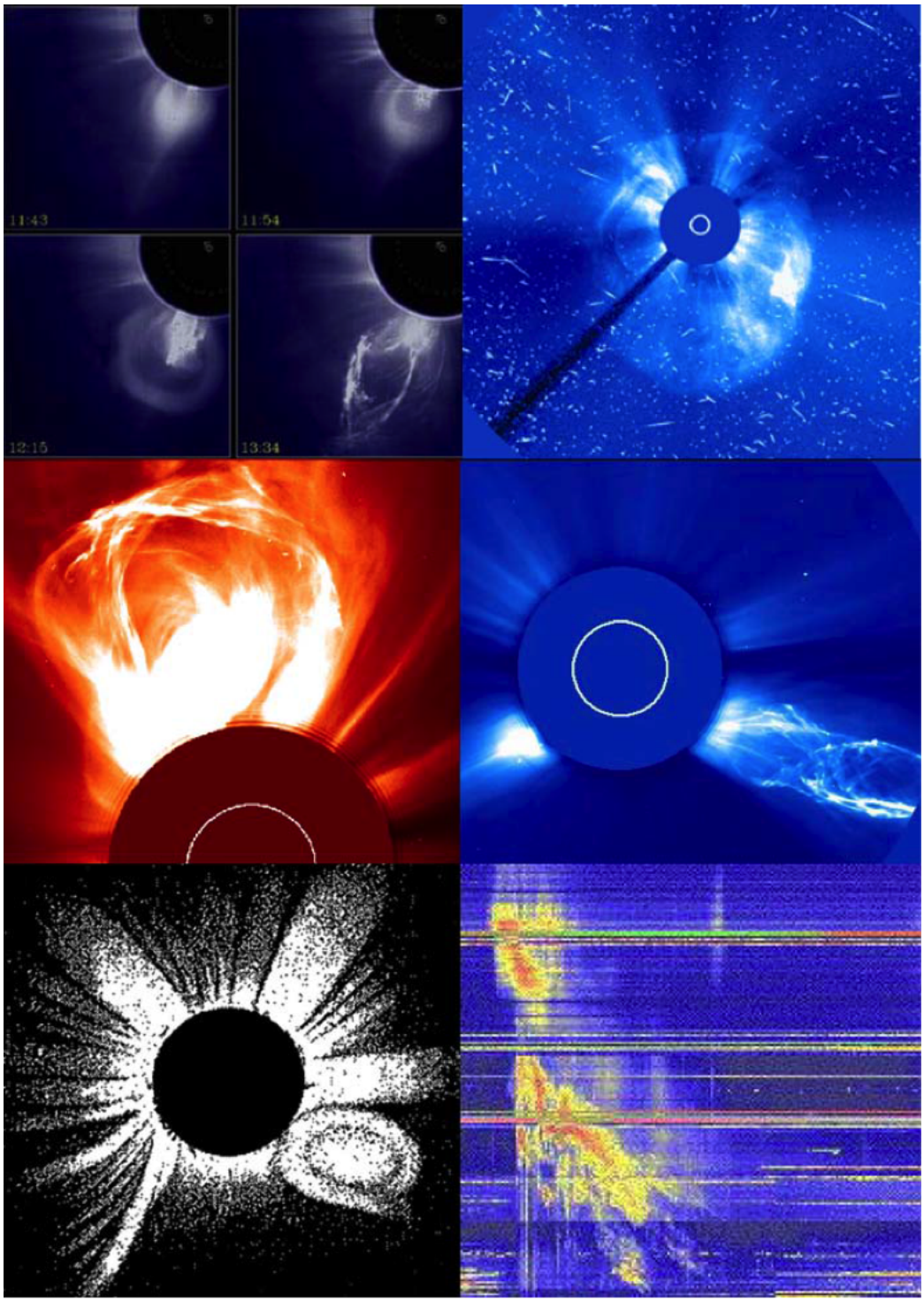

Figure 1.8: Six views of coronal mass ejections. Top: Prototypical 3-part CME as observed by SMM; halo CME from LASCO. Middle: two views of flux-rope CMEs (LASCO). Bottom: Historical eclipse observation of possible CME; type II radio burst (Culgoora spectrogram). (*Hundhausen et al.*, 1984)

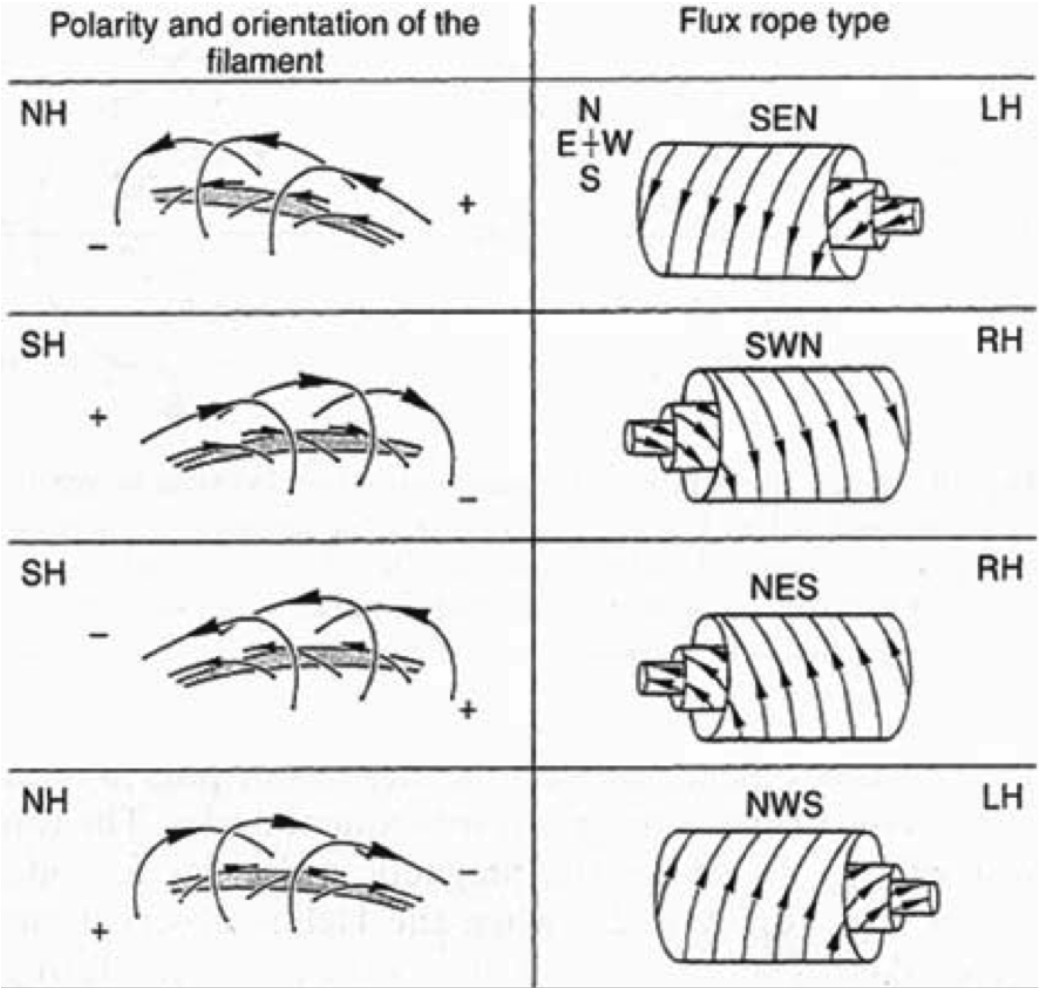

Figure 1.9: Magnetic field structure of solar prominences and magnetic clouds (*Bothmer and Schwenn*, 1994)

enhanced magnetic fields rotating smoothly through a large angle, such as the MC mentioned above. Figure 1.11 shows an example of in situ measurements of plasma, ion composition, and magnetic field for an ICME in October 2000 (*Richardson and Cane*, 2010).

Based on observations for three solar cycles, it has been noted that the fraction of ICMEs with characteristics of MCs is dependent of the solar cycle, with fewer ICMEs around solar minimum having a higher incidence of MCs than ICMEs around solar maximum (*Cane and Richardson*, 2003). The distribution of average ICME parameters and minimum value of the corresponding geomagnetic activity index D_{st}

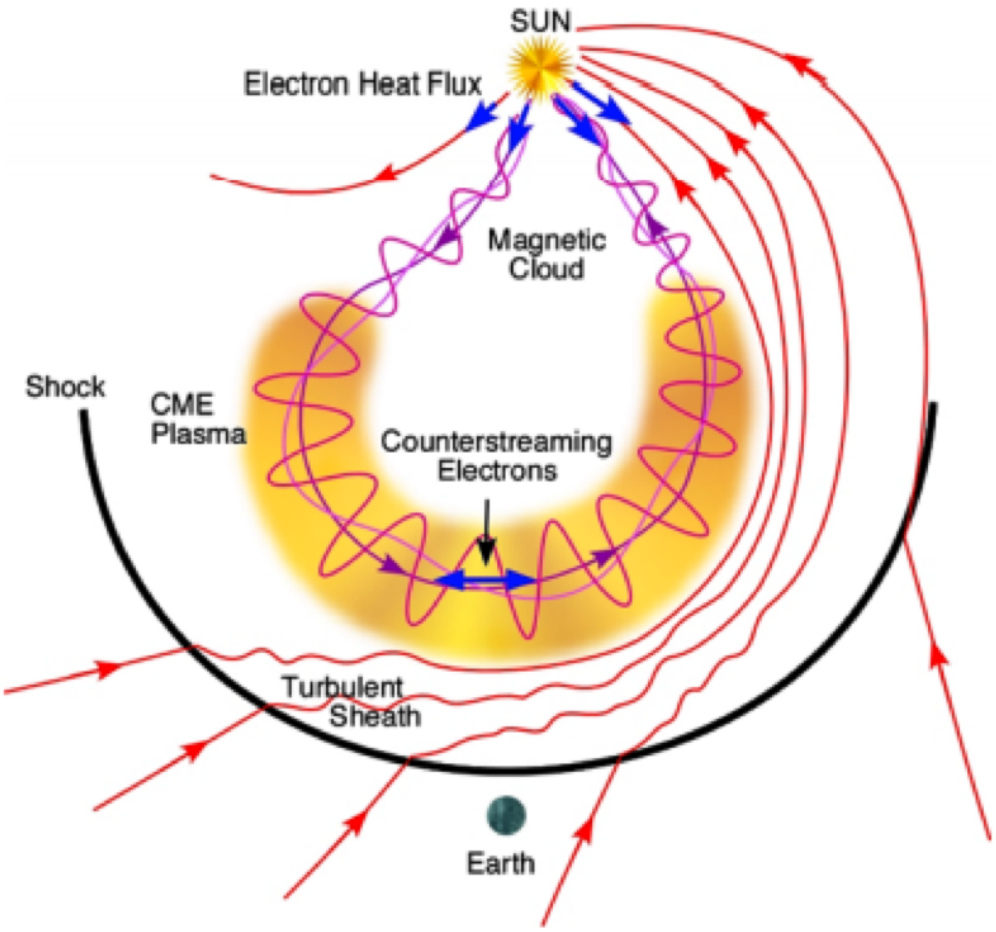

Figure 1.10: Schematic of an ICME and upstream shock indicating magnetic field, plasma and solar wind suprathermal electron flows (*Zurbuchen and Richardson*, 2006).

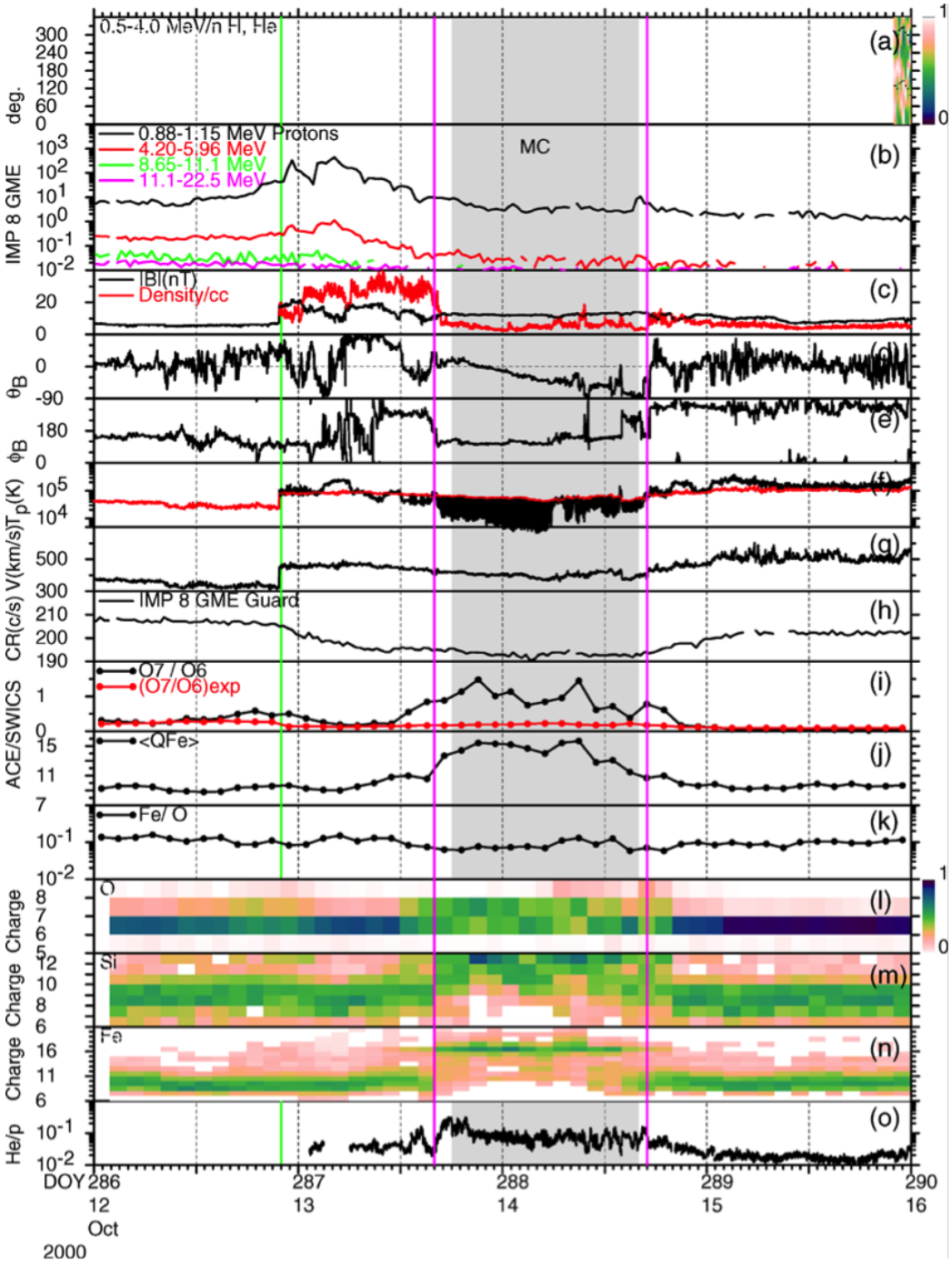

Figure 1.11: Example of an ICME, in October 2000, where the plasma, field and composition/charge state signatures, and reported magnetic cloud (gray shading) are approximately co-located. There are no IMP 8 GME ion distributions (panel (a)) for most of this interval (*Richardson and Cane*, 2010).

for 1996 -2009 is in Figure 1.12. Considering all the ICMEs, the mean magnetic field intensity is 10.0 ± 0.3 nT, compared with 12.6 ± 0.4 nT in MCs and 8.9 ± 0.3 nT in non-cloud ICMEs. Combining with all the results in related literature (*Liu et al.*, 2005; *Wang et al.*, 2005; *Forsyth et al.*, 2006, e.g.), it is reasonable to summarize that MCs have average field strengths around twice the average solar wind values, while non-cloud ICMEs have more modest enhancements, of the order of 30%.

1.3 Alfvénic solar wind

Another feature generated in the solar atmosphere and propagated outward to the interplanetary medium are Alfvénic fluctuations. Alfvénic fluctuations in the solar wind were first observed by (*Coleman*, 1967) based on comparison with an ideal, uniform solar wind model with a wide period range (10^2 to $5*10^4$s in the spacecraft frame). However, it was impossible to distinguish the fast wave mode from Alfvén wave in their study. Soon after, *Unti and Neugebauer* (1968) found a specific example of an Alfvén wave in the interplanetary medium from the Mariner 2 plasma and magnetic field data. *Belcher and Davis* (1969) examined five months of magnetic and velocity field data from Mariner 5, and found that more than 30% of the time with correlation coefficient larger than 0.8 between the absolute value of IMF radial component and the solar wind velocity. They concluded that it was due to large-amplitude, aperiodic Alfvén waves propagating outward from the Sun, with time scale of one hour generally. Following this study, *Coleman and Rosenberg* (1971) did an extensive study of the microscale fluctuations (less than 0.01 AU) in the interplanetary medium from Mariner 5 observations, and showed that large-amplitude, nonsinusoidal, outward propagating Alfvén waves range from 10^3 to $5*10^6$ km in wave-length. They also found that Alfvén waves in slow wind usually have smaller amplitudes than in the fast streams and tend to be more mixed and so suggested that the Alfvén waves in the solar wind are generated in the sub-Alfvénic flow region near the Sun. *Burlaga and*

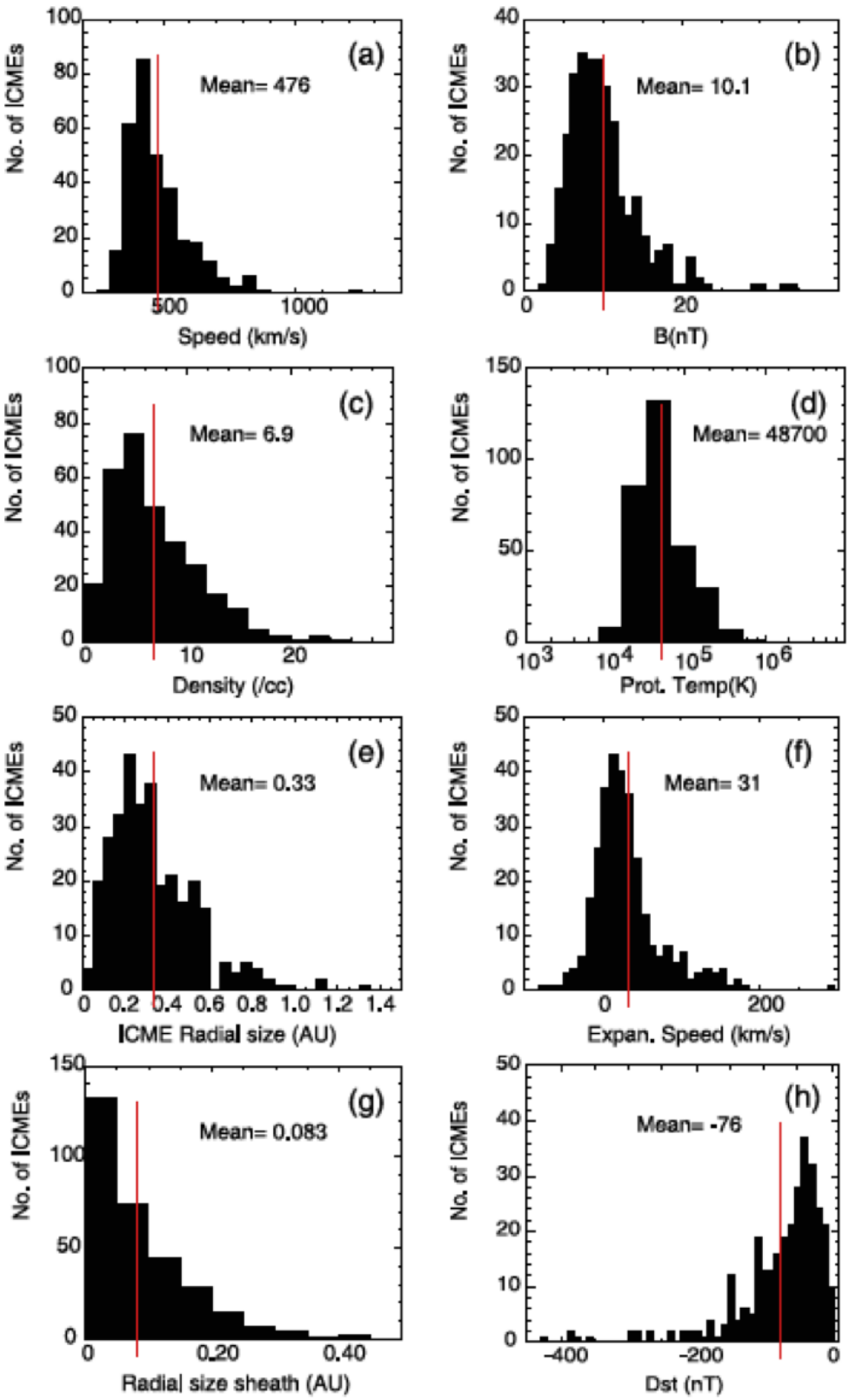

Figure 1.12: Distributions of mean ICME parameters and minimum value of the D_{st} index for 1996 -2009 (*Richardson and Cane*, 2010).

Turner (1976) analyzed the interplanetary plasma and magnetic field fluctuations on a scale of 1 hour from IMP 1 (Explorer 43), revealing that unpure, large amplitude Alfvén waves were observed ∼40% of the time and propagating outward. *Snekvik et al.* (2013) showed in their conference abstract that during Alfvénic intervals, the magnetic field exhibits Alfvénic fluctuations with periods about 1 hour, amplitude of 2-4 nT, and speed over 400 km/s mostly. They found that the occurrence of Alfvénic intervals strongly depends on the solar cycle, with a peak in the early declining phase. Based on the remote sensing observations of lower solar atmosphere, a recent study demonstrated that Alfvénic waves have sufficient energy to power the quiet solar corona and fast solar wind (e.g. *McIntosh et al.*, 2011), which is consistent with the previous results from in situ observations.

Sahraoui et al. (2009) reported the dissipation range of magnetofluid turbulence in the solar wind at the electron scales based on high resolution magnetic and electric field data of the Cluster spacecraft. They found two distinct breakpoints in the magnetic spectrum at 0.4 and 35 Hz, which correspond, respectively, to the Doppler-shifted proton and electron gyroscales. Above electron gyrofrequency, the spectrum has a steeper power law $\sim f^{-4.1}$ down to the noise level of the instrument, and they interpreted this as the dissipation range in agreement with theoretical predictions of a quasi-two-dimensional cascade into Kinetic Alfvén Waves (KAW).

The cross helicity - Alfvén effect ratio - was first suggested as one of the rugged invariants of 3-D ideal incompressible MHD turbulence theory (*Matthaeus and Goldstein*, 1982), which is a measure of the correlation between variations of velocity and magnetic field. Later, they used this quantity to describe the Alfvénicity if the cross helicity is close to unity, the fluctuations of the solar wind are purely Alfvénic, and if it is close to zero, the fluctuations are non-Alfvénic when the interplanetary medium is dominated by the convection of static structures (*Tu and Marsch*, 1993, e.g.). They also showed that as the heliocentric distance increases, the normalized

cross helicity and Alfvénicity decreases, from near 1 at 0.3 AU in high-speed solar wind to substantially less than 0.5 at 1 AU.

Alfvénic fluctuation is another source of southward IMF in the solar wind. (*Borovsky*, 2008) presented a flux tube solar wind model in which the large spread in magnetic field orientations at 1 AU is due to a braiding of magnetic flux tubes about the Parker spiral direction. (*Tian et al.*, 2010) also proposed that Alfvénic fluctuations are observed in periods consistent with flux rope signatures, and defined them as Alfvén wave trains. Some other studies also suggested that turbulence in the solar wind (*Ragot*, 2006) or undamped Alfvén waves (*Burlaga et al.*, 1982) are the source of angular variations of the IMF away from the Parker spiral direction.

1.4 The geomagnetic activity indices and effect of solar wind/IMF variations on geomagnetic field

It is widely accepted that the variations in the upstream solar wind/IMF are external sources for disturbances in the Earth's magnetic field. The primary causes of geomagnetic storms at Earth are strong dawn-to-dusk electric fields associated with the passage of southward directed interplanetary magnetic fields, past the Earth for sufficiently long intervals of time. The solar wind energy transfer mechanism is magnetic reconnection between the IMF and the Earth's magnetic field. As shown in Figure1.13, the plasma flows anti-sunward across the polar cap due to the $\mathbf{E} \times \mathbf{B}$ drift, as required for the field lines to convect from the dayside to the nightside, but then forms return paths on the dusk and dawn sides at lower latitudes. The flow pattern thus has two cells. These return paths give rise to the so-called 'auroral (or convection) ejectrojets' responsible for the magnetic perturbations caused by auroral activity.

Geomagnetic storms are the global disturbances in the Earth's magnetic field

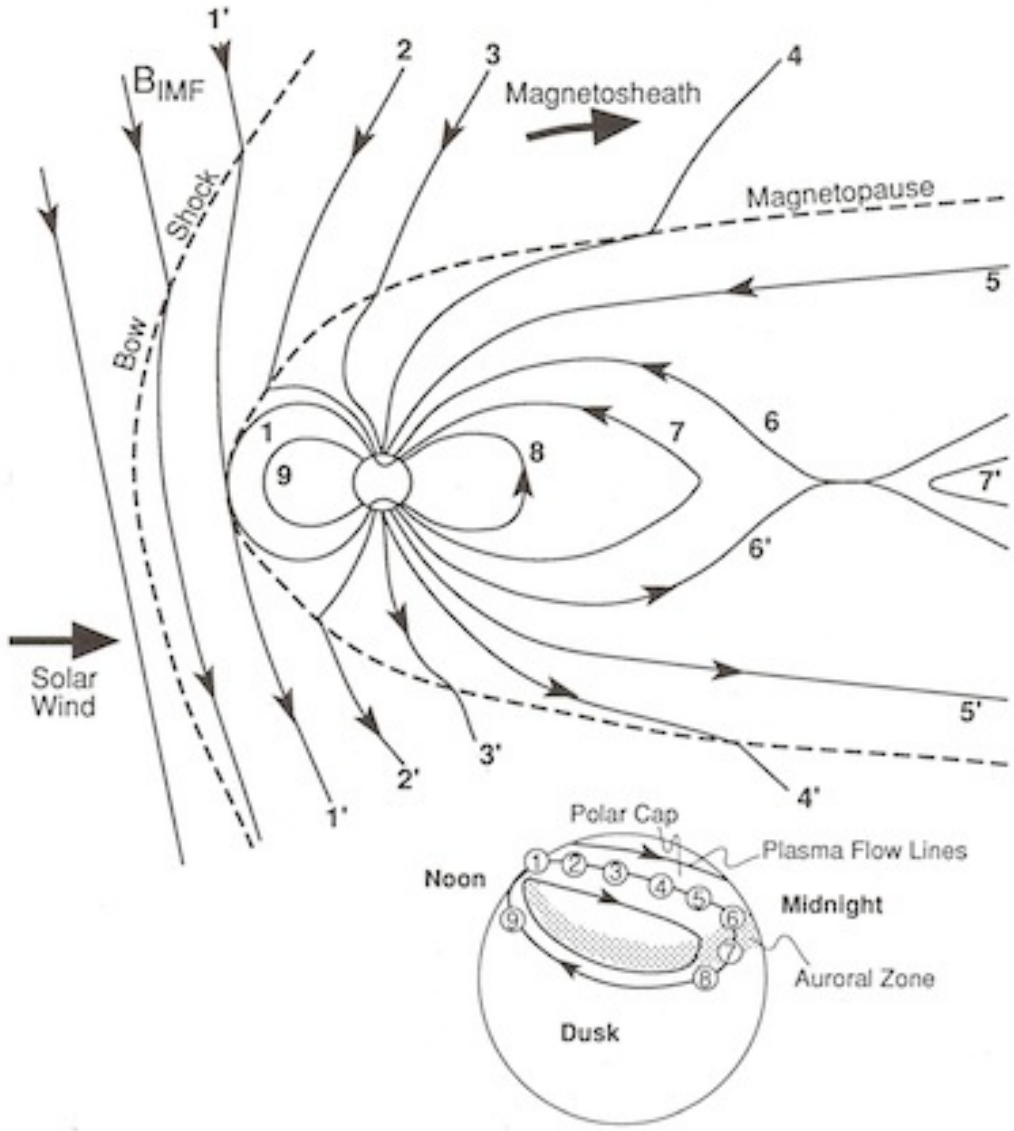

Figure 1.13: Flow of plasma within the magnetosphere (convection) driven by magnetic reconnection at the dayside magnetopause. The numbered field lines show the succession of configurations a geomagnetic field line assumes after reconnection with an IMF field line (1), drag across the polar cap (2-5), reconnection at the x-line in the tail (6), ejection of plasma down the tail and into the solar wind (7'), and the subsequent return of the field line to the dayside at lower latitudes (7-9). (*Kivelson and Russell*, 1995)

that result from the interaction between extreme solar eruptions and the Earth's magnetosphere. Several indices based on satellite and ground measurements quantify the variations of geomagnetic field.

Chapman (1919) demonstrated that for some time after a period of great geomagnetic disturbances, the horizontal component of the magnetic field around the Earth is significantly reduced from its average, by using ground magnetometers. Following studies led to the development of the currently widely used statistical quantity of geomagnetic storm activity the D_{st} index, which was designed to represent the global magnetic field reductions during storms. Four magnetic observatories distant from the auroral and equatorial electrojets and distributed in longitude are usually used for the derivation of the hourly D_{st} index. The D_{st} index represents the axially symmetric disturbance magnetic field at the dipole equator on the Earth's surface. Major disturbances in D_{st} are negative, namely decreases in the geomagnetic field. These field decreases are produced mainly by the equatorial current system in the magnetosphere, usually referred to as the ring current. Positive variations in D_{st} are mostly caused by the compression of the magnetosphere from solar wind pressure increases. (http://wdc.kugi.kyoto-u.ac.jp/D_{st}dir/D_{st}2/onD_{st}index.html) In recent year, a higher-resolution version of D_{st} was created, called SYM-H. The SYM-H index uses different magnetometer stations to calculate the symmetric portion of the horizontal component magnetic field near the equator. Another difference between D_{st} and SYM-H indices comes from the different method to calculate the baseline values. The determination of base value at each station for the hourly D_{st} index takes into account the geomagnetic secular variation while the SYM-H index does not. However, the 1-min resolution SYM-H index responds more timely and clearly to the solar wind dynamic pressure variations.

Another well-known phenomenon in the Earth's magnetic field is the geomagnetic substorm, which is sometimes referred to as magnetospheric substorm or an

auroral substorm. It is a temporal disturbance in the Earth's magnetosphere that causes energy to be released from the tail of the magnetosphere and injected into the high latitude ionosphere. A substorm is usually defined as a sudden brightening and increased movement of auroral arcs from imaging observations (*Akasofu*, 2002). Substorms are distinct from geomagnetic storms in many aspects, such as the triggering mechanisms, the time scales, and related features presented in space and ground measurements. Substorms can cause magnetic field disturbances in the auroral zones up to a magnitude of 1000 nT. To quantify the level of a substorm, the auroral electrojet (AE) index was introduced by *Davis and Sugiura* (1966). The AE index is derived from geomagnetic variations in the horizontal component observed at 10-13 selected observatories along the auroral zone in the northern hemisphere. The related symbols, AU and AL, are respectively defined by the largest and the smallest valued selected from all the stations at each given time. The difference, AU minus AL, finally defines the AE index. The AU and AL indices are intended to express the strongest current intensity of the eastward and westward auroral electrojets, respectively, while the AE index represents the overall activity of the electrojets.

A recently developed index to describe the turbulent variations of the Earth's magnetic field is the ULF wave index. The above mentioned indices - D_{st}, SYM-H, and AE - quantify the energy transport to certain regions of the magnetosphere-ionosphere, however, these indices characterize the level of the electrodynamics of the near-Earth environment. Much of the turbulent nature of plasma processes of solar wind - geomagnetic field interactions can be monitored with ground-based and space observations in the ULF frequency range ($\sim$ 2 - 10 mHz). The first observational evidence of a ULF wave was proposed by *Stewart* (1861), in which he reported quasi-sinusoidal magnetic field oscillations as well as field changes of several hundred nT that occurred on a time scale of a few minutes. The first real understanding of geomagnetic pulsations was put forward by *Dungey* (1954) that the long but regular

periods of these oscillations might be the result of standing Alfvén waves being excited on geomagnetic field lines. An international committee came up with a classification of ULF waves (*Jacobs et al.*, 1964) in which they split ULF waves into classes based on the wave period or frequency, designating by a number - Pc 1-5. The response of magnetospheric ULF waves to solar wind/IMF variations has been extensively studied (*Sanny et al.*, 2002; *Skoug et al.*, 2004; *Sanny et al.*, 2007; *Takahashi and Ukhorskiy*, 2008, e.g.).

The correlation between different kinds of solar wind transients with various plasma/magnetic field conditions and the corresponding geomagnetic response has been analyzed widely using both satellite/ground observations and numerical simulations. Based on the OMNI data of interplanetary measurements for 1976 - 2000, (*Yermolaev et al.*, 2011) analyzed 798 geomagnetic storms with D_{st} <= -50 nT and five different types of solar wind transients (CIR, ICME including MCs and ejecta, and a compression region sheath before both types of ICME), and they found that MCs play a critical role in triggering magnetic storms (higher probability to have an embedded large and long-term southward IMF component) even though they have lower occurrence rates than CIR and sheath. Figure 1.14 shows the schematic of the D_{st} index evolution during an ICME- and CIR- induced geomagnetic storms. (*Tsurutani et al.*, 2006) reviewed the studies about geomagnetic response to CIRs and summarized their cause-effect relationship as follows: the high density plasma region in the vicinity of the HCS in the slow solar wind impinge upon the magnetosphere and create magnetic storm initial phase when D_{st} increases can be higher than those associated with a shock in front of ICMEs; the southward component of the typically rapid Bz fluctuations within the CIRs lead to magnetic storm main phases with weak to moderate intensity (D_{st} > -100 nT) via sporadic magnetic reconnection with the geomagnetic field. Thus some CIRs, without southward IMF, have no effect in changing D_{st}. The recovery phase of CIR-induced magnetic storms can last for a few

days up to 27 days due to the continuous shallow plasma injections into the magnetosphere. The auroras during these intervals are continuous and global auroral zone features, the AE maximum does not mean substorm, but the so-called High Intensity Long Duration Continuous AE Activity (HILDCAA) events. The auroral intensities for HILDCAAs are substantially lower than for substorms (*Guarnieri*, 2005), while they are a global phenomenon, i.e., auroras are present at all local times along the auroral oval.

Pulkkinen et al. (2006) examined two types of storms, one driven by slowly varying MCs and the other driven by the highly fluctuating sheath regions ahead of ICMEs. While the two data sets had comparable solar wind electric field as the storm driver and similar D_{st} minima as the preceding condition, the auroral and inner magnetosphere evolution during the storms were quite different. In the sheath-driven storms, auroral activity begins at storm onset and stays at a relatively constant level until the storm maximum (*Huttunen et al.*, 2002). The MC-driven storms show a much slower increase in auroral activity, with maximum value around the time of D_{st} minimum.

As the Earth's dayside magnetic field is northward, magnetic reconnection (MR) could occur if the impinging IMF has a suitable-magnitude southward component. The ICME with a MC feature usually presents an hourly-scale large-amplitude southward IMF interval, which satisfies the MR condition. One of the effects from the MR between the ICME and the Earth's magnetosphere is that the reconnection process opens the geomagnetic field and connects it with the ICME to provide the passage for the energetic particles in the ICME to deposit into the magnetosphere. Another important influence of the reconnection process is the transfer and release of magnetic energy into the magnetosphere. The overall result is the global extensive disturbance in the magnetosphere-ionosphere system - geomagnetic storm. Besides the MR process that occurs between the magnetic structure within ICME and the magnetosphere, the plasma component of the ICME is also critical for triggering perturbations in the

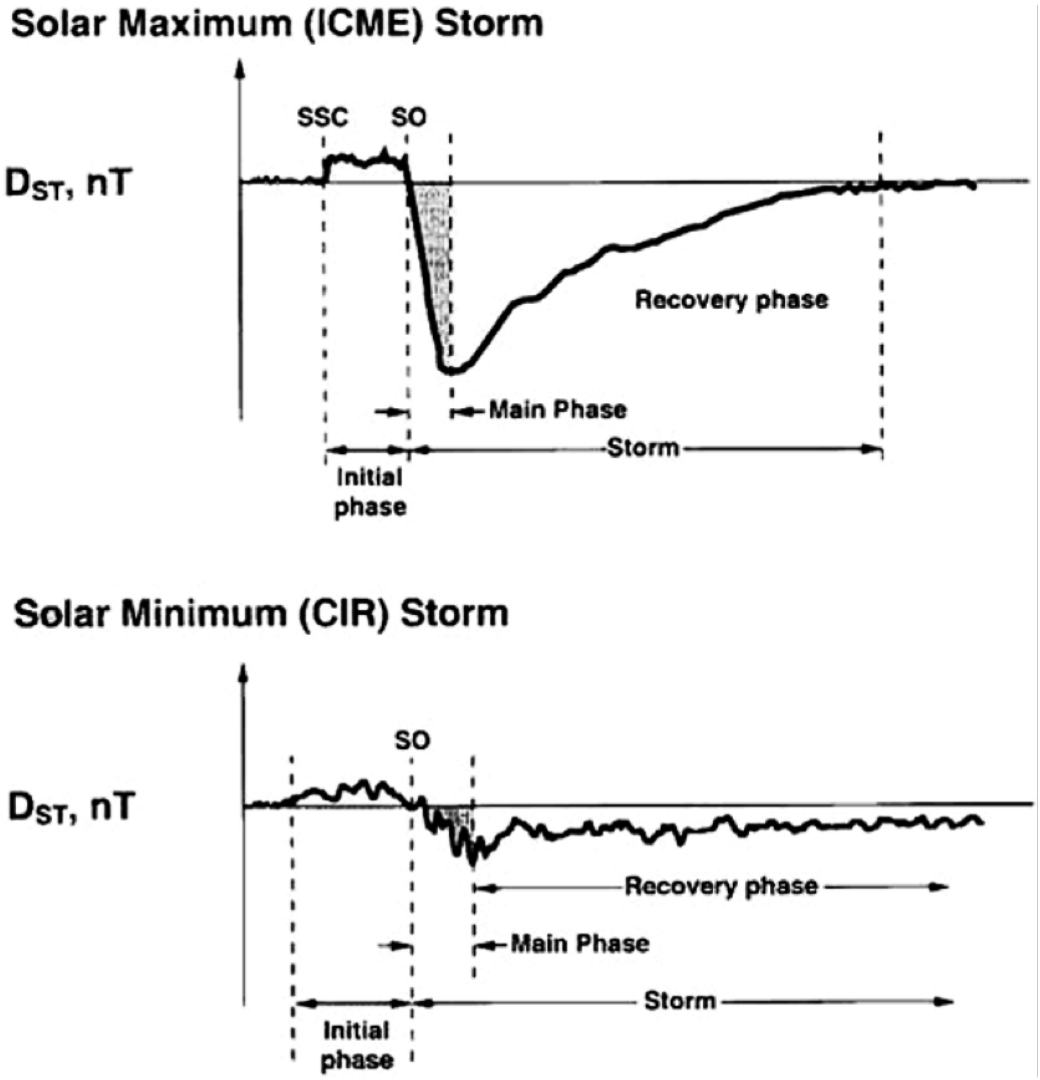

Figure 1.14: Schematic of a magnetic storm generated by an ICME (top) and by a CIR (bottom). Although the profiles of these two different magnetic storms are qualitatively similar, the physical causes and characteristics of the different storm phases are different. The figure is taken from (*Tsurutani*, 2000).

Earth's system. The greatly increased ram pressure because of the increased speed and density (sometimes a shock in the solar wind) within the ICME exerts substantial pressure on the magnetosphere when they interact. This pressure reduces magnetic field lines in size on the dayside, expanding the polar cap and causing the cusp to move further toward the equator, resulting in observed aurora at even lower latitudes and an increase in the area of the ionosphere that is exposed to the solar wind. The condensed and fast solar wind in the shock and sheath region of the ICME will also increase the concentration of energetic particles available to the magnetosphere. The arrival of an interplanetary shock produces the so-called sudden storm commencement (SSC) at the Earth (*Howard*, 2011), shown in Figure 1.14.

Early studies demonstrated that the D_{st} index can be derived from the driving interplanetary electric field using $\frac{dD_{st}{}^*}{dt} = Q(t) - D_{st}{}^*/\tau$, where $D_{st}{}^*$ has been corrected for solar wind dynamic pressure effects by $D_{st}{}^* = D_{st} - b\sqrt{P} + c$ and the source function Q(t) is a linear function of the driver V*Bs (*Burton et al.*, 1975; *O'Brien and McPherron*, 2000). Recently, *Newell et al.* (2007) investigated coupling functions to represent the interaction between the solar wind and the magnetosphere, comparing more than 20 candidate solar wind coupling functions and ten variables that measure the state of the magnetosphere. They found that the function $d\Phi_{MP}/dt = v^{4/3}{B_T}^{2/3}sin^{8/3}(\frac{\theta_c}{2})$ (θ_c is the IMF clock angle defined by $\theta_c = arctan(\frac{By}{Bz})$), which characterizes the rate magnetic flux is opened at the magnetopause, shows to be the best correlated function with 9 out of 10 indices of magnetospheric activity, except for D_{st}. Later, *Borovsky* (2008) derived and tested a formula that expresses the dayside reconnection rate in terms of upstream solar wind parameters - Bm (the magnetic field strength in the magnetosphere), Bs (the magnetic field strength in the magnetosheath), ρ_m (the plasma mass density in the magnetosphere), and $\rho_s heath$ (the plasma mass density in the magnetosheath), and an IMF clock-angle dependence. Based on the analysis of this function, a solar wind control function was derived as

$$R = 0.4{\mu_0}^{1/2} sin\left(\frac{\theta}{2}\right) \rho_0 {v_0}^2 (1 + 0.5{M_{ms}}^{-2})(1 + \beta_s)^{-1/2} \left[C\rho_0 + (1 + {\beta_s}^{-1/2})\right]^{-1/2} \left[(1 + \beta_s)^{1/2} + 1\right]^{-1/2} \quad (1.5)$$

where $\beta_s = 3.2 * 10^{-2} {M_A}^{1.92}$, $C = [(1/4)^6 + (1/(1 + 1.38 log_3(M_A)))^6]^{-1/6}$, $M_{ms} = v_0 \left[({B_0}^2/(\mu_0\rho_0)) + 5P_0/3\rho_0\right]^{1/2}$, $M_A = v_0(\mu_0\rho_0)^{1/2}/B_0$.

Although a lot of studies are still being carried out to determine a better solar wind driving function to predict the level of geomagnetic activity, the importance of southward component of IMF has been demonstrated in all of the different formulations.

1.5 Current status and limitation of measurements and space weather forecasting

The conditions in the near-Earth space environment that may affect space-borne or ground-based technological systems and may threaten human life are referred to as space weather. As the utilization of space has become part of our everyday life, and as our lives have become increasingly dependent on technological systems, the understanding and forecasting of hazards caused by solar transients have dramatically grown in importance. Forecasting space weather is to describe the state of the space environment at a future time based on its current status and our accumulated knowledge of the correlation between relevant phenomena, which is a great challenge (*Schwenn et al.*, 2005; *Weigel et al.*, 2006). This is because, in addition to formulating and implementing a test of a model or theory, it is constrained by limited information to issue a predictive statement (*Vassiliadis et al.*, 2007).

Figure 1.15 shows the current operating and upcoming missions that are designed as observatories for the heliophysics system, primarily in the space between the Sun

and the Earth. The various instruments onboard these NASA spacecraft provide real-time science data to space weather forecasts. Examples include ACE measurements of interplanetary conditions from the Lagrangian point L1 where objects are never shadowed by the Earth or the Moon; CME alerts from SOHO; STEREO beacon images of the far side of the Sun; and super high-resolution images from SDO. On the other hand, the satellites inside the Earth's magnetosphere, such as Cluster, THEMIS, and Van Allen Probes, are monitoring the current status of the Earth's space environment. Although we have made great achievements in the technologies in space weather monitoring since the first International Geophysical Year (IGY) in 1957, we are still substantially constrained by the limited access to the information about the real-time space environment conditions due to the fact that we can not launch as many mission as would be desirable. For instance, it is hard to put any other satellite on the line between the Sun and Earth except for the only stable L1 point, which prevents us from studying the radial evolution of the interplanetary medium all the way from the Sun to the Earth. Though solar sail technology may allow expanded radial coverage, we could not send a satellite to the near-Sun region, which leaves us little knowledge about the in situ conditions of the solar atmosphere - the source of almost everything for space weather.

Not only has spacecraft technological development been utilized to improve the capability of space weather forecasting, but also global numerical models have been carried out to mimic the process of space weather events. The Community Coordinated Modeling Center (CCMC, $http://ccmc.gsfc.nasa.gov/$) provides access to modern space science simulations; it also supports the transition to space weather operations from these models. The CCMC models are primarily categorized into five groups based on the targeted regions - solar, heliosphere, magnetosphere, inner magnetosphere, and ionosphere. Models in each group are performed under specific conditions and some different assumptions from other models - not any one of the

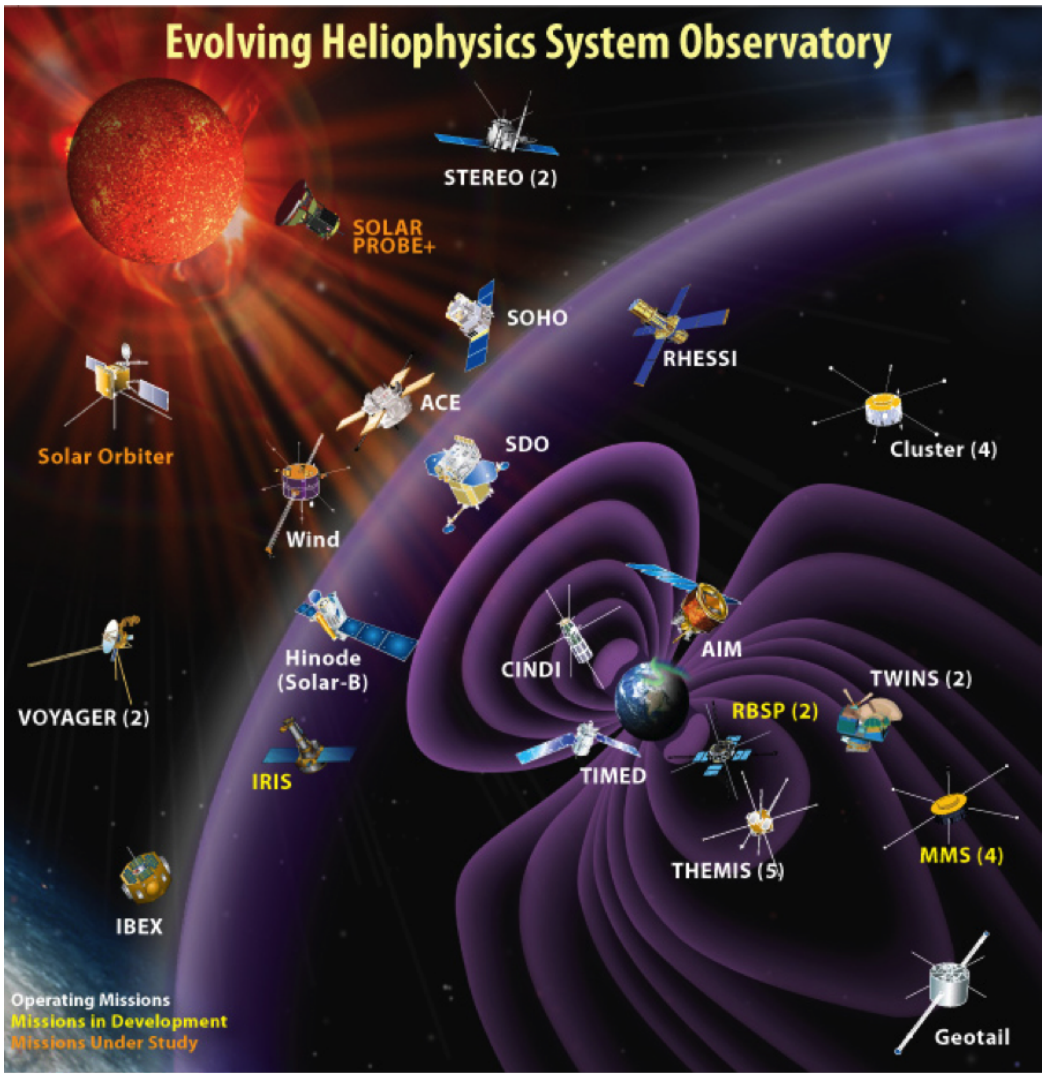

Figure 1.15: The Heliophysics System Observatory (HSO) showing current operating missions, missions in development, and missions under study. [Credit: NASA]

models works in a universal environment. The combination of the models from different groups to simulate the process of an integrated space weather event is also quite a challenge due to the difficulty of exchanging the boundary conditions and achieving a self-consistent system as a whole. Based on satellite and ground-based observations, as well as empirical models and numerical simulations, NOAA's Space Weather Prediction Center (SWPC) provides warnings and forecasts of geophysical activity and the verification statistics and other forecast quality information of these products - Joint USAF/NOAA Report of Solar and Geophysical Activity, 3-day Space Weather Forecast, as well as short-term warning of the substantial geomagnetic events. However currently, the accuracy of space weather forecasting, even for large solar eruptions, e.g., flares and CMEs, and their impacts on the Earth's magnetosphere are still poor (*Watermann et al.*, 2009b,a). Although we still need to make great efforts to improve the predictability of these space weather forecasting models, there have been results demonstrating the causal relationship between solar activity, solar wind variations and Earth's magnetospheric disturbances. (*Lopez et al.*, 2004; *Palmroth et al.*, 2003; *Tóth et al.*, 2007, e.g.)

The knowledge of the relationship between other solar wind/IMF parameters and southward IMF is important to understand their source on the Sun and their propagation through the interplanetary medium, and also key to improve the forecasting ability of the IMF Bz component based on simulating the other parameters in current solar/heliospheric models. The knowledge of how different combinations of solar wind conditions affect the Earth's magnetosphere is also important to understand the physical mechanisms that drive geomagnetic activity to improve heliosphere-magnetosphere modeling and to enhance the ability of space weather prediction based on in situ observations.

1.6 Thesis review

This thesis provides a comprehensive picture of the source, evolution, and geo-effectiveness of the southward component of the interplanetary magnetic field (IMF Bs), especially its relationship with solar wind transients, from the view of in situ observations, theory and statistical analysis methods.

Chapter 2 presents the first systematic analysis of the IMF Bs intervals identified by the observational occurrence constrained by preset thresholds. Based on the in situ measurements from Helios, Ulysses, WIND, ACE, and STEREO spacecraft as well as solar activity index, the statistical properties of large-amplitude, long-duration (LALD) southward IMF events are investigated, including the correlation with sunspot number, in situ plasma and magnetic field characteristics.

Chapter 3 focuses on identifying the sources of LALD southward IMF events by comparing with the literature and re-examination of the well-known features about the solar wind transients. The potential sources of the LALD southward IMF events not discussed in the literature have been proposed by analyzing the in situ and remote sensing observations, where the back mapping method has been used.

Chapter 4 shows the relationship between the LALD southward IMF events and geomagnetic activity indices. Statistical methods, such as linear regression, and superposed epoch analysis, have been utilized to investigate correlation between the solar wind and IMF parameters directly measured or derived from the observations at 1 AU and the geomagnetic storm - SYM-H, geomagnetic substorm - AE indices. The ultra low frequency (ULF) wave activity has also been processed from the GOES satellites.

Chapter 5 describes the probabilistic forecasting technique in space weather prediction and the results based on the studies about LALD southward IMF events. The potential improvement of predicting the occurrence and intensity of IMF Bs-events using in situ and remote observations has also been discussed.

Chapter 6 summarized the key results of this thesis and includes some discussion of the future work.

CHAPTER II

Identification and properties of southward IMF intervals

2.1 Introduction: The deviation from Parker-spiral structure of IMF

Based on the classic Parker theory (*Parker*, 1958), the interplanetary magnetic field (IMF) lines form a spiral pattern, which does not produce a polar magnetic field component. However in observations, it became clear that there is component perpendicular to the equatorial plane - IMF z-component (Bz) under unperturbed conditions. A non-zero Bz is observed for transients propagating outward from the Sun observed in the interplanetary medium as interplanetary coronal mass ejections (ICMEs) (*Lindsay et al.*, 1995), interplanetary small-scale magnetic flux ropes (ISMFRs) (*Moldwin et al.*, 2000; *Zhang et al.*, 2012), stream interaction regions (SIRs) (*Rosenberg and Coleman*, 1980, e.g.), Alfvénic solar wind (*Zhang et al.*, 2014).

Solar activity characterized by sunspot number (SSN) shows an 11-year or 22-year cycle, which is modulated by the large-scale polarity change of the magnetic field in polar coronal holes. The statistical features of some solar wind/IMF parameters and geomagnetic activity level have also been analyzed and also found to have an 11-year cycle. The correlation between the SSN, solar wind/IMF parameter, and

geomagnetic disturbance cycles has also been demonstrated (*Richardson and Cane*, 2010). However, the distribution of the IMF Bz and southward component (Bs) have rarely been studied, nor their correlation with the SSN.

This chapter provides the first systematic analysis of the southward IMF intervals identified by the occurrence constrained by preset amplitude and duration thresholds. Based on multiple in situ satellite measurements, such as WIND, ACE, STEREO, Ulysses, and Helios, as well as solar activity indices (sunspot number), the statistical properties of large-amplitude, long-duration (LALD) southward IMF events are investigated, including the correlation with sunspot number, in situ plasma and magnetic field characteristics.

Following in this chapter, we will discuss about the distribution of IMF Bz and Bs over time and space, and its relationship with the solar activity over solar cycles.

2.2 The characteristics of IMF Bz intervals over time and space

In order to study the statistical characteristics of the non-Parker-spiral polar component of IMF, we examine the 1 min WIND/OMNI magnetic field data at 1 AU from 1995 to 2010 (data source: $http://cdaweb.gsfc.nasa.gov/istp_public/$). The OMNI data are 1-min-averaged, field/plasma data sets shifted to the Earth's bow shock nose (BSN), involving an interspersal of BSN-shifted ACE, WIND, IMP 8 and Geotail data. Figure 2.1 illustrates the distribution of IMF Bz amplitude in Geocentric Solar Ecliptic (GSE) coordinates from 1 min WIND magnetometer data (except (a) using OMNI 1 min magnetic field data) (solid line in each panel) and the first-order Gaussian fit (dashed line). WIND is a spin stabilized spacecraft launched in November 1, 1994 and placed in a halo orbit around the L1 Lagrange point, more than 200 Re upstream of Earth to observe the unperturbed solar wind that is about

to impact the magnetosphere of Earth. Figures 2.1a includes all the data points from 1995 to 2010, 2.1b interplanetary magnetic flux rope (interplanetary magnetic flux rope (IMFR), including MC and interplanetary small-scale magnetic flux rope (ISMFR)) intervals from 1995 to 2005, 2.1c ejecta intervals from 1995 to 2004, and 2.1d stream interaction region (SIR) intervals from 1995 to 2004. The data processing approach and categorization method will be described in the following section. The results for years in Figures 2.1a, 2.1c, and 2.1d all show one peak at 0 nT with a symmetric distribution of positive and negative values, which fit the Gaussian function well within about ± 10 nT. Then we examined the data points that have IMF Bz less than -10 nT and found that nearly 90% of them occurred in continuous southward IMF intervals with durations longer than 1 h. The distribution of IMFRs in Figure 2.1(b) has other significant peaks besides 0 nT at more positive and negative Bz values than the other categories. However, the distribution of IMF Bz related with IMFR in Figure 2.1b shows the highest fit to Gaussian function, with good fit up to about [-30, 30] nT. The half width of the Gaussian fit function is 20 nT for IMFR, 8 nT for ejecta, 10 nT for SIR, and 6 nT for the whole duration 1995-2010. This indicates that MCs are the dominant source of extreme IMF Bz values, and also that the underlying mechanisms for the generation of the z- component of IMF embedded in these solar wind transients are different.

To study the spatial distribution of IMF Bz, we also analyzed the magnetometer data from other satellites when they were located at the near-ecliptic plane (Figure 2.2). Figure 2.2(top) presents the trajectory of Ulysses satellite from Oct 1997 to Nov 1998 when it was located within 10 degrees from the ecliptic plane and 5.3 AU - 5.4 AU from the Sun. Ulysses is the first spacecraft to study our Sun's poles, launched on Oct 6 1990. The figure on the bottom shows the distribution of Bn amplitude in the radial-tangential-normal (RNT) coordinate based on the 1-min data from Vector Helium Magnetometer (VHM) onboard Ulysses during the periods shown on the left

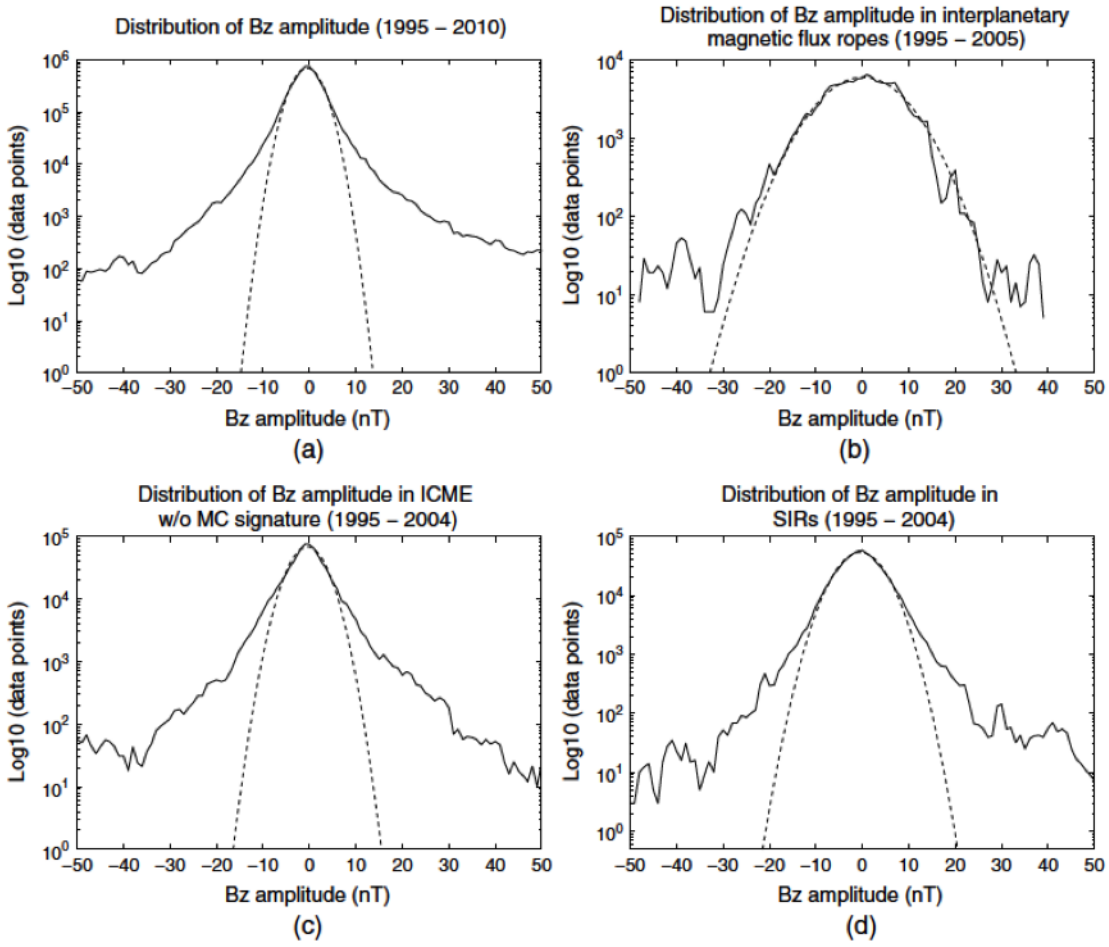

Figure 2.1: (a) All the data points from 1995 to 2010 (OMNI magnetic field data), (b) interplanetary magnetic flux rope (IMFR, including MC and ISMFR) intervals from 1995 to 2005, (c) ejecta intervals from 1995 to 2004, (d) SIR intervals from 1995 to 2004. The distribution of IMF Bz amplitude in GSE coordinates from 1 min WIND magnetometer data (except (a)) is shown as the solid line in each panel, and the dashed lines are the one-peak Gaussian fit.

and Dec 26, 2003 - Jan 30, 2005 when it has similar trajectory in the same format as in Figure 2.1. The result shows one peak at 0 nT with a symmetric distribution of positive and negative values, which fit the Gaussian function well within about ± 1 nT. According to Parker's theory, $B_{non-radial} \propto r^{-1}$, where r is the radial distance from the Sun, the normal-component of Ulysses magnetometer data could be scaled to r = 1 AU as follows $B_{n-scaled} = B_{n-measured} * r$,where r is in AU. It is noted that the occurrence count of IMF Bz drops from 10^6 to 10^3 when Bz amplitude increases from 0 to 20 nT based on the OMNI data measured at 1 AU (Fig. 2.1a); however, if we scale the Bn measured by Ulysses at 5.3-5.4 AU to 1 AU by multiplying 5.35, the occurrence rate has dropped from 10^6 to 10^2. When the Bz value is below -5 nT at 1 AU, which corresponds to ∼-1 nT at 5.3 AU according to the r proportional rule, there is no such difference in the occurrence rate. It will be shown in the next chapter that the main contribution to the large-amplitude, long-duration IMF Bs is from ICMEs, which expands at a rate faster than $B_{non-radial} \propto r^{-1}$, thus the large-amplitude Bz will be decreased more quickly than the small-amplitude Bz when it propagates outward from the Sun.

Besides the distribution of IMF Bz in terms of the radial distance from the Sun, we have also performed the analysis for the distribution with varying latitude (Figure 2.3). We analyzed the 10-sec resolution magnetic field data from instrument IMPACT (In-situ Measurements of Particles and CME Transients) onboard Solar TErrestrial RElations Observatory (STEREO) Ahead (STA) and Behind (STB). STEREO is the third mission in NASA's Solar Terrestrial Probes program (STP), launched in Oct 2006. The two nearly identical observatories - one ahead of Earth in its orbit, the other trailing behind - have traced the flow of energy and matter from the Sun to Earth. Figure 2.3 (top) presents the orbit of the two STEREO spacecraft (A in blue, B in green) in Heliocentric Inertial (HCI) coordinate. It is shown in the trajectory that the radial distance is around 1 AU (0.96 - 0.97 AU for STA and 1.0 -

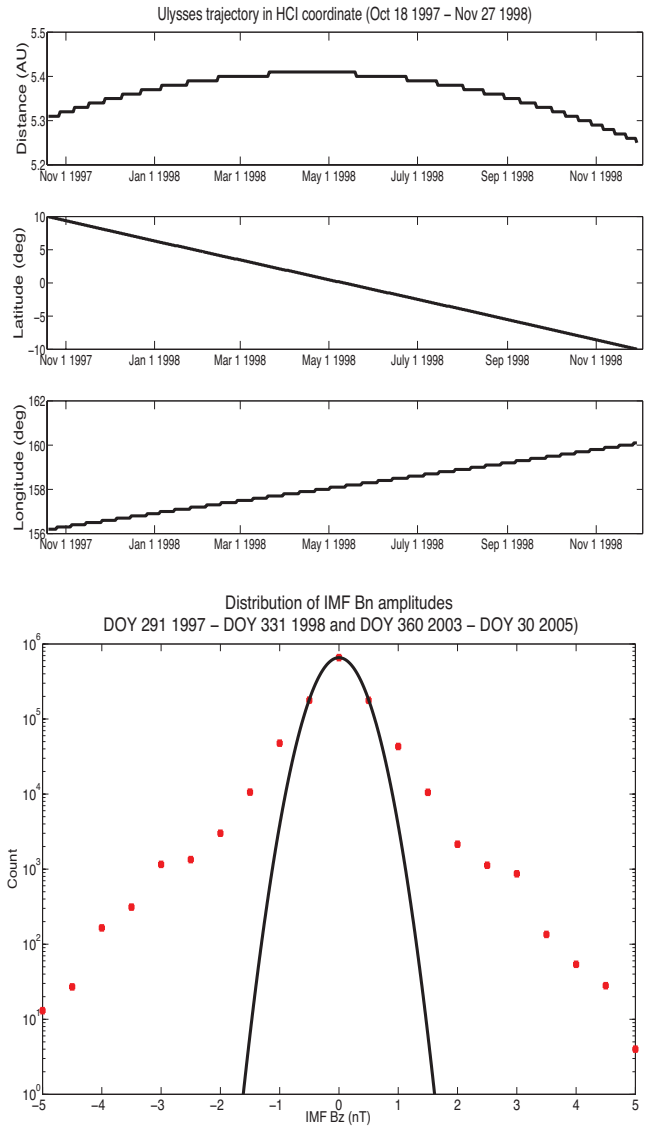

Figure 2.2: top: The orbit of Ulysses satellite in Heliocentric Inertial (HCI) coordinate for the period Oct 18, 1997 - Nov 27, 1998 (the trajectory for Dec 26, 2003 - Jan 30, 2005 is similar); bottom: The distribution of IMF Bz amplitude in HCI coordinates from 6-sec Ulysses magnetometer data in the same format as in Fig 2.1.

1.1 AU for STB), and latitude spanning within 10 degrees, but the longitudinal separation of the STA and STB spacecraft from the Earth changes from almost zero to 90 degrees. Figure 2.3 (bottom) shows the distribution of IMF Bz measured by STB (left) and STA (right), which are similar to that observed at the near-Earth satellites. However, the tail part ($|Bz| > 20$ nT) of the distributions obtained from STEREO observations is more disturbed and more similar to the distribution of IMF Bz related with SIRs shown in Fig. 2.1d. These results suggest that the non-Parker-spiral component of IMF does not depend on the longitudinal location in the near-ecliptic-plane region at least for the first-order approximation.

2.3 The characteristics of large-amplitude, long-duration (LALD) IMF Bs intervals over time and space

2.3.1 Identification of large-amplitude, long-duration southward IMF (IMF Bs) intervals

To further investigate the properties of southward IMF intervals, we define and select IMF Bs-events as follows:

1. Setting the maximum values of IMF Bz in GSE coordinates from 0 nT to -10 nT decreasing by 1 nT each step and automatically identifying the intervals with at least three satisfactory points (3 min duration), ignoring single points between two intervals that meet the requirement;

2. Setting the minimum values of the duration from 3 min to 6 h increasing by 10 min each step and selecting the Bs events from step (1). Figure 2.4 shows a schematic example about how we accept and reject an interval as a Bs event. The intervals from time point 5 to point 12 and from time point 15 to time point 18 are considered as Bs events with thresholds as -5 nT and 3 mins.

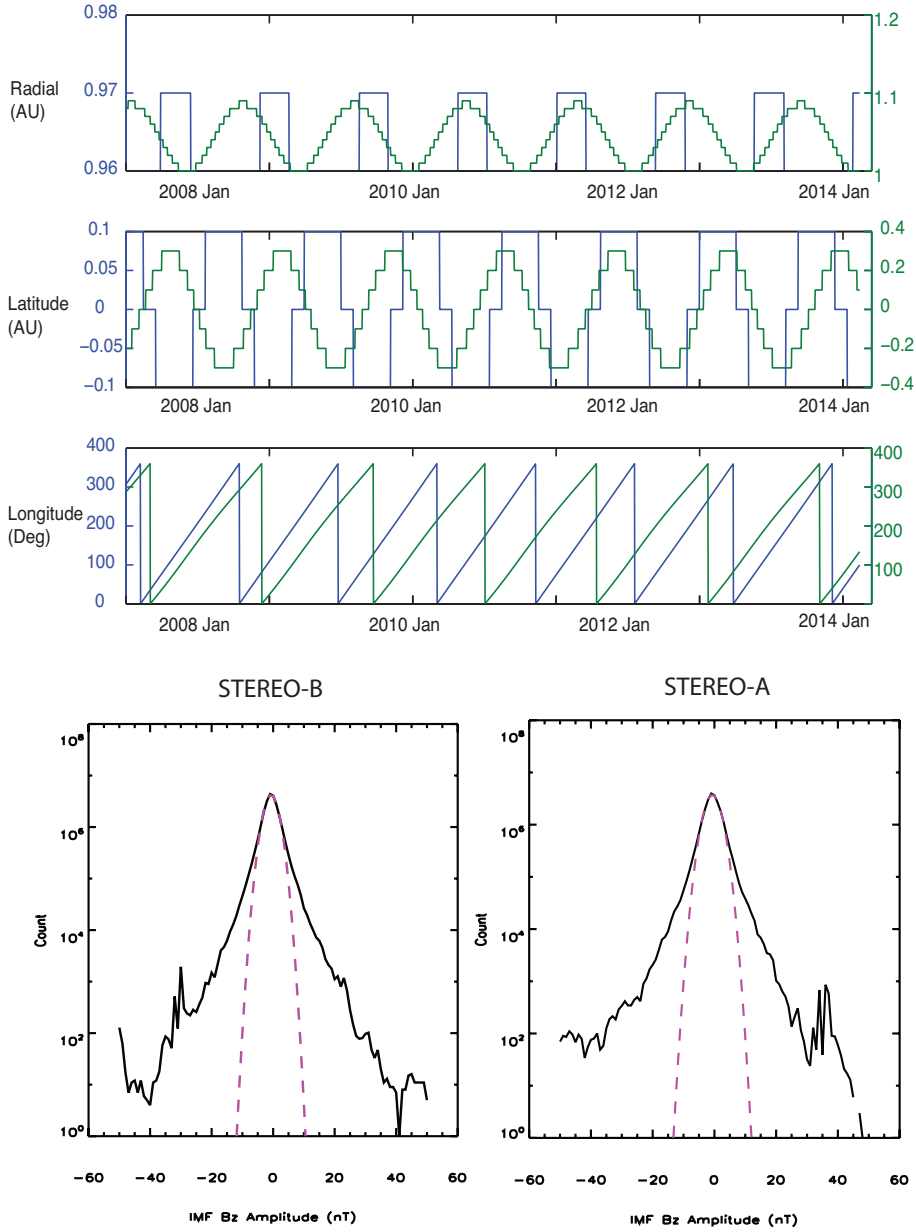

Figure 2.3: Top: The orbit of STEREO A(blue) and STEREO B(green) satellite in Heliocentric Inertial (HCI) coordinate for the period DOY 200 2007 - DOY 200 2014; bottom: The distribution of 1-min averaged IMF Bz amplitude in HCI coordinates from 10-sec magnetometer data from IMPACT instrument onboard STEREO B(left)/A(right) in the same format as in Fig 2.1.

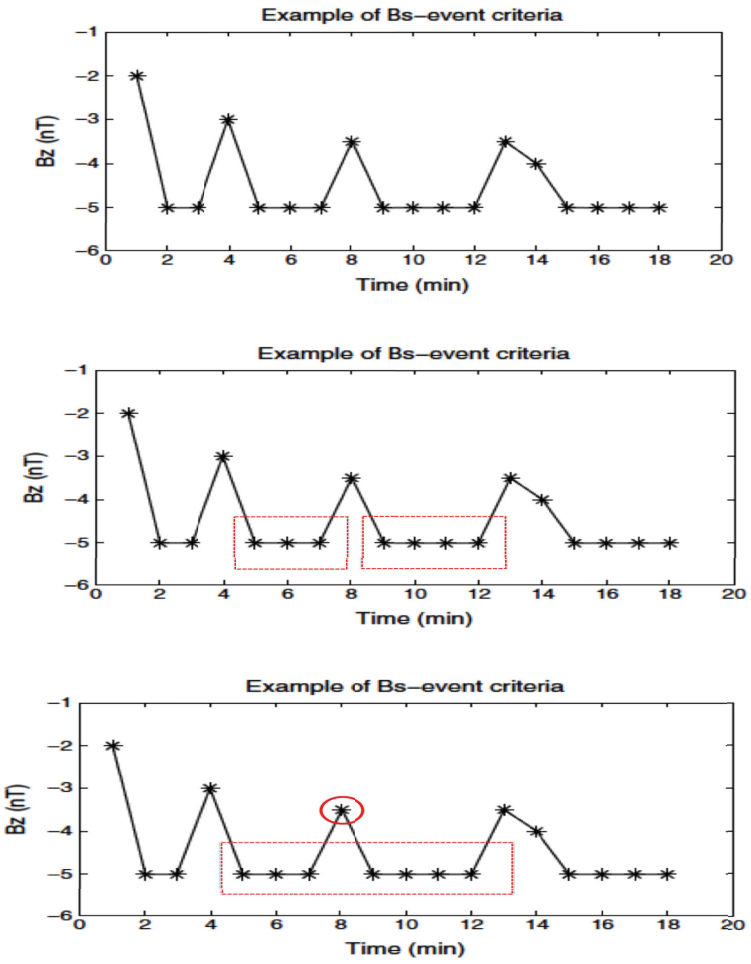

Figure 2.4: A schematic example about how we accept and reject an interval as a Bs event. The intervals from time point 5 to points 12 and from time point 15 to time point 18 are considered as Bs events with thresholds as -5 nT and 3 mins.

2.3.2 Statistical properties of IMF Bs compared to sunspot number

Figure 2.5 presents the normalized yearly distribution (divided by the range of each parameter) of the number and total duration of Bs events from 1995 to 2010 (1 min averaged definitive multispacecraft interplanetary magnetic field data from OMNI), compared with the sunspot number. Table 1 shows the minimum and maximum values for variables illustrated in Figure 2.5. The period of the events lasts at least 3 mins, 1 h, and 6 h in Figures 2.5a, 2.5b, and 2.5c, respectively. The upper threshold of the Bz value is -10 nT, -5 nT, and 0 from the top to the bottom panels in each plot. There is a positive correlation shown between the variation of sunspot number and the distribution of IMF Bs properties for the -5 nT and -10 nT cases but no clear correlation for 0 nT. However, the correlation is good for all the events longer than 6 h regardless of the magnitude (shown in Figure 2.5c). It is also interesting that the maximum of sunspot number does not always match the Bs event maximum from Figure 2.5. For the Bs events with Bs thresholds less than -10 nT, shown in the first column in Figure 2.5, the peak of total duration is 1 year ahead of the sunspot number peak. There is a dual-/triple-peak signature in the yearly variation of IMF Bs event number and duration of Bs events. The low occurrence of IMF Bs events from 2007 to 2009 indicates that the most recent solar minimum was prolonged, consistent with sunspot number, which has been shown in previous work (*Russell et al.*, 2010).

Besides the yearly trend of IMF Bs-events at 1 AU, we also analyzed the magnetic field data from Helios spacecraft. Helios-A and Helios-B (also known as Helios 1 and Helios 2), are a pair of probes launched into heliocentric orbit for the purpose of studying solar processes on December 10, 1974 and Jan 15, 1976. Figure 2.6 illustrates the trajectory of Helios 1 and 2 around the Sun in the ecliptic plane (the orbit is on the ecliptic plane). In order to investigate the temporal variance of IMF Bs-events in terms of different solar cycles, we compared the distribution of IMF Bs-event duration based on the magnetic field data from Helios (1975 - 1981) and OMNI (1995 - 2001,

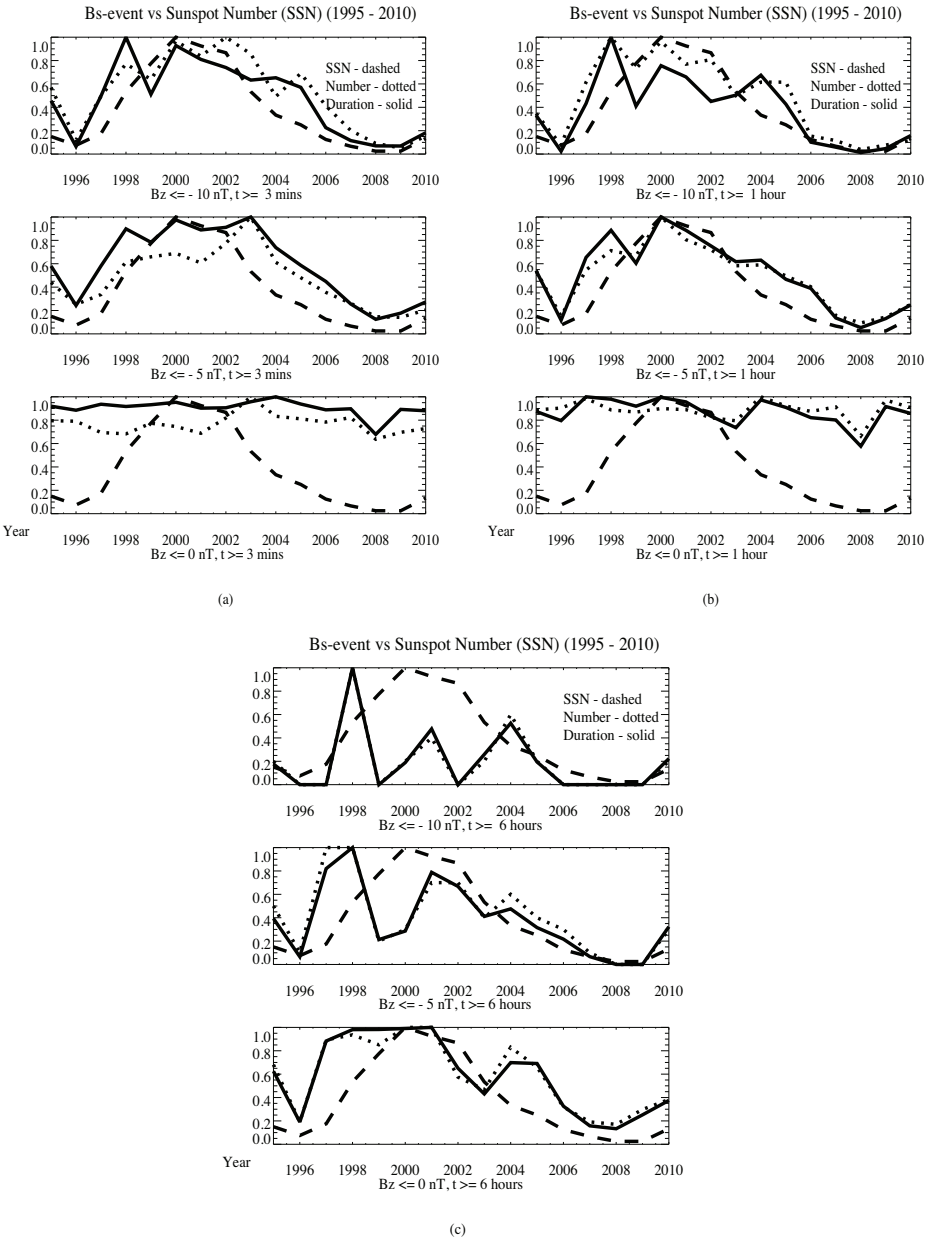

Figure 2.5: The yearly distribution (divided by the maximum of each parameter) of the number and total duration of Bs events from 1995 to 2010, compared with the sunspot number. The period of the events lasts at least (a) 3 min, (b) 1 h, and (c) 6 h. The upper threshold of the Bz value is -10 nT, -5 nT, and 0 nT from the top to the bottom panels in each plot.

Variables	Min Count	Max Count	Min Time (hr)	Max Time (hr)
Sunspot number	3	120		
(-10 nT, 3 min)	16	307	9	132
(-5 nT, 3 min)	409	2893	87	698
(0 nT, 3 min)	7401	10839	2919	4304
(-10 nT, 1 hr)	2	36	1	87
(-5 nT, 1 hr)	12	147	17	327
(0 nT, 1 hr)	859	1160	1362	2359
(-10 nT, 6 hr)	0	5	0	47
(-5 nT, 6 hr)	0	10	0	101
(0 nT, 6 hr)	8	47	59	441

Table 2.1: Minimum and Maximum values of variables illustrated in Fig. 2.5

2007 - 2013) for time periods corresponding to rising phase of three solar cycles, shown in Figure 2.7 (top). Figure 2.7(bottom) presents the distribution of occurrence rate over data points of IMF Bs-event (Bz <= -10 nT) duration based on data from Helios (red) and OMNI (1995 - 2001 green, 2007 - 2013 blue). It is shown that the occurrence frequency of LALD IMF Bs-event during the rising phase of Solar Cycle 21 (1975 -1981) and 23 (1995 - 2001) is similar, while the result for solar cycle 24 (2007 - 2013) shows almost half of the frequency compared to 21 and 23. Extensive studies have demonstrated that the solar activity during the most recent solar cycle was unprecedentedly weak based on observations of sunspot number, F10.7 index and solar wind/IMF parameters, such as bulk speed, IMF magnitude, heavy ion density, ion charge status (*Heelis et al.*, 2009; *Russell et al.*, 2010). It is shown from our study that the occurrence rate of LALD IMF Bs-events is also an indicator of the solar activity if the data is scaled by the radial distance from the Sun.

Figure 2.8 shows the normalized distribution of IMF Bs-events duration, occurrence rate, and average duration compared with sunspot number based on the observations from STB (left) and STA (right) in the same format as Figure 2.5. The total duration and number of IMF Bs-events change in the similar way as the SSN, except the local minima measured by STB during 2013 and the decrease from 2013 to 2014 observed by STA. However, the averaged duration (total duration over total

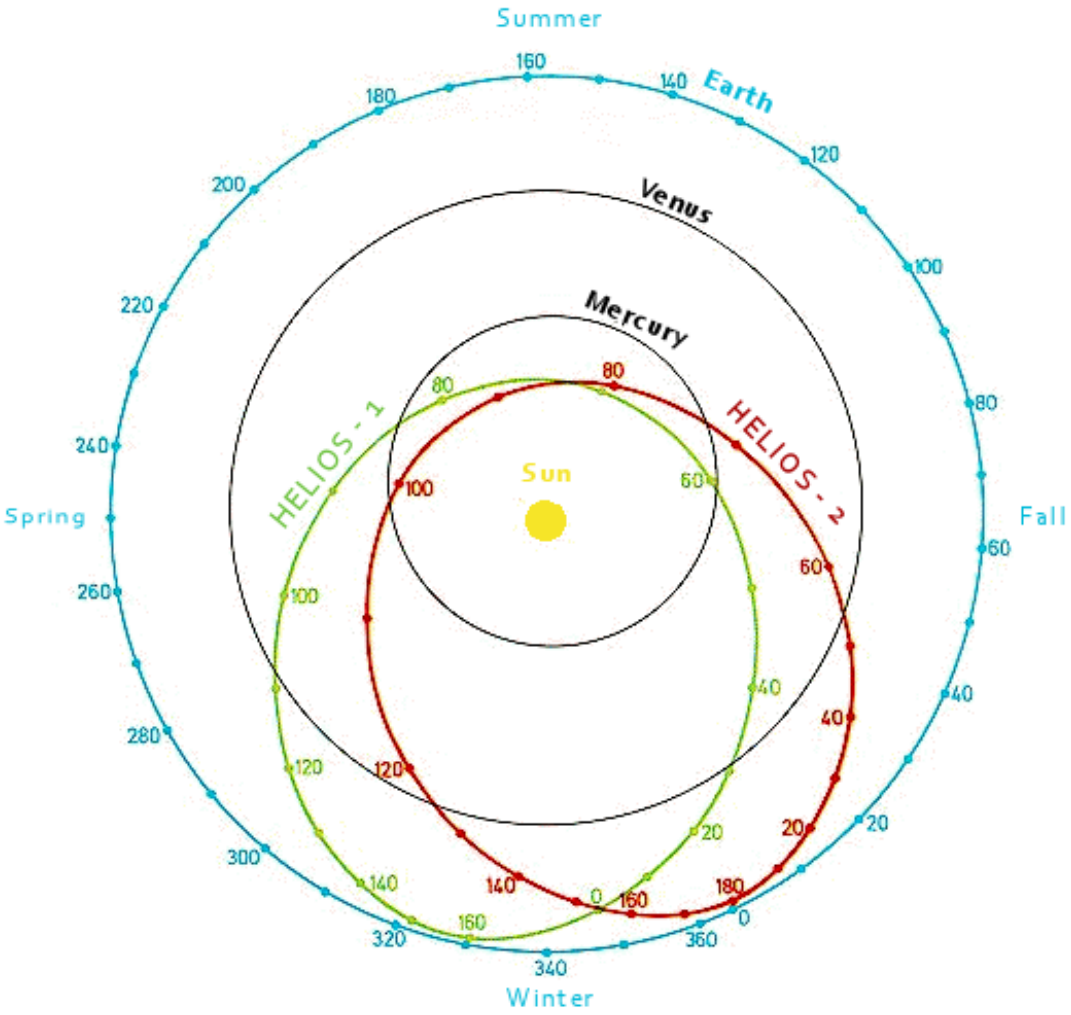

Figure 2.6: Helios 1 and Helios 2 trajectory around the Sun. [Credit: NASA]

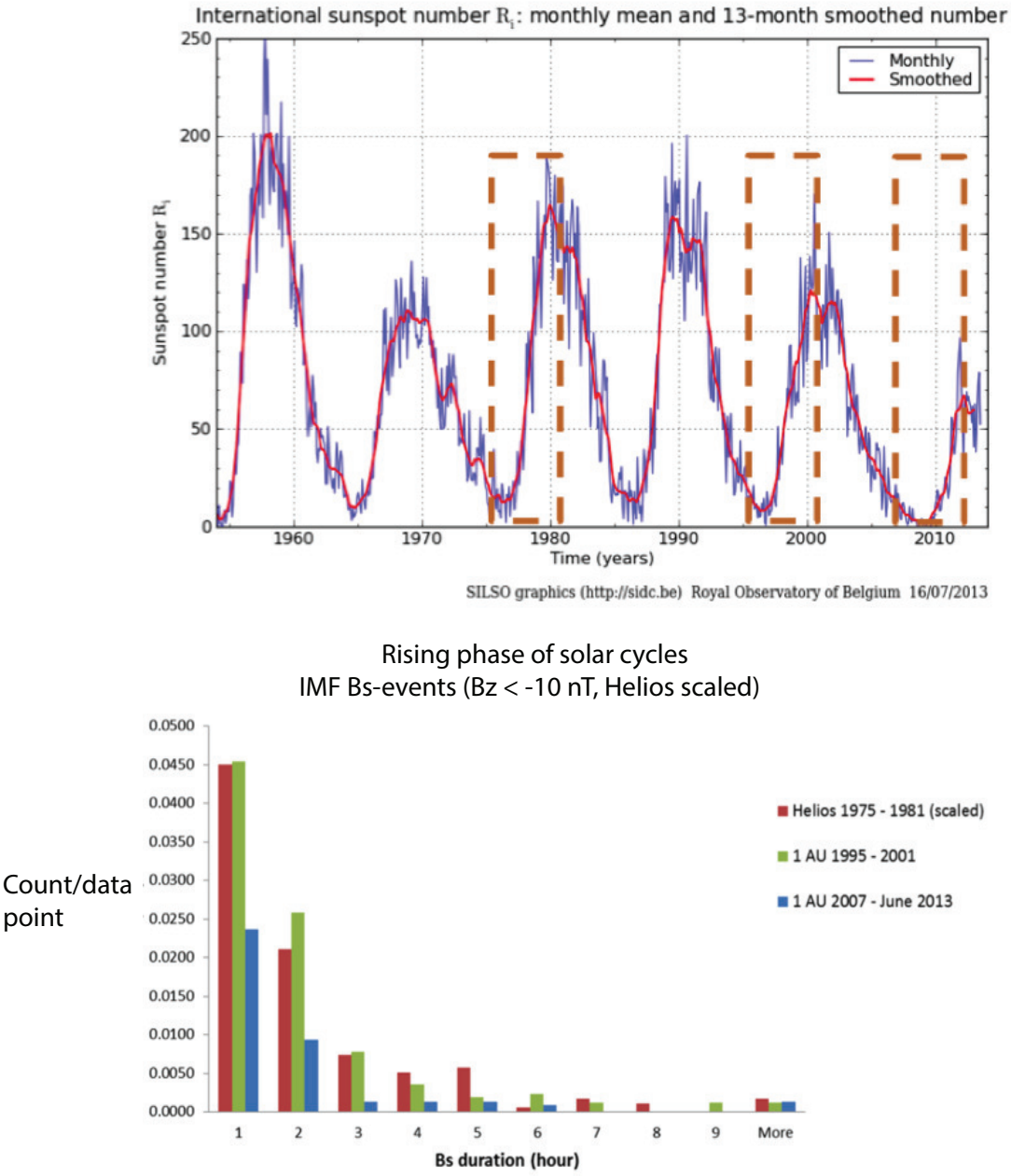

Figure 2.7: Top: Monthly (blue) and smoothed (red) sunspot number from 1953 to 2013. The orange boxes denote the time periods we analyzed the magnetic field data from Helios (1975 - 1981) and OMNI (1995 - 2001, 2007 - 2013), corresponding to the rising phase of three solar cycles; bottom: the occurrence rate over available data points of IMF Bs-events in terms of duration (1 - 9+ hours) based on Helios (red), OMNI (green and blue) data for the three periods marked in the top figure. The magnetic field component has been scaled according to r^{-1} rule.

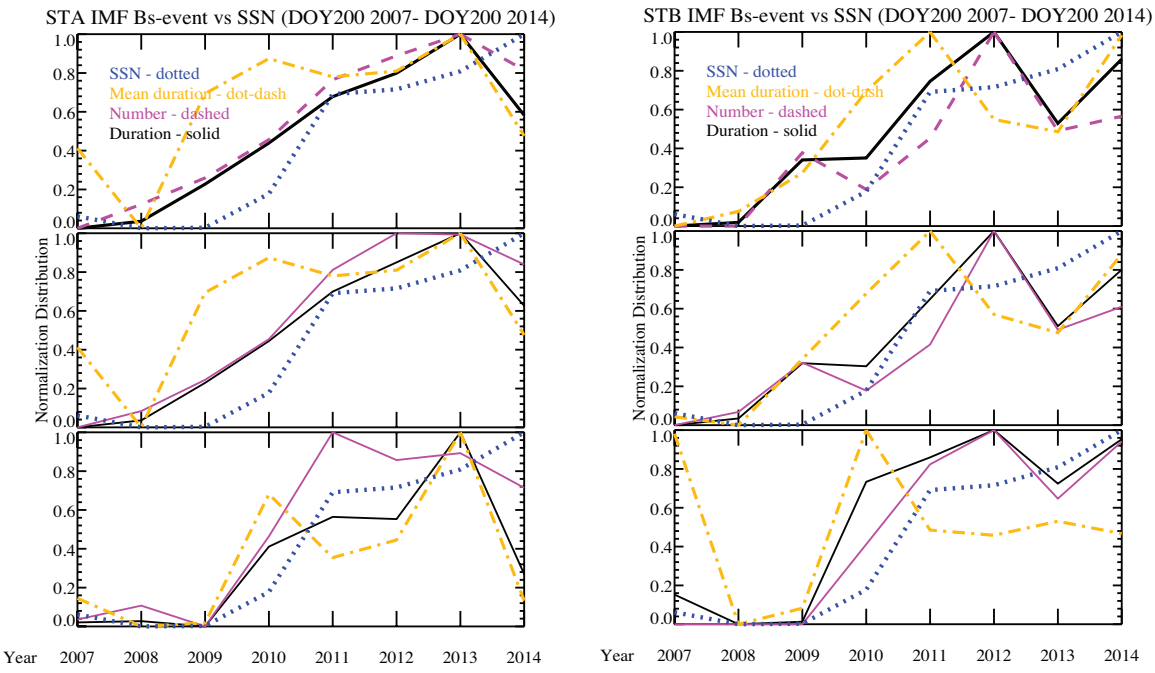

Figure 2.8: The yearly distribution (divided by the max-min of each parameter) of the number, total duration, and average duration of IMF Bs events from 2007 to 2014 observed by STB (left) and STA (right), compared with the sunspot number. The thresholds of for the IMF Bs-events are Bz $<$ -5 nT, t $>$ 1 hour (top), Bz $<$ -5 nT, t $>$ 30 min (middle), Bz $<$ -10 nT, t $>$ 30 min (bottom).

number, shown as the yellow lines) does not show better consistence with SSN for any case. It is similar as the results from OMNI data that when the thresholds of IMF Bs-events are set as Bz $<$ -5 nT and t $>$ 1 hour, the statistics of the events is more synchronized with the yearly SSN. Comparing between the results based on STB and STA observations, the latter is more similar with the profile of SSN.

2.4 The properties of plasma, ion composition and magnetic field of LALD IMF Bs intervals

To further investigate the changing properties of solar wind parcels embedded with IMF Bs intervals as they propagate along the Parker spiral, we analyzed the plasma

Variables	Min Count	Max Count	Min Time (hr)	Max Time (hr)
Sunspot number	3	120		
STB (-10 nT, 30 min)	3	20	3	36
STB (-5 nT, 30 min)	62	180	69	267
STB (-5 nT, 60 min)	26	79	43	195
STA (-10 nT, 30 min)	2	30	2	78
STA (-5 nT, 30 min)	45	188	43	330
STA (-5 nT, 60 min)	9	90	19	264

Table 2.2: Minimum and Maximum values of variables illustrated in Fig. 2.8

measurements from STEREO spacecraft and Advanced Composition Explorer (ACE). ACE launched on a McDonnell-Douglas Delta II 7920 launch vehicle on August 25, 1997 is orbiting the L1 point. From its location at L1 ACE has a prime view of the solar wind, interplanetary magnetic field and higher energy particles accelerated by the Sun, as well as particles accelerated in the heliosphere and the galactic regions beyond. Figure 2.9 shows the IMF and solar wind velocity, density measurements of a LALD IMF Bs-event related with the same corotating interaction region (CIR) from STB, ACE and STA. The IMF Bs-events are marked by the dashed vertical lines. It is shown from Figure 2.9 that STB observed the CIR and the IMF Bs-event first, then ACE, and finally STA. The duration between the dashed lines is 10 hours, 4.5 hours, and 10.5 hours for STB, ACE and STA respectively, while the amplitude of the IMF southward component shown as the blue line in the fourth panel is weaker at STA than STB and ACE. The magnetic field magnitude plotted in blue lines in the first panel shows an increase followed by a decrease during the IMF Bs intervals for STB and ACE, but not such a clear trend at STA. It is shown from the second-fourth panels that all the three components are constant polarity between the dashed lines measured at ACE and STA, while STB observed a polarity change of the IMF tangential component. It is indicated that the satellite crossing of heliospheric current sheet does not account for the emergence of non-Parker-spiral component of IMF. The solar wind bulk speed illustrated in red lines in the first panel shows

a smooth increase during the IMF Bs-event at STB, while the other two satellites observed an almost unchanged profile of solar wind speed. The solar wind density observed by STB shown as green line in the last panel presents complex variance, while smooth monotone decrease from the measurements of ACE and STA. The solar wind velocity and IMF components shown in the second-fourth panel show good correlation in STB observations, but not for ACE or STA, which will be discussed in detail in the discussion section.

Besides the case study, we performed a superposed epoch analysis (SEA) of solar wind/IMF parameters for the IMF Bs-events observed by different satellites in order to investigate their statistical characteristics. The Superposed Epoch Analysis (SEA) technique is a statistical method used to resolve significant signal to noise problems. Through simple compositing, the SEA method involves sorting data into categories dependent on a "key- time" for synchronization and then comparing the means or medians of those categories. The method allows the analysis of systematic behavior of a parameter with respect to an event. In our study, SEA allows the identification of any systematic behavior prior to the start of the IMF Bz event. Examples of applications of the SEA method are widespread in various scientific fields of study and are extensively used in space physics (*Forbush et al.*, 1982; *O'Brien et al.*, 2001; *Green et al.*, 2004, e.g.). Setting the start time of the southward IMF-events (t $>$ 1 hour, Bz $<$ -5 nT for OMNI and STEREO and Bz $<$ -1 nT for Ulysses) identified by (*Zhang and Moldwin*, 2014) as the zero epoch time. We then performed a SEA of IMF Bz, IMF magnitude (Bt), solar wind speed (Vsw), proton density (Np), for 24 hours before and 24 hours after the zero epoch time using the 1-minute averaged data. It is worth noting that the zero epoch time is not when the IMF becomes negative, but when it falls below -5/-1 nT . We accept the potential overlaps in intervals in epoch selection process and do not remove other events that could occur within 24 hours. The results for data from OMNI, STB, STA, and Ulysses are shown in (a), (b), (c),

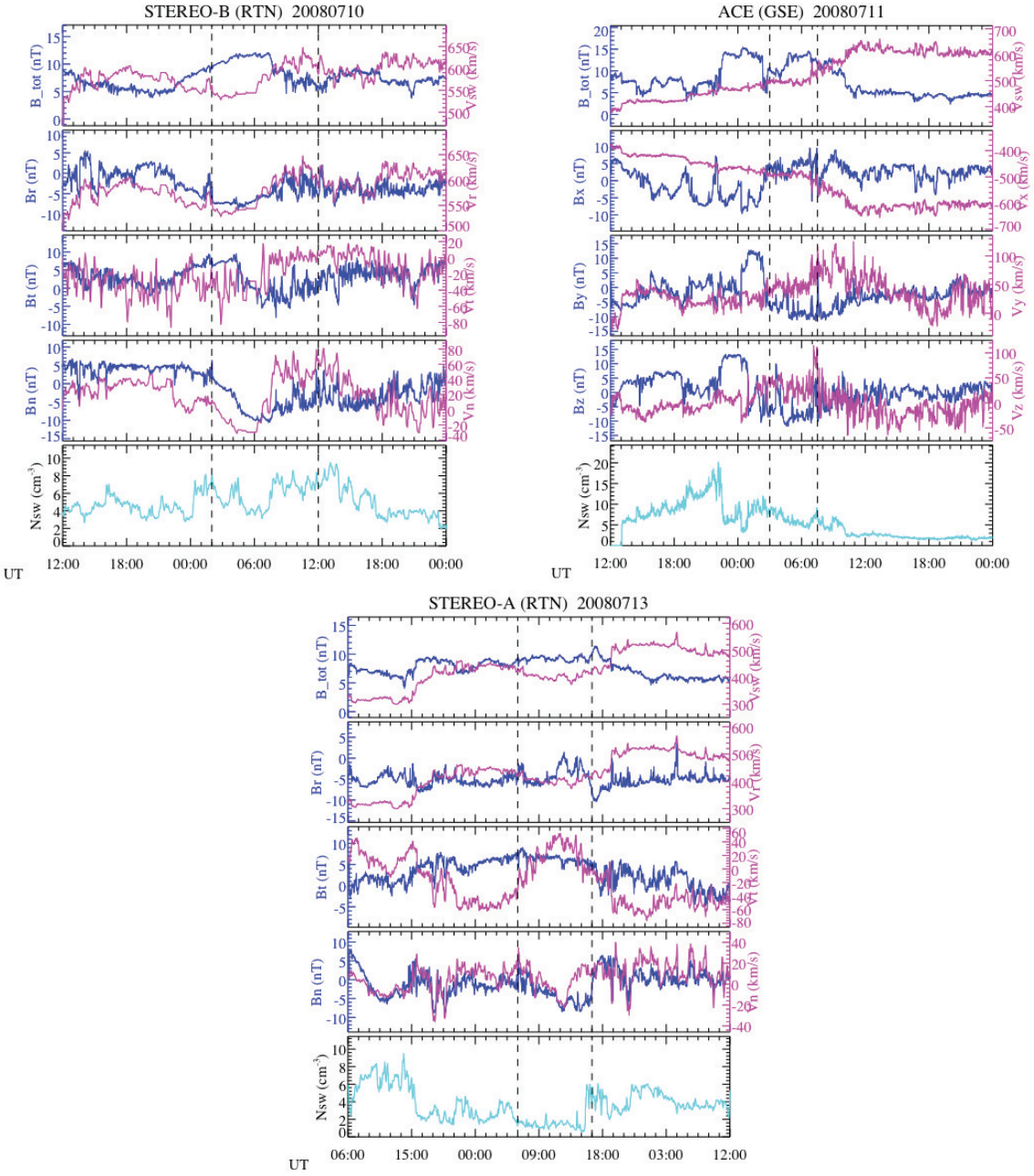

Figure 2.9: Measurements of IMF/solar wind velocity magnitude and components (top four panels) and proton density from STB, ACE and STA for the LALD IMF Bs-events related with the same CIR. The dashed lines denote the period of the IMF Bs-events.

and (d) respectively 2.10. Fig. 2.10 (a)-(c) show similar profile of the magnetic field magnitude, solar wind speed, and density during the IMF Bs-events. While the IMF z-component decreases to -5 nT and keeps strongly southward, the total magnetic field and solar wind density show an increase followed by a decrease, and the bulk speed smoothly monotone increases. Illustrated in Fig. 2.10(d), the magnetic field strength observed by Ulysses shows the similar trend as (a)-(c), however the solar wind speed and density are almost unchanged.

2.5 Discussion and Conclusion

As shown in Fig. 2.1, 2.2, and 2.3, the occurrence rate distribution of IMF Bz value fits well to Gaussian function with zero mean in the region of [-10, 10] nT, with much higher occurrence frequency beyond this range. It is indicated that the emergence of large-amplitude non-Parker-spiral is not random fluctuations of the solar wind or IMF, but some physical mechanisms in the solar atmosphere or interaction in the interplanetary medium.

We also performed the analysis of yearly distribution of IMF Bs-events based on data from different satellites over different solar cycles. We found that the moderate and strong IMF Bs-events are well correlated with the yearly profile of SSN, but not for the weak IMF Bs intervals, which suggests, as the Gaussian function analysis indicates, that the small-value IMF Bs are generated by random fluctuations in the interplanetary medium or waves in the solar wind propagating outward from the Sun while the LALD IMF Bs are related with solar activity and solar transients. *Prestes et al.* (2006) performed spectral analysis of SSN and geomagnetic indices and found that the annual average of antipodal activity (aa) shows a dual-peak structure, one near sunspot cycle maximum and the other in the descending phase. They proposed that the first peak is caused by CMEs while the second one resulted from coronal hole fast streams. The dual-peak phenomenon is also present in our study for IMF

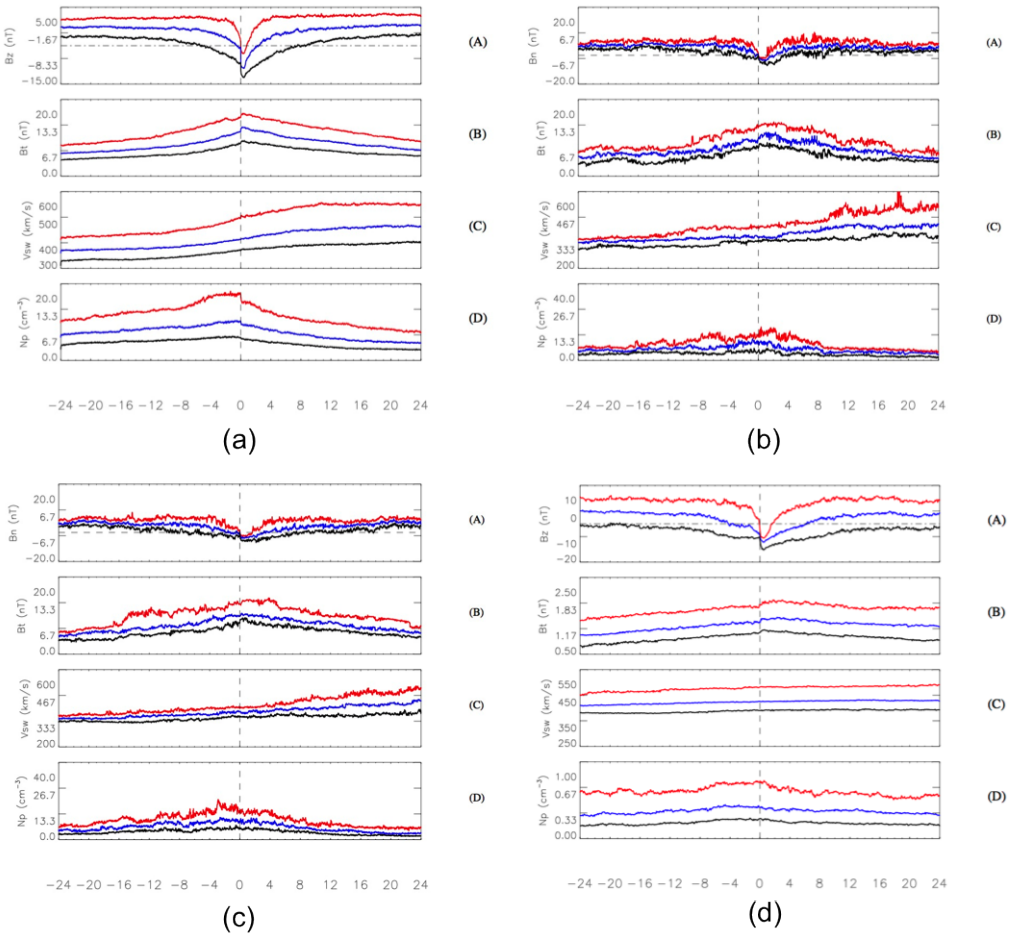

Figure 2.10: Superposed epoch analysis for all the IMF Bs-events (Bz < -5 nT, t > 60 min) based on OMNI data during 1995 - 2013 (a), STB (b) and STA (c) during 2007 - 2014, and IMF Bs-events (Bz < -1 nT, t > 60 mins) observed by Ulysses (d) in the two periods shown in Fig. 2.2. The epoch zero is set at the change of IMF Bz drops under -5 nT/-1 nT denoted by the dashed vertical line, and the duration is 48 hours. The red/blue/black are the temporal files of upper/middle/lower quartile of IMF Bz, IMF amplitude, solar wind speed, proton density from top to bottom panels. The horizontal dashed line marks the threshold as Bz = -5 nT (a-c). All the data is downloaded from Coordinated Data Analysis Web (CDAWeb, $http://cdaweb.gsfc.nasa.gov/cgi-bin/eval1.cgi$)

Bs and is more significant if the duration of Bs event is longer. Analyzing the yearly distribution of IMF Bs intervals for different categories (the detailed methodology will be discussed in the next chapter), we find that the contribution to the second peak is mainly from the SIR and Bs event unrelated with well-defined solar wind structures. The cross-correlation analysis of sunspot number (Rz) and aa in (*Prestes et al.*, 2006) implies that the maximum value of aa lags that of Rz by a year; however, IMF Bs event occurrence is peaked 1 year ahead of Rz in our results for the main peak. It is also shown from our study that the occurrence rate of LALD IMF Bs-events is another indicator of the unprecedented weak solar cycle (SC24), besides parameters like F10.7 index, solar wind speed, and magnetic field strength.

We also investigated the spatial distribution of IMF Bs-events occurrence by comparing the statistical analysis results based on data from OMNI, STEREO, Helios, and Ulysses. It was shown that the non-Parker-spiral component of IMF is decreasing faster than the way inversely proportional to the radial distance from the Sun, which implies the sources of some large-scale IMF Bs-events could be processes like reconnection in the local interplanetary medium or solar wind transients expanding in a similar way as CMEs in the interplanetary region. Although the distribution function in terms of longitudinal locations does not show much difference from a statistical perspective, the case study shown in Fig. 2.10 suggests that the configuration of the magnetic field, or the properties of the IMF Bs changes significantly when it propagates around solar longitude. Meanwhile, the local plasma conditions during the IMF Bs-events do not vary in a similar way at different locations. It is interesting to note that not all of them occur in the increasing period of solar wind speed, which implies that the stream interface (SI) of the CIR is not always the source region of the large-scale IMF Bs, but other mechanisms, such as [Rouillard et al., 2009] suggesting that the small-scale magnetic cloud with a flux rope topology embedded prior to the SI contributes to the Bs interval.

It is found that the statistical profile of solar wind speed, density and magnetic field magnitude change in similar ways during IMF Bs-events observed by STEREO and near-Earth satellites - different longitudes on the ecliptic plane at 1 AU, but the 1 AU observation are significantly different from the measurements at 5.3 AU by Ulysses. It implies that the major sources of LALD IMF Bs-events are long-lasting and/or large-spatial-scale activities in the solar atmosphere propagating outward to the interplanetary medium. Thus it is possible to predict the occurrence of LALD IMF Bs-events at the near-Earth region based on the observations from STEREO A or B depending on their relative locations to the Earth. It also suggests that instead of the bulk speed and plasma density, the heavy ion charge state or heavy ion density could be much better indicators of the source region of IMF Bs-event and in situ plasma conditions for forecasting its occurrence, as such parameters change little while propagating in the interplanetary medium after ejected from the Sun.

In conclusion, the non-Parker-spiral component of the interplanetary magnetic field is not always due to random fluctuations of the local plasma environment, but are indicators of large-scale solar activity, physics processes in the solar atmosphere, and drive geomagnetic activity. The spatial distribution of IMF z-component on the ecliptic plane is mainly dependent on radial distance from the Sun, weakly on longitude. Also, the variance of in situ plasma conditions show a pattern prior to and during the large-amplitude, long-duration IMF Bs-events, which could be used to improve the space weather forecasting system.

CHAPTER III

The source of large-amplitude, long-duration southward IMF

3.1 Introduction: Theories of the source for southward IMF and observations of solar transients

Observationally, the large-amplitude, long-duration (LALD) southward IMF intervals are often embedded in solar wind transients, such as high-speed streams (HSS) from coronal holes (CHs) (*Sheeley et al.*, 1976), coronal mass ejections (CMEs) (*Klecker et al.*, 2006b; *Lindsay et al.*, 1995), and corotating interaction regions (CIRs) (*Rosenberg and Coleman*, 1980). Based on the classic theory of the generation and evolution of IMF, large-amplitude southward component intervals should be mostly found in these structures (*Dessler*, 1967). However recently, *Borovsky* (2008) came up with a solar wind model formed by flux tubes and the large deviation of magnetic field from the Parker spiral is due to a braiding of magnetic flux tubes (as shown in Figure 3.1). He also suggested that the reconnection at the foot of these flux tubes leads to Alfvénic discontinuities in the solar wind. The turbulence in the solar wind (*Ragot*, 2006), or umdamped Alfvén waves in the interplanetary medium (*Burlaga et al.*, 1982) were proposed to be the source of directional deviations of IMF from the Parker spiral theory.

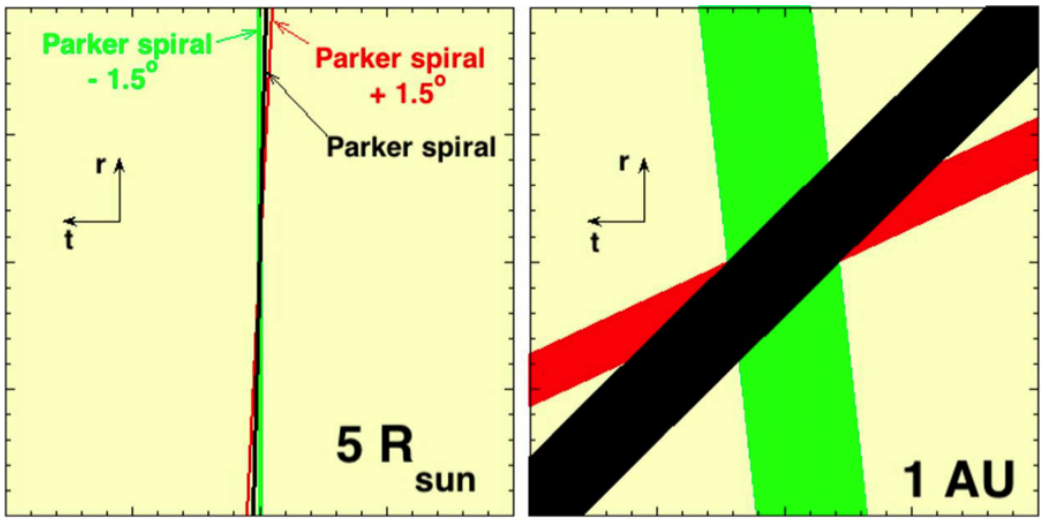

Figure 3.1: In RTN coordinates, the orientations of three flux tubes are sketched at a heliocentric distance of (left) 5 Rs and (right) 1 AU. The black tube is oriented at the local-Parker spiral direction for 400 km/s wind. The red tube is tilted to the right of the Parker spiral, and the green tube is tilted to the left. Transverse expansion of the solar wind increases the diameters of the tubes and increases the misalignment angles. (*Borovsky*, 2008)

A schematic figure of an Alfvén wave is shown in Figure 3.2. If there is a kink perpendicular to the background magnetic field, and the plasma flows in the same direction as the background magnetic field, it is expected to observe a sinusoidal profile of the magnetic field components at a standing point and the same velocity component changing in the opposite direction. However, if the plasma flows antiparallel to the background magnetic field, the time profile of the magnetic field and velocity components is expected to change in the same way.

Alfvén waves were first observed by *Coleman* (1967) based on comparison with an ideal, uniform solar wind model with a wide range of periods in the interplanetary medium. Alfvén waves are commonly observed in all types of solar wind (e.g., *Belcher and Davis*, 1971; *Tu and Marsch*, 1995), and clearly not all Alfvén waves lead to LALD Bs-events. The correlation between the magnetic field and velocity components from solar wind measurements, converted to a parameter called as cross helicity (Alfvénic

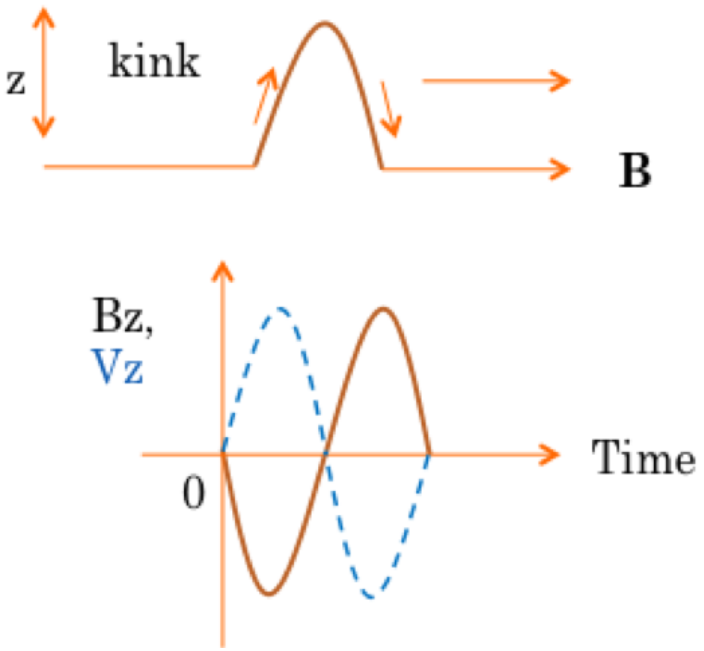

Figure 3.2: A schematic figure of how Alfven waves is generated and time profile of the magnetic and velocity component observed at one point.

effec ratio, (*Matthaeus and Goldstein*, 1982)), has been used widely to detect the occurrence of Alfvén waves in the solar wind, calculated based on the equation below

$$\sigma_c = (e^+ - e^-)/(e^+ + e^-) \tag{3.1}$$

where $e^{\pm} = 1/2\ (Z^{\pm})^2$ and $(Z^{\pm}) = V \pm V_A$, V_A is the Alfvén speed.

Besides the large-scale solar wind transients and Alfvénic fluctuations in the solar wind, the interplanetary small-scale magnetic flux ropes (ISMFRs) (*Moldwin et al.*, 2000; *Feng et al.*, 2010; *Zhang et al.*, 2012) are also sources of LALD southward IMF. ISMFRs observed in the solar wind are defined by their short-durations, which strongly peaks at an hour or less with most lasting less than 4 hours (*Cartwright and Moldwin*, 2008). ISMFR and the large-scale flux ropes in the solar wind - magnetic cloud (MC) not only differ in their temporal and spatial scale, but also in their configuration and evolution, which implies that they may have distinct source mechanisms

(*Moldwin et al.*, 2000). Observationally, MC and ISMFR are distinguished by their durations. The average time duration of MC is $\sim$ 21 hour at 1 AU, and the core field is often twice the background IMF field strength. The combined duration distribution of all solar wind magnetic flux ropes show clearly a bi-modal distribution allowing the identification between MC and ISMFR.

Meanwhile, extensive literature has shown that low-latitude coronal holes (LLCHs) are source regions for HSS, and HSS from such holes catches up with downstream slow solar wind, forming CIRs. Such a structure can be observed as a periodic feature with a $\sim$ 27-day period if the CH is stable (e.g., *Schwadron et al.*, 2005; *Choi et al.*, 2009). At 1 AU, CIRs observational signatures include the solar wind speed increase from slow to fast and the direction of the solar wind changing from east to west indicating the interacting region (IR). The pile up of plasma in IR leads to a local maximum of the IMF magnitude and first increase and then drop to a minimum of the plasma density. Another signature of the CIR observed at 1 AU is the large fluctuations shown in the solar wind velocity and z-component of IMF, indicating large-amplitude Alfvénic structures, which has important implications for solar wind-magnetosphere coupling (e.g., *Kavanagh and Denton*, 2007; *Tsurutani et al.*, 2006). A recent study showed the observational evidence of a small-scale magnetic cloud with a flux rope topology embedded prior to IR in a CIR. They suggested that open magnetic field line footprints in the LLCH in the vicinity of the closed magnetic field lines spreading the photosphere near the neutral line favors reconnection leading to footprint exchange and finally small-scale transients trapped in CIRs, as shown in Figure 3.3 (*Rouillard et al.*, 2009). Several other studies have also shown the presence of other types of small-scale transients inside the slow solar wind due to reconnection events in *Wang et al.* (2000); *Zurbuchen et al.* (2000); *Crooker et al.* (2004); *Kilpua et al.* (2009).

Ko et al. (2006) analyzed the observations from SOHO and ACE and suggested that the boundary region between an equatorial coronal hole and an active region

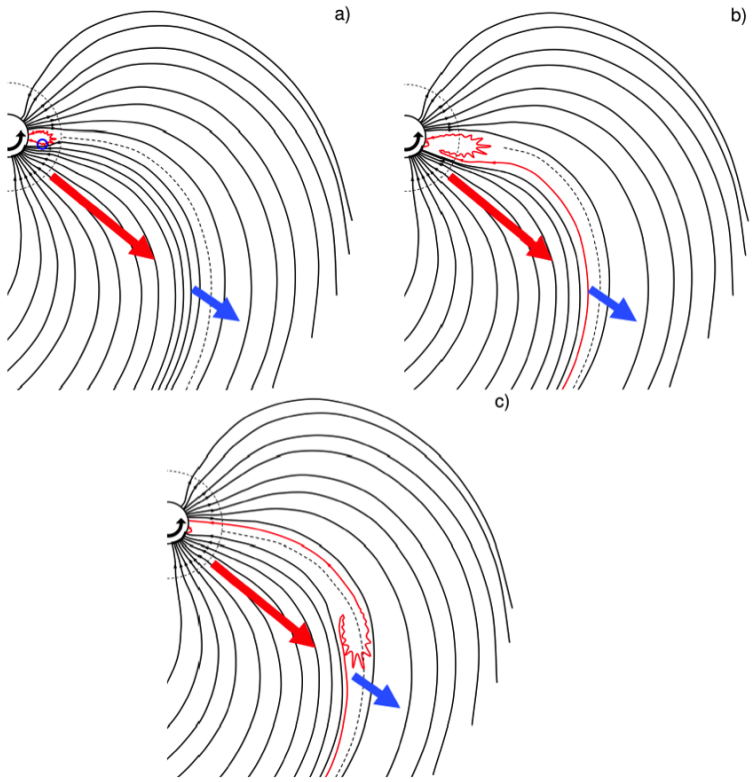

Figure 3.3: A view of the solar equatorial plane during the take-off of a small-scale transient embedded in a CIR. This scenario is inferred directly from the in situ observations of the solar wind measured by STA and consists of a flux-rope emergence (a), reconnection of the flux rope with open field lines (b) and trapping of the small-scale transient inside a forming CIR (c). The HCS is plotted as a dotted black line in each panel. (*Rouillard et al.*, 2009)

(AR) is one source of the slow solar wind, featured as the passage of a fast slow wind followed a slow solar wind observed at 1 AU. The assertion that such regions on the Sun are a possible source of the slow solar wind is also supported by interplanetary scintillation tomographic observations of solar wind (*Kojima et al.*, 1999), and by Hinode X-ray Telescope (XRT) observations (*Sakao et al.*, 2007). *He et al.* (2010) utilized the observations from Hinode,TRACE and ACE investigated the intermittent outflows at the edge of an AR and found that these outflows in the lower corona correspond to the intermediate-speed solar wind stream in interplanetary space. It was shown that the solar origin of interplanetary structures with LALD IMF Bs could be associated with AR in vicinity of the streamer belt and growing LLCH. They also claimed that these interplanetary structures are geoeffective and thus the corresponding phenomena on the Sun could be an important observational tool for space weather prediction. *Choi et al.* (2009) statistically studied the connection of CH, CIR, and geomagnetic storms and showed that the area of geoeffective CHs larger than 0.12% of the solar hemisphere area, and that the CIR-associated geomagnetic storms distribution depends on magnetic polarity which is suggested to be the combined effect of the southward component of the Alfvén waves and the Russell-McPherron effect.

Following in this chapter, we will discuss the relationship between LALD IMF Bs-events and solar wind transients, the effect of the passage of solar wind transients propagating outward on the orientation of IMF, and the potential mechanisms for the solar source of LALD IMF Bs-events.

3.2 The relationship between LALD IMF Bs-events and transient solar wind structures at 1 AU

3.2.1 The identification of solar wind transients related with LALD IMF Bs-events

In order to study the sources of LALD IMF Bs-events, we analyzed the plasma and magnetic field measurements of the IMF Bs-events (for different sets of thresholds of Bs amplitude and duration) in our dataset and compared with the literature of solar wind transients. The detailed methodology is described as following:

(1). Compared with previous studies of different solar wind structures - Stream Interaction Region (SIR), ISMFR, ejecta (*Jian et al.*, 2006a,b; *Richardson and Cane*, 2010) and published lists such as the Interplanetary Shock Database from Center for Astrophysics and Lepping Magnetic Cloud database), we categorize the Bs events from the WIND IMF data (if WIND satellite was crossing the Earth's magnetosphere, we averaged ACE/IMP 8 magnetic field data into 1 min resolution instead of WIND data) into MC, ISMFR, ICME without MC signature (hereafter referred to as ejecta, (*Burlaga et al.*, 2001)), SIR, and Shock if there is an overlap between a Bs event and a solar wind structure. If there is no overlap, we define the Bs event as unrelated with well-defined solar wind structures.

(2). For the MC list, the start and end times were estimated by a magnetic field model (*Lepping et al.*, 1990), assuming that the field within the magnetic cloud is force free using Magnetic Fields Investigation (MFI) data from WIND. For SIR list, the authors calculated the total perpendicular pressure (the sum of the magnetic pressure and plasma thermal pressure perpendicular to the magnetic field) for the WIND and ACE data set and defined the boundary from a combination of signatures described in their paper (*Jian et al.*, 2006a). The main requirement is that the interval covers where the pressure structure emerges from then decays back to the background. The

interplanetary shocks were analyzed using plasma data from Solar Wind Experiment and MFI onboard WIND spacecraft based on the criteria that increases of at least 3%, 20%, and 30% sharply occur in bulk speed, IMF magnitude, and density of downstream compared to the upstream values. The immediate 20 min of data on either side of the shock is used to characterize the upstream and downstream plasma parameters (*Jurac et al.*, 2002). For the ejecta list, the authors set up the boundaries of the events mainly based on a consensus of the solar wind plasma and magnetic field signatures (*Cane and Richardson*, 2003; *Richardson and Cane*, 2010). The ISMFRs were preselected out from the rotation and enhancement of the magnetic field by eye using WIND plasma and field data and then verified by the geometric parameter fit to the cylindrical constant-alpha force-free field (*Feng et al.*, 2008). Limited by the date range of the lists available, the distribution of Bs events in these groups is examined from 1995 to 2004.

In order to understand if there is any relationship between Bs events not overlapping with well-defined solar wind structures and well-defined solar wind structures, we examined the temporal separation of Bs event (longer than 1 h and stronger than -5 nT) to solar wind structures. We found that the shortest separation of a Bs event not overlapping with any well-defined solar wind structure is 20 min from a flux-rope-type Bs event, 15 min from an ejecta Bs event, 10 min from a Shock-type Bs event, and 1 h from a SIR-type Bs event. Out of the 89 MC-related IMF Bs events, there are 36 events occurring within 3 days of the MC structure. There are seven out of 11 ISMFR-type Bs events, 46 out of 241 ejecta-type Bs events, 48 out of 206 SIR-type Bs events, and eight out of 12 Shock-type Bs events that occur within 3 days of the solar wind transient structure. For the Bs events with separation less than 3 days, the average of the time separation is about 14 h for MC-type Bs events, 27.5 h for ejecta type, and about 36 h for SIR type. We investigated the Bs events that occurred within an hour of a solar wind structures and found that they are distinct intervals

rather than part of a complex structure.

(3). For the Bs events showing no features of ICME, shock, or SIR from steps 3 and 4, perform linear regression between the magnetic field and velocity field for the x, y, and z components in GSE coordinates; if the slopes of all three components have the same order (the difference between the largest and smallest value of slope is no more than 100%), this event is considered Alfvénic wave related; if one or two components change only slightly in both magnetic and velocity fields, while the other two or one components show a good linear relationship, this event is also categorized as Alfvén wave related. For further confirmation, we calculate the cross helicity and require it to be > 0.5. If the fluctuation of the corresponding magnetic field and the velocity vectors has positive/negative correlation when the longitudinal angle of the IMF is negative/positive, the Alfvén wave is propagating outward; otherwise, it is inward.

3.2.2 Association of LALD IMF Bs-events with solar wind transients

Figure 3.4 illustrates the distribution of total duration of Bs events in MC, ISMFR, ejecta, SIR, Shock, and those unrelated with well-defined solar wind structure (including Alfvénic fluctuations). The minimum value of IMF Bs magnitude and the event duration are shown at the top of each subfigure. The structure type is shown at the right side in each plot. We find that for the Bs events that last more than 1 h with maximum Bz value as zero, the cases unrelated with well-defined solar wind structure are dominant (nearly 70%). As the threshold of the duration and magnitude of Bs increase, the proportion of MC-type Bs events increases. The contribution of ejecta-type Bs events is also smaller as the duration is longer when the maximum Bz is -10 nT. The Bs events in the ISMFR group only occur in the category of events with duration less than 1 h and Bs intensity less than 5 nT. The Shock-type Bs events also never exceed 3% of any of the distributions. It is noteworthy that for the Bs

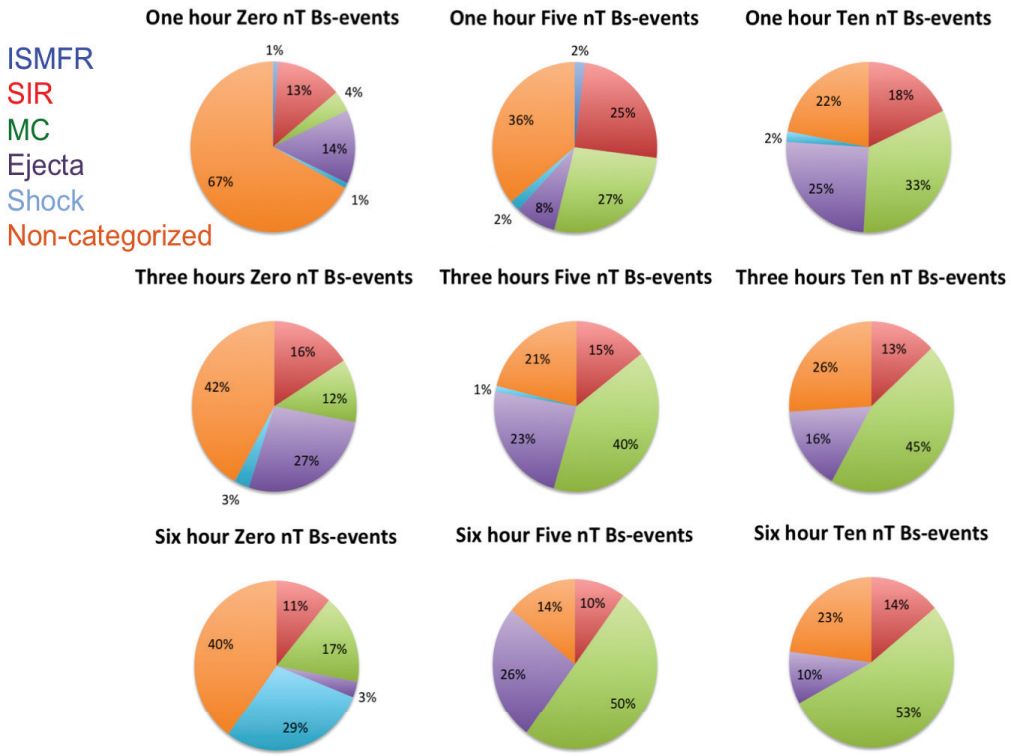

Figure 3.4: The distribution of total duration of Bs events in MC, ISMFR, ejecta, SIR, Shock, and other cases.The minimum value of IMF Bs magnitude and the event duration is shown at the top of each subfigure. The marker type is shown at the right side of each plot.

events that are longer than 6 h and have minimum Bs value of -10 nT, the MC-type Bs events become the majority (53%); however, nearly one quarter of the intervals are not associated with well-defined structures such as flux ropes, ejecta, SIR, or Shock, and 10% are related to ejecta.

3.2.3 Association of LALD IMF Bs-events with Alfvénic fluctuations in the solar wind

Figure 3.5 gives an example of an Alfvén wave-related Bs event observed by the ACE satellite at 1 AU on 19 November, 2002. The time period shown in the plot is 19:00 - 24:00 UT 19 November, 2002, while the Bs event is from 20:30 to 22:50 UT marked by the dashed lines. During this Bs event, the magnitude of the total

magnetic field and Bx did not change significantly but averaged about 11 and 3 nT, respectively. IMF By showed an increase from -5 nT to 5 nT during the first half of the Bs interval and then decreased to $\sim$ -10 nT until the end of this interval. Between the dashed lines in Figure 3.5c, the solar wind speed fluctuates around 390 km/s, while the component in the Sun-Earth direction varied simultaneously with the magnitude. It is seen from Figure 3.5d that there were sign changes of the z component of solar wind velocity in the same direction as the corresponding magnetic field component, which is also seen in the y component of both the magnetic field and solar wind velocity. We also examined the solar wind conditions over the solar rotation that covers this Bs event, showing that the solar wind speed remained around 400 km/s for 3 days before this event and a SIR occurred 2 days later. The pitch angle distribution of suprathermal electrons is peaked at 180°, that is antiparallel to the magnetic field over the whole interval, indicating an inward IMF sector.

Figure 3.6 shows the linear regression of the x-, y-, z- components (from top to bottom) between magnetic field and velocity for the event shown in Figure 3.5. The scattered dots are magnetometer and velocity observations from ACE, and the straight line shows the linear regression result. The equation and correlation coefficient of the linear regression are shown in each panel. The correlation coefficients for x-, y-, z- component are 0.83, 0.90, and 0.95, while the slopes are 0.16, 0.17, and 0.22, respectively. Combined with the fact that the longitude angle of the IMF during this interval almost stayed at -45°, the observations are consistent with Alfvén waves propagating anti-parallel to the magnetic field, or anti-sunward within an inward polarity IMF sector. We also calculated the cross helicity as 0.78 for this Bs-event (which is not shown in the plot).

Figure 3.7 shows the histograms of the properties of the 57 Alfvénic fluctuation related IMF Bs-events. Panel (A) shows that for 62 % of these Bs-events, the average IMF magnitude is less than 8 nT, but that 5 events have amplitudes greater than 12

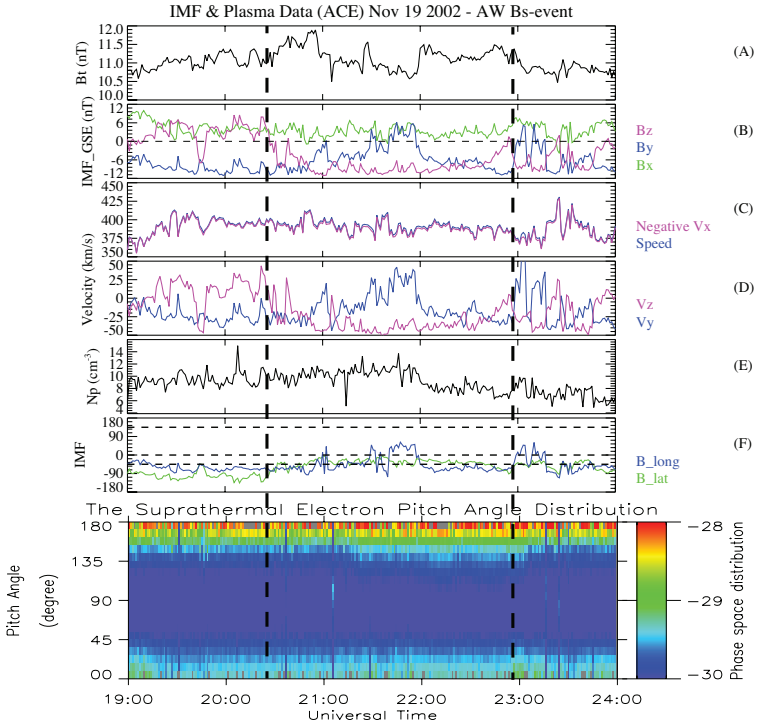

Figure 3.5: An example of an Alfvén wave related Bs-event observed by the ACE satellite at 1 AU. From top to bottom, panels show the (A) total interplanetary magnetic field (IMF) magnitude; (B) IMF x-, y-, z- components in GSE coordinates; (C) solar wind speed and negative x- component of solar wind velocity in GSE coordinates; (D) y-, z- components of solar wind velocity in GSE coordinates; (E) solar wind proton density; and (F) suprathermal electron pitch angle distribution at 272 eV.

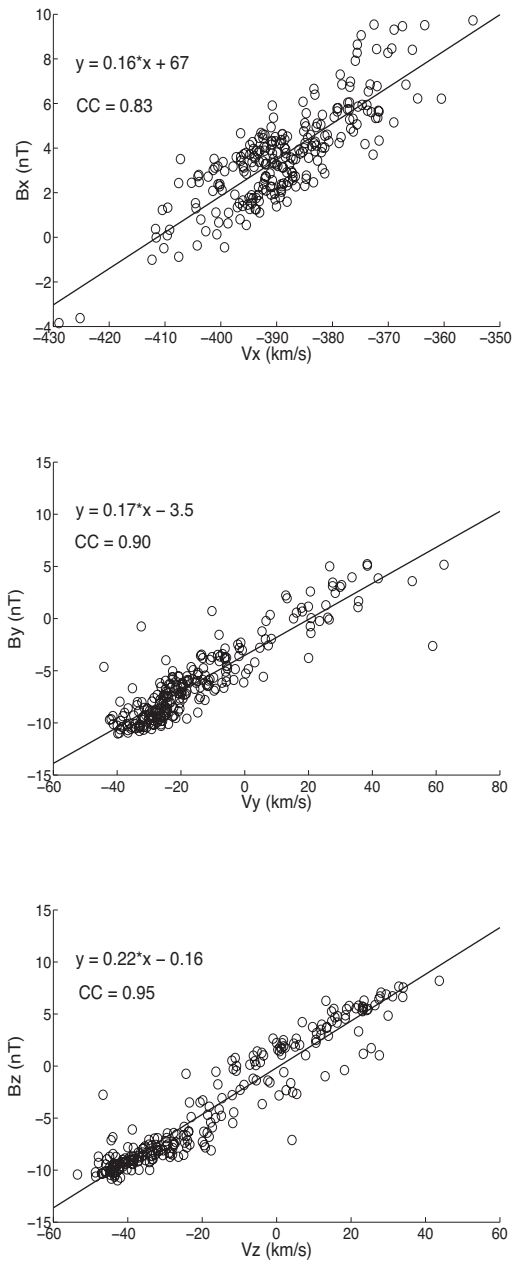

Figure 3.6: The linear regression of x-, y-, z- components (from top to bottom) between magnetic field and velocity for the event shown in Figure 3.5. The scattered dots are observations from ACE, and the solid line shows the linear regression result. The equation and correlation coefficient of the linear regression are shown in each panel.

nT. It is indicated from panel (B) that only 22% of them propagated in solar wind with speed of more than 500 km/s, while over half of them occurred in solar wind with speed less than 400 km/s. The velocity distribution is peaked between 375 - 400 km/s. There are data gaps in proton density for 9 events, so the total numbers of the counts in panels (C), (D) and (E) are 48. The histogram in panel (C) shows that three quarters of these events have mean proton density smaller than 8 cm^{-3}, with a most probable density of 6 cm^{-3}. Based on the measurements of magnetic field and proton density, we calculated the Alfvénic speed (V_A) during the intervals shown in panel (D) and found that 75% have V_A less than 80 km/s, and peaked at V_A = 70 - 80 km/s. Using the definition of cross helicity (*Matthaeus and Goldstein*, 1982), we show in panel (E) that the absolute value of the cross helicity is less than 0.6 for only 1/6 of events, and that the most frequent occurrence is at 0.8. We plot the correlation coefficients (CC) of the linear regression between the magnetic and velocity fields for all three components of all the 57 Bs-events in panel (F). It is shown that about 74% of these intervals have CC higher than 0.7 between the two fields, which is an important criterion for identifying Alfvénic fluctuations in the solar wind.

To further check if there are solar wind structures (ICME, shock, and SIR) present that were not captured by the published lists, we examined the ion moments and suprathermal electron (STEA) pitch angle data from ACE for features related to ICMEs, shocks, or SIRs during the LALD IMF Bs-events that were not recognized in previous published lists; if the measured proton temperature is significantly lower than the expected temperature based on the solar wind speed during intervals not near the heliospheric current sheet (e.g., *Gosling et al.*, 1973; *Richardson and Cane*, 1995), or the STEA pitch angle in the energy channel of 272 eV shows a bidirectional distribution not associated with Earth's bow shock or a SIR (e.g., *Zwickl et al.*, 1983; *Gosling et al.*, 1987), this interval is categorized as an ICME; if there is a sharp increase of proton density, speed, temperature, and IMF magnitude, this event is

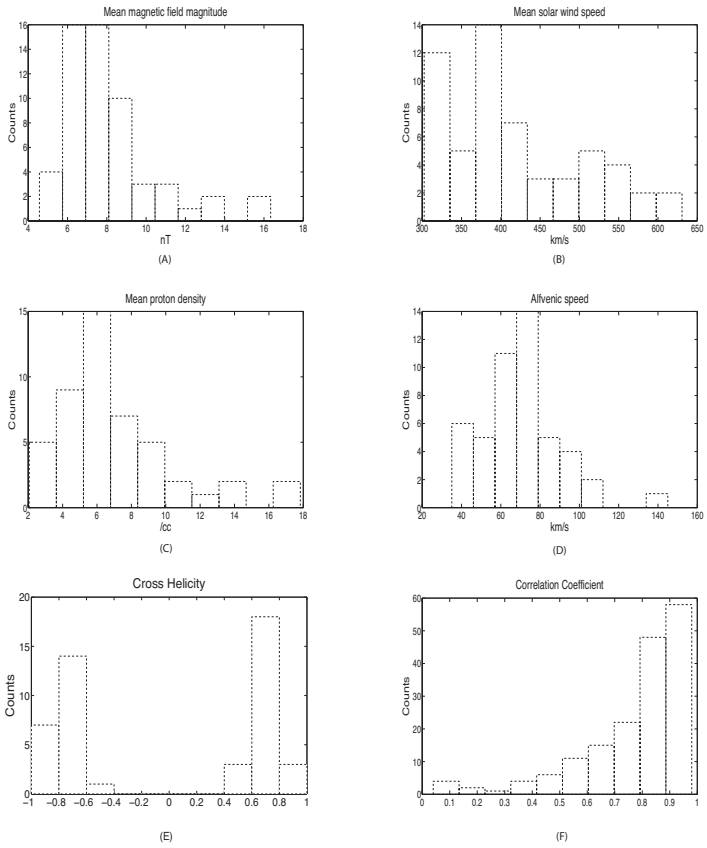

Figure 3.7: Histograms of mean values of the IMF magnitude (A), solar wind speed (B), proton density (C), Alfvénic speed (D), cross helicity (E), and correlation coefficient (F) for the Alfvénic fluctuation related IMF Bs-events

Table 3.1:

	MC	Ejecta	SMFR	SIR	Shock	AW	Unidentified
Previous study	64	209	5	149	13	–	172
Current study	64	237	5	151	15	57	83

considered shock associated; if there is a gradual increase of solar wind speed from the background average value ($\sim$ 400 km/s) to over 500 km/s, and decrease of proton density, the event is labeled as a SIR.

Table 1 shows the number of Bs-events (t $>$ 1 hour, Bz $<$ -5 nT) during the period of April 1998 - Dec 2004 in each category of solar wind transients and Alfvénic fluctuations. It shows that there are 28 Bs-events identified as ejecta, 2 as SIRs, and 2 as shocks in this study that were not previously identified in published event lists. This study again finds that most Bs-events are associated with ejecta, while about 10% of Bs-events are associated with Alfvén waves where there are no other concurrent and predominant solar wind features. However, $\sim$ 14% of Bs-events are still not associated with any of these solar wind structures.

3.3 Association of LALD IMF Bs-events with solar wind transients beyond 1 AU

It is shown in the red bars comparing the top and bottom panels in Figure 3.8 that at $\sim$ 5 AU, SIR contributes to the IMF Bs-events significantly more than ICME when the duration threshold is set to 4 hours. Comparing the red and blue bars in the top panel, it is presented that the occurrence rate of IMF Bs-events related with SIR is almost always twice at $\sim$ 5 AU as that at 1 AU in terms of different duration. While the frequency of ICME-related IMF Bs-events beyond 5 AU is less than half of that at 1 AU from the bottom panel. For the IMF Bs-event that last for more than 5 hours, the occurrence rate is higher embedded in ICMEs at both 1 AU and $\sim$ 5 AU than embedded in SIRs. We find that the magnetic field southward component

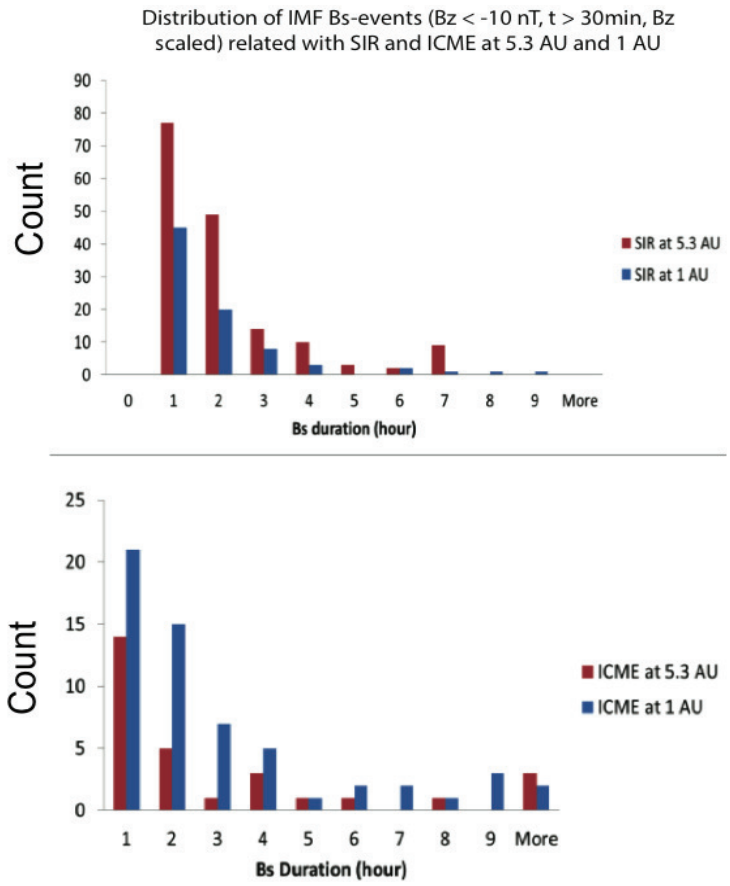

Figure 3.8: The distribution of IMF Bs-events duration (Bz < -10 nT, t > 30 min, Bz at Ulysses has been scaled by multiplying with 5.3) related with SIRs (top) and ICMEs (bottom) based on the measurements from Ulysses traveling at 5.3-5.4 AU near the ecliptic plane (Figure 2.2) and from ACE at 1 AU.

in the ICME structures tends to diminish more quickly than that in the SIRs as the solar wind propagates outward.

As mentioned, there are LALD IMF Bs-events related with Alfvénic fluctuations at 1 AU, which is also observed beyond 5 AU by Ulysses. Figure 3.9 illustrates the radial (top), tangential(middle), and normal(bottom) components of the mangetic field and solar wind velocity at $\sim$ 5 AU measured by the VHM and BAI instruments onboard Ulysses for an IMf Bs-event related with Alfvénic fluctuations in the solar wind. It is shown that IMF z-component keeps at -1.0 nT as the principle component for about 2 hours, which corresponds to an IMF Bs-event at least with Bs < -5 nT, t > 2 hrs at 1 AU in scale of amplitude. While the time resolution of the magnetic

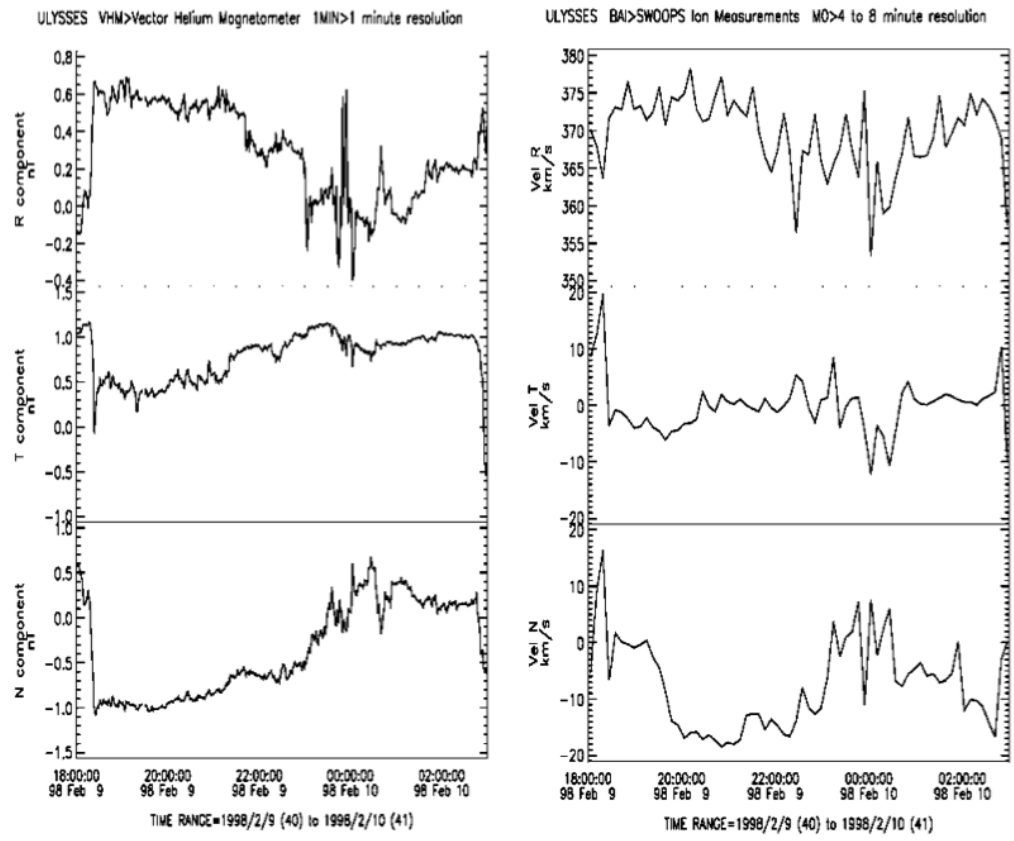

Figure 3.9: An example of IMF Bs-event related with Alfvénic fluctuations beyond 5 AU on Feb 9 1998. The magnetic field components (left) and solar wind velocity components (right) in the RTN coordinates measured by Ulysses VHM and BAI instruments. The radial, tangential, and normal components are displayed from top to bottom respectively.

field (1 min) is higher than the velocity (4-8 mins), it is shown from Figure 3.9 that the two parameters change in a similar way simultaneously.

Figure 3.10 shows the linear regression of the r-, t-, n- components (from top to bottom) between magnetic field and velocity for the event shown in Figure 3.9. The scattered dots are magnetometer and velocity observations from Ulysses, and the straight line shows the linear regression result. The linear regression function are shown in each panel. The slopes for r-, t-, n- component are 0.027, 0.024, and 0.028, respectively. Combined with the fact that the longitude angle of the IMF during this interval almost stayed at -45°, the observations are consistent with Alfvén waves

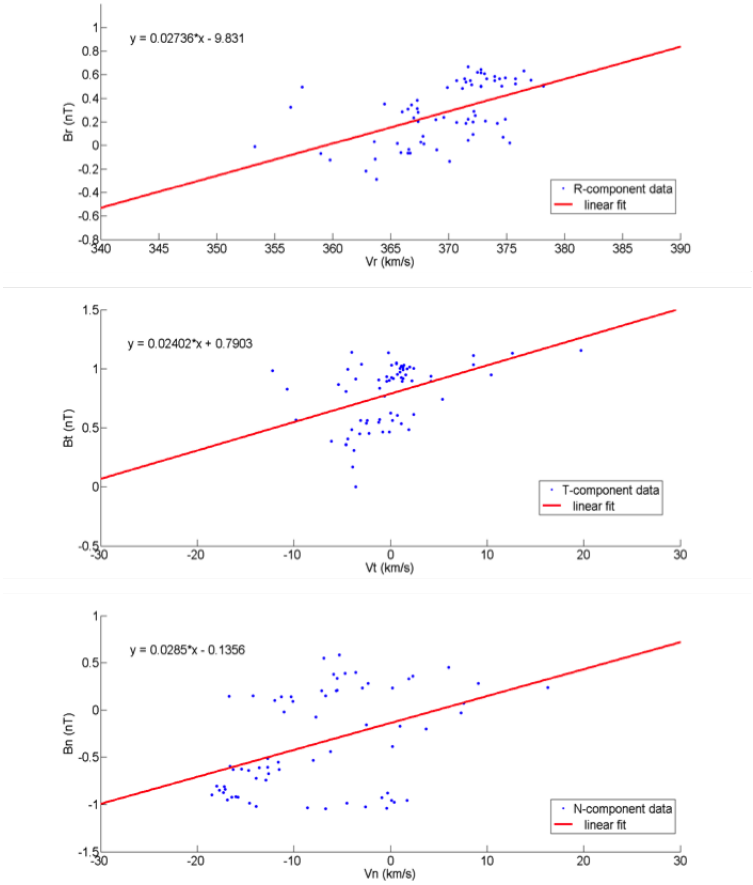

Figure 3.10: The linear regression of r-, t-, n- components (from top to bottom) between magnetic field and velocity for the event shown in Figure 3.9. The scattered dots are observations from Ulysses, and the solid line shows the linear regression result. The linear regression function are shown in each panel.

propagating anti-parallel to the magnetic field, or anti-sunward within an inward polarity IMF sector.

3.4 Potential techniques for detecting the solar source for LALD IMF Be-events

We have shown the relationship between the LALD IMF Bs-event and different types of solar wind transients comparing their features based on the in situ satellite data. We also analyzed other data sources in order to further investigate the

solar/interplanetary sources of the emergence of this component.

3.4.1 Low-latitude coronal hole with adjacent active region is the source region of LALD IMF Bs-events

The flux rope configuration within an ICME contributes to the LALD IMF Bs-events is widely demonstrated, while the mechanism for how the IMF is oriented toward southward for a long time embedded in a SIR is still in debate. In order to study the solar or interplanetary sources of the LALD IMF Bs-events related with SIRs, we did a preliminary analysis focusing on the corotating interaction region (CIR) associated events since CIRs are recurring and more trackable structures than other types of SIRs. The detailed methodology is described as following:

(1). We identified CIRs based on the published lists (e.g., *Choi et al.*, 2009; *Mason et al.*, 2009; *Ebert et al.*, 2012) and generally accepted definition of CIRs as the downstream region of the forward and reverse shock or waves (*Hada and Kennel*, 1985). When a CIR sweeps around the satellites, the plasma density, temperature, magnetic field amplitude, and solar wind bulk speed increase suddenly across the forward shock. The interface region (IR), which is the boundary between the slow solar wind and the HSS, is located within the CIR between the forward and reverse shocks. Across the IR, temperature and solar wind speed increase while proton density decreases (*Richardson et al.*, 1996, 1998). We applied these conditions to the identification of CIRs using observations from ACE and STEREO.

(2). Based on the lists of identified CIRs, we obtained the maximum of the HSS following the CIR and the minimum of the low speed stream preceding it - the radial solar wind velocity at the two ends of IR, then we took the arithmetic mean velocity from the two values as being representative of the radial velocity of the CIR, V_r. We assumed that the adjacent sources of fast and slow solar wind would continue to emit coronal plasma at these same velocities. Under this assumption, we can use the

following equation to estimate the expected travel time, Δt, from source region of the CIR on the solar surface to the observation of the CIR at the spacecraft or the expected travel time between the observations of CIR at two spacecraft based on the method used by (e.g., *Richardson et al.*, 1998)

$\Delta t = \frac{\delta r}{V_r} + \frac{\delta \beta}{\omega_{sun}}$,

where δr is the radial distance of the spacecraft from the Sun or the distance between the two spacecraft, which is assumed constant for the duration taken for the CIR to propagate, and $\delta\beta$ is the angle between the source region when it emits from the Sun and the current meridian plane or the angle between the two spacecraft in terms of solar longitude, again assumed to be constant for the duration of the event. Here ω_{sun} is the equatorial rotation rate of the Sun, approximately 14.4° day^{-1}, equivalent to a complete solar rotation every 25 days. Using the above equation and the knowledge of the time of observation of the CIR at one spacecraft we are able to calculate an approximate arrival time of the CIR at another two satellites (ACE, STA, and STB). It should be noted that this will not be the same plasma as observed at the reference point, unless there is radial alignment, but plasma that is part of the same overall CIR front.

(3). We traced the CIR observations at the three satellites back to the solar surface and compared with the solar extreme ultraviolet (EUV) images to search for the corresponding low-latitude coronal hole (LLCH), if there is any, as the source region of the HSS part of the CIR. Note that we used the images from SOHO or SDO to represent that captured at ACE. We also compared the expected travel time between the three satellites of CIRs adjacent in time series, as well as the images of the corresponding LLCHs, and obtained a list of CIRs observed by the three satellites in a sequence from the same source region.

(4). We checked for the occurrence of LALD IMF Bs-event (Bz $<$ -5 nT, t $>$ 1 hour) in the duration of the CIRs from the list using the in situ plasma and magnetic

field measurements from the satellites.

(5). Combined the images from X-ray Telescope (XRT), the records of active regions (AR), and the EUV instruments onboard STEREO and SOHO/SDO, we searched for the emergence of an AR or ARs or brightened loops adjacent to the LLCH that are inferred as the source region of the CIRs.

Figure 3.11 shows the EUV images (195 $\mathring{A}$) captured by STEREO-B on June 12, 2008 (left), SOHO one day later and STEREO-A on June 16. The white boxes represent the region of a LLCH with adjacent AR as the source region of CIRs sweeping the three satellites and ACE spacecraft deduced from the above equation. We obtained the information about the ARs from the Raben Systems, Inc. website (https://www.raben.com/maps). They provide the solar maps showing the current active region numbers and locations assigned by the National Oceanic and Atmospheric Administration (NOAA) Space Weather Prediction Center (SWPC), and the information of the activity level and hazard potential of the AR designed by the NASA Space Radiation Analysis Group. The AR shown in the box is numbered as 10998, and the magnetic classification is alpha on June 12 (observed by STB, left), which means a unipolar sunspot group according to the Mount Wilson Sunspot Magnetic Classification. When the AR rotates with the Sun facing to the SOHO spacecraft on June 13, its magnetic classification is coded as beta, indicating a sunspot group having both positive and negative magnetic polarities (bipolar), with a simple and distinct division between the polarities. It diminishes to a plage when moving to the field-of-view of STA on Jun 16. During the evolution of AR 10998, there is no historical record of CME or flare eruption. It is also shown that this LLCH spans a wide longitudinal range, and consists of one large and one small size CH connected by the AR. The shape of the LLCH changes from left to right, but not significantly.

Figure 3.12 shows the local measurements of the magnetic field and plasma obtained by the STEREO and ACE spacecraft when the CIR, which is emitted from

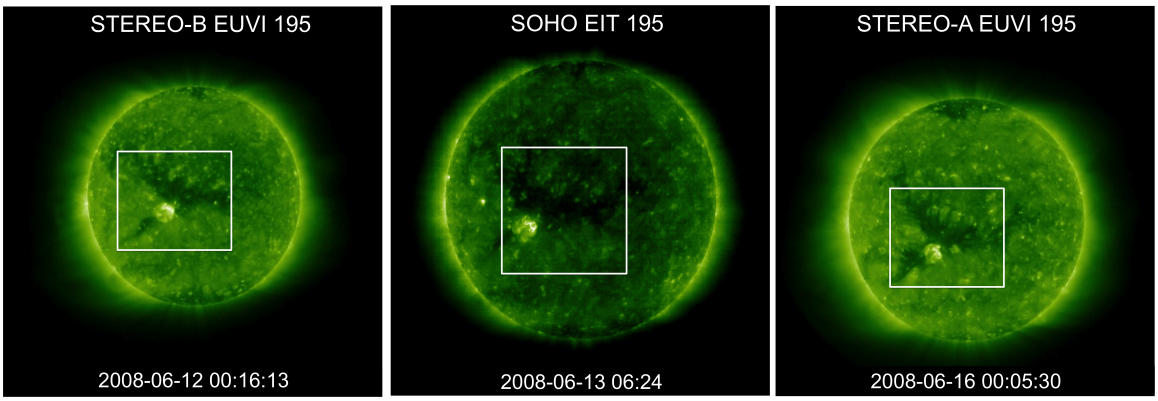

Figure 3.11: The EUV images (195 $\mathring{A}$) captured by STB on Jun 12, 2008 (left), by SOHO EIT on June 13 (middle), and STA on Jun 16 (right). The region of LLCH and the adjacent AR is marked as the white boxes. The LLCH is inferred as the source region of CIRs observed by the three satellites.

the LLCH in Figure 3.11, sweeps by the satellite. From the profiles, the CIR was observed by STB first, then ACE, and finally STA. The duration of the LALD IMF Bs-event within the CIRs is denoted by the two vertical lines in each panel. It is illustrated that the IMF Bs-event observed by STB lasts for about 5 hours with minimum value about -10 nT, and that the duration of the event from ACE is about 2 hours with minimum Bz $\sim$ -18 nT, while STA observed an IMF Bs-event continuing for less than 2 hour with minimum as -10 nT. From the top panels, it is presented that the magnetic field strength has a peak in the interval of the IMF Bs-event observed at all the three satellites, and the difference between the minimum and maximum values of the total magnetic field is 6 nT, 8 nT, and 5 nT from left to right respectively. The density measured by STB in the third panel (left) experiences a change in the similar way as the magnetic field amplitude, while the solar wind bulk speed is almost constant. The solar wind velocity measured by ACE is increasing smoothly from 450 km/s to 500 km/s, proton density shows a peak as the magnetic field strength. When the IMF Bs-event was observed by STA, the plasma density sees a local minimum, while the solar wind speed changes a little. It is indicated that the IMF Bs-event was embedded in the slow solar wind before the IR when the CIR propagates to STB,

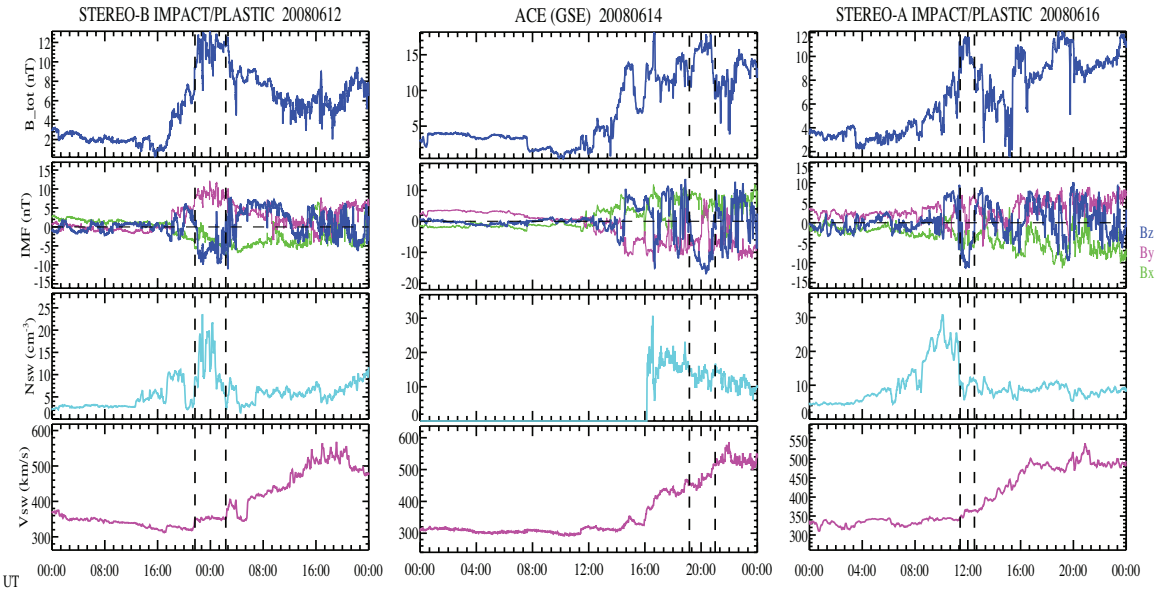

Figure 3.12: The in situ magnetic field magnitude and components (in GSE coordinate), plasma density and solar wind speed measurements (top to bottom) for the CIR generated by the LLCH in Figure 3.11 from STB (left), ACE (middle), and STA (right) when it sweeps by the satellite. The time range for STB observations is from June 12 00:00:00 to June 14 00:00:00, for ACE from June 14 00:00:00 to June 15 00:00:00, and for STA from June 16 to June 17. The two vertical dashed lines mark the LALD IMF Bs-events embedded in the CIRs.

while right in the IR when observed at ACE, and at the edge between the slow solar wind and IR when the CIR sweeps around STA.

The first four rows in Table 2 present the number of CIRs observed by STEREO and ACE during April 2007 - December 2008 tracing back to LLCH with and without adjacent AR in the EUV images from STEREO, and the none-adjacent AR category divided into two subcategories based on occurrence of nearby brightened loops. The last two rows show the number of CIRs with and without observations of IMF Bs-events based on ACE data. The columns are divided into three types according to the detection of IMF Bs-events at the two STEREO spacecraft. It is presented that there is only 1 out of 27 CIRs emitting from a LLCH with adjacent AR showing no observations of IMF Bs-event at either STA or STB. There are 17 CIRs embedded

Table 3.2:

	Only STB or STA	Both	Neither
CH w/ nearby AR	12	14	1
CH w/o nearby AR	12	9	9
Brightened loops	6	3	3
No Brightened loops	6	6	6
ACE Bs-event	15	18	6
No ACE Bs-event	9	5	4

with IMF Bs-events observed by both STEREO satellites that are related with source region of LLCH with adjacent AR or brightened loops, compared to 6 cases from source region without any bright features nearby the LLCH region. There are 47 CIRs with IMF Bs-event measured at either STA or STB or both, out of which 35 ($\sim$ 74%) cases are solar wind propagating outward from LLCH with nearby AR or brightened loops. Compared with the ACE measurements, there are 5 CIRs not showing IMF Bs-event out of the total 23 CIRs that embed with IMF Bs-events observed by both STEREO satellites.

3.4.2 Heavy ion charge status as indicators for the source region of LALD IMF Bs-events

Our results also show that there are some events identified as ICME or SIR based on our study but missing from previous publications, which also contribute to the occurrence of LALD IMF Bs-events. We present the superposed epoch analysis of the heavy ion charge states for the IMF Bs-events based on the SWICS measurements (1-hour resolution) from ACE. Figure 3.13 illustrates the SEA results of He^{++} density (A), Carbon charge ratio (B), Oxygen charge ratio (C), and Averaged Ion Charge Ratio (D) for the IMF Bs-events (Bz $<$ -5 nT, t $>$ 1 hr) related with ICMEs , SIRs, Alfvénic fluctuations, and ICMEs not in published literature. *Zurbuchen and Richardson* (2006) summarized the in situ signatures of ICMEs at $\sim$ 1 AU heliospheric distance in the magnetic field, plasma composition, plasma waves, and suprathermal

particles. (e.g., *Bame et al.*, 1978; *Lepri et al.*, 2001; *Lepri and Zurbuchen*, 2004) have demonstrated that the high Fe charge states - averaged Fe charge state > 12 - is one of the indicators of ICME. *Schwenn et al.* (1980); *Gosling et al.* (1980); *Gloeckler et al.* (1999) have shown that if the density ratio of He^{+} to He^{2+} is bigger than 0.01, the solar wind is identified as part of ICME. It is suggested that the elevated oxygen charge state - $O^{7+}/O^{6+} > 1$ - could be used as the feature of ICME (e.g., *Henke et al.*, 2001). Although the parameters suggested for identification of ICME are different, these studies and others have shown that the ion charge states are better indicators than in situ solar wind/IMF measurements to distinguish an ICME most of the time. Studies have also shown that the oxygen charge states - $O^{7+}/O^{6+} = 0.145$ - could be used as the criterion to identify streamer-stalk solar wind and non-streamer-stalk wind. The streamer-stalk region is defined as the narrow region in the middle of the streamer belt and underlie the heliospheric current sheet, which has the highest density fluctuations and the lowest solar wind speeds (*Gosling et al.*, 1981; *Borrini et al.*, 1981). Correspondingly, any other non-transient wind, including slow solar wind from the outside of streamer-stalk regions, fast wind from coronal holes, etc, are referred as non-streamer-stalk wind (*Zhao et al.*, 2009). It is shown in Figure 3.13 that none of the ion charge state parameters present significant change in the 2-day interval for the Alfvénic fluctuation related IMF Bs-events. The three quartiles in top three panels for the results of IMF Bs-events embedded in SIRs present smooth decrease across the zero epoch time - the occurrence of IMF Bs intervals, indicating the transition from streamer-stalk wind to non-streamer-stalk wind. It is also shown in the first and last subfigures that the averaged Fe charge states increase across the zero-epoch time, the published ICME related IMF Bs-events also show clear increase in the oxygen charge ratio. Since the cases in the newly identified ICMEs are relatively shorter in duration than the published lists, the low-resolution plasma data (1-hour) makes it difficult to investigate the features in the duration of the IMF Bs intervals.

However, it could be concluded that the ion charge state features, even currently hourly data available for most cases, are good indicators of the source region of the solar wind based on the analysis of in situ measurements.

3.5 Discussions and Conclusions

Prestes et al. (2006) performed spectral analysis of sunspot number and geomagnetic indices and found that the annual average of antipodal activity (aa) shows a dual-peak structure, one near sunspot cycle maximum and the other in the descending phase. They proposed that the first peak is caused by CMEs while the second one resulted from coronal hole fast streams. The dual-peak phenomenon is also present in our study for IMF Bs and is more significant if the duration of the Bs event is longer. Analyzing the yearly distribution of IMF Bs intervals for different categories, we find that the contribution to the second peak is mainly from the SIR and Bs event unrelated with well-defined solar wind structure. The cross-correlation analysis of sunspot number (Rz) and aa in (*Prestes et al.*, 2006) implies that the maximum value of aa lags that of Rz by a year; however, IMF Bs event occurrence is peaked 1 year ahead of Rz in our results for the main peak. We show that the dominant contribution to the LALD IMF Bs events is from transient solar wind structures (MC, ISMFR, ejecta, SIR, Alfvénic fluctuations). We also find that most of the LALD IMF Bs intervals unrelated with these solar wind transients began or ended with a discontinuity or slow shock.

Marsch and Tu (1990) analyzed the magnetic field and plasma data from the Helios spacecraft between 0.3 and 1 AU near the quiet phase of solar cycle 21 and found that in the solar wind fluctuations with frequency below 3×10^{-4} Hz are found in low-speed flows bordering the heliospheric current sheet, and that the fluctuation spectrum at low frequencies drops much faster in fast streams than in slow streams. In this study, we find that the distribution of the Alfvén wave (AW) related Bs-events

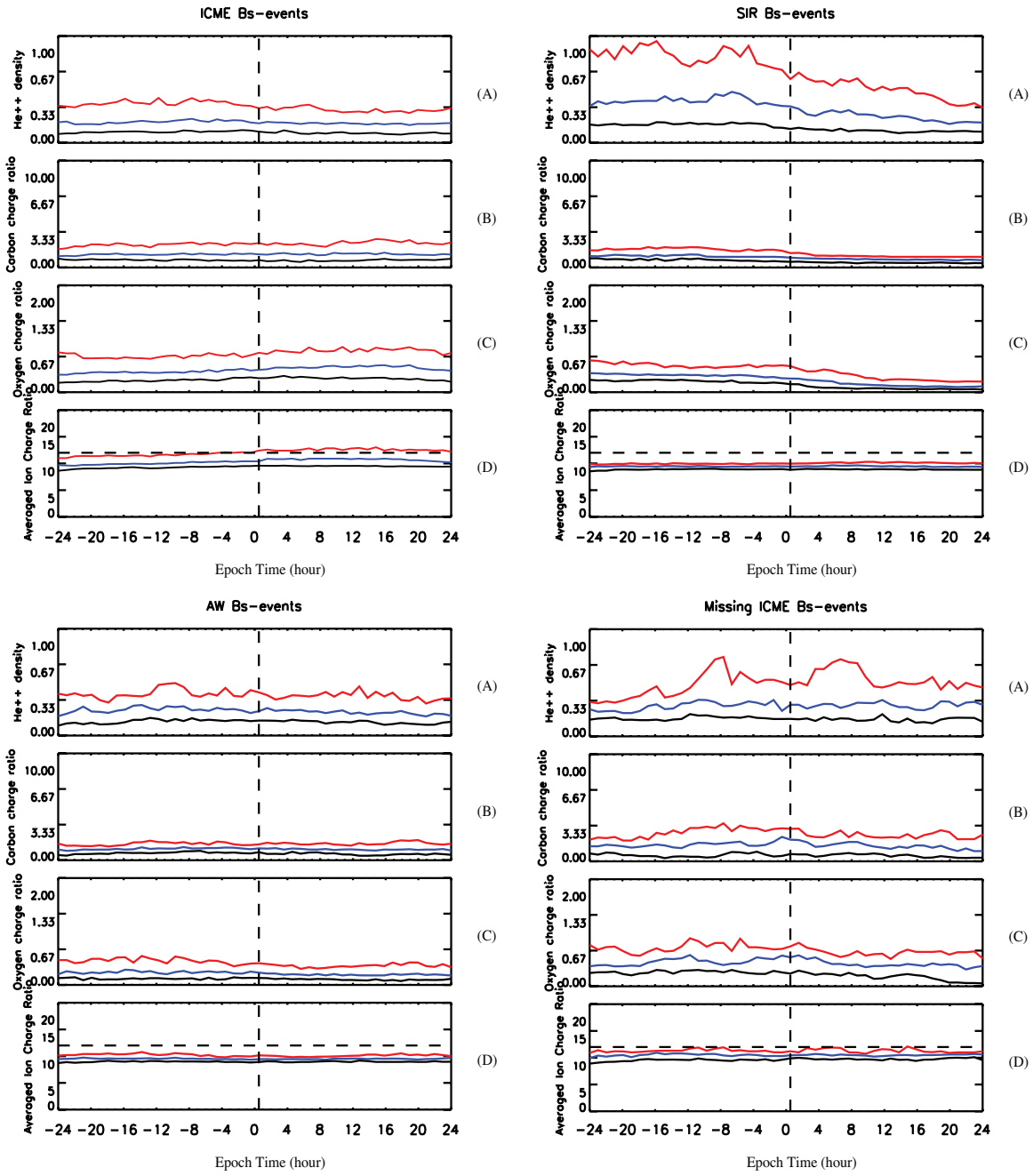

Figure 3.13: The superposed epoch analysis of He^{++} density (A), Carbon charge ratio (B), Oxygen charge ratio (C), and Averaged Fe Charge Ratio (D) for the IMF Bs-events (Bz < -5 nT, t > 1 hr) associated with ICMEs , SIRs, Alfvénic fluctuations, and ICMEs not identifies in previous studies, in the same format as Figure 2.10. The epoch zero is set at the change of IMF Bz drops below -5 nT denoted by the dashed vertical line, and the duration is 48 hours. The red/blue/black lines are the temporal profiles of upper/middle/lower quartile of these parameters.The horizontal dashed line in the bottom panel in each figure marks the averaged Fe charge ratio as 12.

duration is peaked at 2 hours (7.2×10^3 sec, or 1.4×10^{-4} Hz in frequency), which is in the low-frequency range of Alfvén waves. Nearly 80% of these Bs-events are embedded in solar wind slower than 500 km/s. We assume that the low-frequency Alfvén waves carrying LALD Bs intervals in our study originate as perturbations in the magnetic field on the Sun and propagate outward. If Alfvén waves in the solar wind have different source regions in the solar corona, which in turn affect their efficiency in accelerating the solar wind, the differences will be manifested in different spectra and plasma properties in the solar wind at further heliocentric distance.

We have shown the low-latitude coronal hole (LLCH) with nearby solar activities in the closed magnetic field configuration, such as active region (AR) and brightened loops, is the solar source of CIR with LALD IMF Bs intervals. In Figure 3.3, we have shown that *Rouillard et al.* (2009) put forward a model that the reconnection between the open and closed field lines at the footpoint of the transition region of a CIR accounts for the small-scale flux rope configuration in within the CIR. In order to investigate the possibility of this mechanism, we did a Grad-Shafranov (GS) reconstruction analysis for the intervals containing the IMF Bs-events shown in Figure 3.10. The GS reconstruction method has been widely used in space physics community in different areas. It has been often used on structures in space plasmas that can be described in the approximation of MHD such as the magnetopause, flux transfer events, flux ropes in the Earth's magnetotail, as well as magnetic flux ropes and magnetic clouds in the solar wind. (*Hu and Sonnerup*, 2002; *Sonnerup et al.*, 2006) Its main point is to assume invariance and time-independency so the MHD equations in equilibrium, including plasma pressure, can simply be numerically integrated as an initial value problem. The steps for the GS reconstruction analysis, the original data is processed by the deHoffmann Teller (dHT) and Minimum Variance Analysis (MVA), which gives the minimum variance direction as the first approximation to search for the GS axis. If the electric field measured in the instrument frame is $\boldsymbol{E}$, then the

electric field in the HT frame, assuming such a frame exists, is $\boldsymbol{E}' = \boldsymbol{E} + \boldsymbol{V}_{HT} * \boldsymbol{B}$. In other words, the existence of HT frame implies that the magnetic field structure sampled is stationary when viewed in that frame. The detailed implementation of the dHT frame conversion is described in *Khrabrov and Sonnerup* (1998). The main purpose of MVA is to find, from single-spacecraft data, an estimator for the direction normal to a one-dimensional or approximately one-dimensional currently layer, wave front, or other transition layer in a plasma. The methodology of the MVA technique is described in *Sonnerup and Scheible* (1998).

It is shown in Figure 3.14 the hodogram pair of the principle and intermediate component (B1 vs B2, left), and principle and minimum component (B1 vs B3, right) for the data interval 10:00:00 - 12:35:00 on June 16, 2008 from the dHT and MVA analysis based on STA measurements. The magnetic hodograph is a curve in space constructed by drawing vectors from the origin, the lengths and directions of which represent the members of the measured set, and then connecting the arrowheads of those vectors by line segments, following the time sequence in which they were measured. The hodograph displayed in two projections is commonly called magnetic hodograms. It is shown that the hodogram pair on the left experiences a quasi-circular trajectory on the B1-B2 plane, and varies little on the minimum variance component (B3) from the result shown on the right. These features are signs that the magnetic field based on the measured data fits well to a flux-rope configuration, which supports the hypothesis that the flux-rope configuration embedded in CIR contributes to the LALD IMF Bs-events observed by in situ satellites. As shown in Figure 3.12, this CIR is related with a LLCH accompanied by an active region. *Gonzalez et al.* (1996) investigated the large-intensity (Bz <= -10 nT) and long-duration (T >= 3 hrs) interplanetary structure as a driver for intense geomagnetic storms near solar maximum and suggested that the solar origin of such interplanetary structures is associated with an active region (involving flares and/or filament eruptions) occurring close to

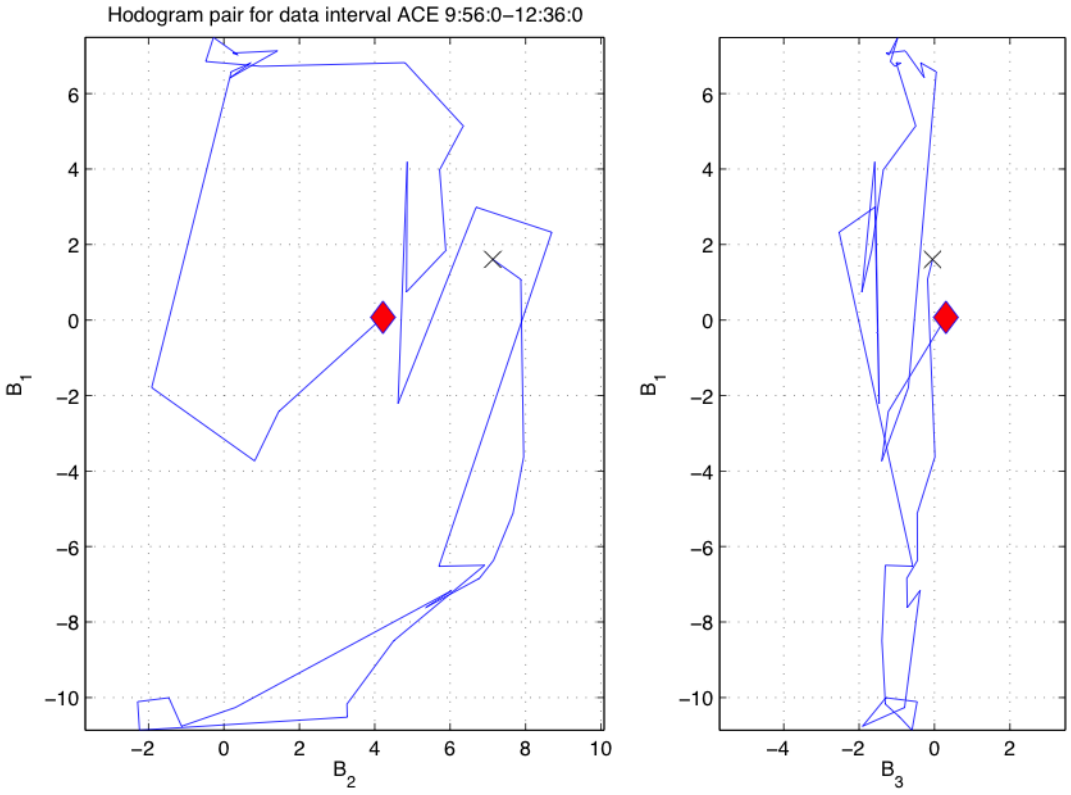

Figure 3.14: The hodogram pair of the principle and intermediate component (B1 vs B2, left), and principle and minimum component (B1 vs B3, right) after the dHT and MVA analysis for the data interval from June 16 10:00:00 to 12:35:00 based on STA plasma and magnetic field data.

the streamer belt and to growing LLCH, which they claimed as coronal hole-active region-current sheet (CHARCS). *Sakao et al.* (2007) has shown that at the edge of the AR, located adjacent to a CH, a pattern of continuous outflow was identified emanating along open magnetic field lines and into the upper corona, and they suggested that this region could be a possible source of solar wind. The reconnection between the open magnetic field lines at the edge of the LLCHs and the close field lines at the edge of the AR or bright loops is a possible source of flux-rope configuration of the magnetic field within the CIR observed by in situ satellites.

In conclusion, we have examined the relationship of the LALD IMF Bs-events

with solar wind transients and find that the major contribution to the LALD IMF Bs events is from MC, ISMFR, ejecta, SIR, and Alfvénic fluctuations. We also find that most of the LALD IMF Bs intervals unrelated with these structures show a discontinuity or slow-mode shock at both or either boundary. We also suggest that ion charge state data are good indicators of the source region of the solar wind based on the analysis of in situ measurements. Besides, we also propose a possible solar source of the emergence of IMF Bs intervals to be the low-latitude coronal hole with nearby solar activities, such as active region and bright loops. In the next chapter, we will talk about the effect of these IMF Bs-events on the Earth's magnetosphere.

CHAPTER IV

The geoeffectiveness of LALD IMF Bs-events

4.1 Introduction

The geoeffectiveness of different types of solar wind transients with different plasma and magnetic field conditions has been analyzed widely using both observational and computational evidence. *Denton et al.* (2006) performed a statistical study of the magnetospheric plasma's response to interplanetary coronal mass ejections (ICMEs) and corotating interaction regions (CIRs) during storm-time and proposed that CIR events change the plasma sheet temperature more significantly, while ICMEs modulate the density to a greater extent, which is partly attributed to the differences in their solar wind speed and density. *O'Brien et al.* (2001) did a statistical study to compare storms with and without the occurrence of relativistic electrons at geosynchronous orbit. They found that solar wind with continuous speed greater than 450 km/s, and long lasting, elevated ULF Pc5 wave power in the magnetosphere during the recovery phase of storms are both strongly associated with the appearance of these electrons. Comparing Figure 4.1 (A) and (B), which illustrates the distribution of three types of solar wind transients followed by four levels of geomagnetic activity strength, *Echer and Gonzalez* (2004) suggested that compound interplanetary magnetic structures are more geoeffective than single interplanetary magnetic structures based on a statistical study of solar wind structures like mag-

netic clouds, heliospheric current sheet sector boundary crossings and the D_{st} index following those intervals. *Newell et al.* (2007) have studied the correlation between 10 different geomagnetospheric indices and 20 candidate solar wind coupling functions using multiple years of data. As shown in Figure 4.2, they found that the function $d\phi_{MP}/dt = v^{4/3}B_T^{3/2}sin^{8/3}(\theta_c/2)$, where $d\phi_{MP}/dt$ is the rate magnetic flux is opened at the magnetopause, v is the solar wind speed, B_T is the IMF magnitude, and θ_c is the IMF clock angle, defined by $\theta_c = arctan(B_y/B_z)$, is correlated best with all the indices, except D_{st}. Note that Bz south comes into play through the IMF clock angle θ_c. Though the conclusion of *Newell et al.* (2007) is that Bz alone only accounts for a little better than a quarter of the variance, IMF Bz south is essential in all the coupling functions examined and it is well correlated with most of the magnetic activity indices (cc > 0.6) from Figure 4.2.

The relationship between interplanetary magnetic field (IMF) z component (Bz) and geomagnetic activity has also been extensively studied since the introduction of the concept of magnetic reconnection as the driver of magnetospheric dynamics (e.g., *Dungey*, 1961) and the first systematic observations of the upstream solar wind conditions. *Fairfield and Cahill* (1966) found that the southward component of IMF is associated with ground magnetic disturbances on Earth while the northward component corresponds to quiet geomagnetic conditions. *Arnoldy* (1971) showed that the solar wind/IMF parameter best correlated with auroral electrojet index (AE) is the preceding time integral of IMF southward component (Bs); thus, he suggested that IMF Bs represents a continuing dynamic mechanism for the production of substorms rather than just being a trigger. Later, *Akasofu* (1979) found that the most important parameters in the solar wind controlling the development of the main phase of geomagnetic storms and substorms are a combination of solar wind speed, magnetic field magnitude (Bt), and its polar angle.

Geomagnetic storms with minimum D_{st} less than -100 nT are found to be almost

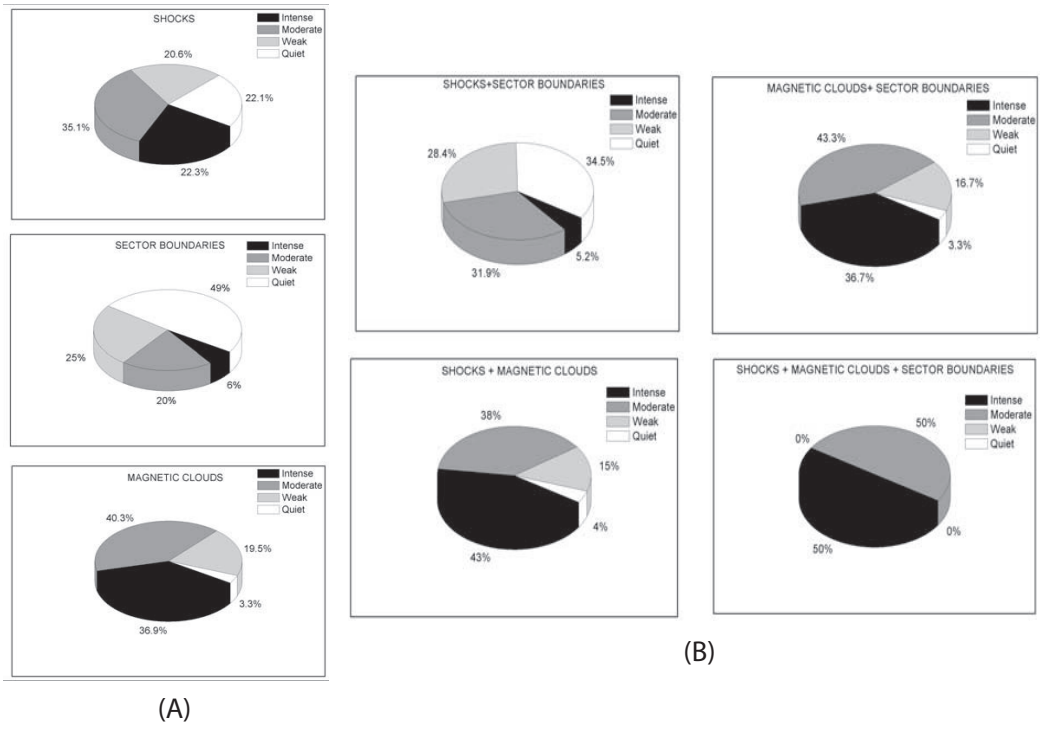

Figure 4.1: (A): Sector Graphs of the percentage of interplanetary shocks (top panel), sector boundary crossings (middle panel) and magnetic clouds (bottom panel) followed by each geomagnetic activity strength level. (B):Sector graphs of the percentage of the combined occurrence of interplanetary shocks and sector boundaries (top panel on the left), magnetic clouds and sector boundaries (top panel on the right), shocks and magnetic clouds (bottom panel on the left) and shocks, magnetic clouds and sector boundaries (bottom panel on the right) followed by each geomagnetic activity strength level. Adapted from (*Echer and Gonzalez*, 2004)

Rank, f	Λ_c	Dst	AE	AU	Goes	Kp	Auro	b2i	Φ_{PC}	AL	$\Sigma r^2/n$
1. $d\Phi_{MP}/dt$	−.845	−.796	.830	.765	−.760	.760	.741	−.720	.614	−.528	57.3%
2. E_{WAV}	−.830	−.816	.787	.734	−.751	.688	.701	−.695	.570	−.477	52.6%
3. E_{WV}	−.821	−.855	.798	.735	−.696	.700	.726	−.690	.542	−.467	52.6%
4. ε_3	−.822	−.812	.777	.718	−.737	.699	.699	−.673	.582	−.478	52.2%
5. E_{KL}	−.794	−.797	.759	.732	−.721	.709	.689	−.707	.551	−.443	51.0%
6. E_{KLV}	−.776	−.835	.772	.735	−.671	.721	.713	−.700	.528	−.433	50.8%
7. $E_{wav}^{0.5}$	−.818	−.714	.774	.741	−.731	.696	.681	−.700	.592	−.501	50.6%
8. vBs	.803	.810	−.754	−.684	.744	−.642	−.675	.648	−.560	.465	48.8%
9. $E_{KL}^{1/2}$	−.776	−.714	.732	.720	−.697	.712	.658	−.704	.561	−.453	48.2%
10. E_{SR}	−.788	−.860	.756	.706	−.586	.670	.701	.670	.476	−.410	46.9%
11. E_{TL}	−.775	−.859	.740	.675	−.581	.645	.691	−.645	.463	−.407	45.1%
12. Bs	.757	.732	−.695	−.654	.733	−.575	−.629	.620	−.549	.429	42.4%
13. ε	−.745	−.770	.670	.632	−.567	.552	.582	−.556	.365	−.338	36.6%
14. ε_2	−.707	−.735	.620	.587	−.541	.515	.554	−.532	.321	−.311	32.2%
15. E_{WAV}^2	−.698	−.654	.628	.547	−.460	.459	.537	−.462	.263	−.312	28.2%
16. B_z	.644	.476	−.610	−.556	.573	−.417	−.537	.450	−.445	.440	26.4%
17. vB_T	−.406	−.633	.385	.414	−.452	.551	.460	−.491	.344	−.132	22.6%
18. p	−.277	−.551	.312	.357	−.202	.512	.391	−.474	.217	−.085	15.3%
19. v	−.324	−.395	.374	.279	−.321	.582	.399	−.315	.254	−.251	14.7%
20. n	−.041	.102	.001	.093	.033	.058	.122	−.172	.058	.070	0.8%

[a]The coupling functions are ranked from best ($d\Phi_{MP}/dt$) to worst (n) by the total variance of the 10 indices (13 data sets, counting multiple solar cycles for Λ_c, Dst, and Kp) predicted, as given in the right-hand column.

Figure 4.2: Table 3 adapted from (*Newell et al.*, 2007): Correlations Between 20 Coupling Functions and 10 Indices.

always caused by strong negative Bz with durations longer than 3 hours (*Gonzalez et al.*, 1994). Many studies have also shown that the magnitude of geomagnetic storms increases with either more intense or longer southward IMF (e.g., *Hirshberg and Colburn*, 1969; *Arnoldy*, 1971). Geomagnetic substorms were initially considered to be a simultaneous phenomenon with storms but weaker in effect, and *Akasofu* (1968) showed that a chain of substorms could induce storm-time ring current. However, *Tsurutani and Gonzalez* (1987) confirmed that ongoing substorm activity does not necessarily lead to storms, and more recent studies demonstrated that substorms can be triggered by internal sources (*Horwitz*, 1985; *Henderson et al.*, 1996) or external driving factors such as certain configurations of IMF (e.g., *Heppner*, 1955; *Lyons*, 1995; *Zhou and Tsurutani*, 2001). *Burch* (1972), *Samson and Yeung* (1986), and *Lyons* (1996) have found that the northward turning of the IMF can trigger substorm onset. Since it is highly correlated with solar wind/IMF conditions, the current prediction of geomagnetic activity, especially large-scale storms, is based on the forecast of occurrence of geoeffective solar activity and the ensuing solar wind and IMF conditions. The maximum magnitude of IMF Bs observed in situ at 1 AU was found to be directly related with the propagation velocity of CMEs observed in coronagraph observations (*Lindsay et al.*, 1999). This velocity is needed for forecasting the arrival time of ICME to the Earth (*Hochedez et al.*, 2005). Further, though the occurrence frequency and time delay of CH outflows or CIR are easily estimated, the determination of the Sun-Earth magnetic connectivity is unfortunately not straightforward (*Schwadron and McComas*, 2004) and requires the knowledge of the instantaneous Parker spiral geometry and a comprehensive understanding of IMF Bz evolution. Despite the progress in space weather modeling, predicting IMF Bs at 1 AU is still poorly done (*Hochedez et al.*, 2005).

The response of magnetospheric ultra-low-frequency (ULF) waves to non-storm-exclusive intervals has also been studied extensively. *Takahashi and Ukhorskiy* (2008)

performed correlation analysis between the solar wind parameters and amplitude of Pc5 waves (1.7 - 6.7 mHz) at geosynchronous orbit for solar minimum year 2006 and concluded that the major driver of geosynchronous Pc5 waves is solar wind pressure variations rather than the Kelvin-Helmholtz instability on the magnetopause. The statistical studies by *Sanny et al.* (2002, 2007) suggested that solar wind dynamic pressure and its variability have greater influence on ULF wave power than IMF northward/southward orientation, and that ULF wave power changes more for northward IMF than for southward IMF during periods of high solar wind dynamic pressure. However, *Skoug et al.* (2004) pointed out that the solar wind dynamic pressure coupled with large negative Bz was sufficient to cause intense geomagnetic disturbances.

Global simulations have also been used extensively to understand the solar wind drivers of geomagnetic activity. *Lopez et al.* (2004) demonstrated that solar wind density plays a significant role in modulating the transfer of energy to the magnetosphere under southward IMF using global magnetohydrodynamic (MHD) simulations of the solar wind-magnetosphere interaction. *Palmroth et al.* (2003) used a 3-D global MHD simulation code to examine the energy flow from the solar wind to the magnetosphere during a magnetic storm and found that the correlation between the simulated total transferred energy and the empirical energy parameter calculated from the solar wind parameters (magnetic field, solar wind speed, and magnetic field clock angle) depends on the phase during the storm. *Tóth et al.* (2007) carried out the first sun-to-thermosphere simulation of the most powerful solar eruptions associated with the "Halloween Storms", using observed solar magnetograms, and pointed out that the simulated magnetospheric activity index is in good agreement with the D_{st} index. *Owens et al.* (2014) used downscaling input and tested an ensemble of simulation results for the space weather forecasting model- the Lyon-Fedder-Mobbary (LFM) simulation, and found that the best estimate of magnetospheric forecast is improved

and uncertainty is quantifiable. They also suggested that the distribution of solar wind parameter fluctuations should be analyzed for different solar wind types respectively, and that the coupling of different components should be considered.

Following in this chapter, we will discuss the Earth's magnetospheric response to the large-amplitude, long-duration IMF Bs-events, and the effect of their association with different kinds of solar wind transient structures.

4.2 The geoeffective of IMF Bs-events: a general aspect

The symmetric (SYM) -H is the index to describe the geomagnetic disturbance fields in the horizontal direction in mid-latitudes with high-time resolution (1-min). The Auroral Electrojet (AE) index is derived from geomagnetic variations in the horizontal component observed at selected observatories along the auroral zone in the northern hemisphere to represent the overall activity of the electrojets. SYM-H and AE indices are widely used to get a comprehensive understanding of the activity in the magnetosphere, especially the well-known geomagnetic storm and substorm.

In order to investigate the statistical relationship between the occurrence of IMF Bs-events and geomagnetic activity, we compared the count of IMF Bs intervals with different threshold and the number of storms (e.g., *Rathore et al.*, 2012) for the period between 1996 - 2007 as shown in Figure 4.3. Comparing all the three categories, all the storms (D_{st} <= -50 nT) have the highest correlation with the occurrence and intensity of the IMF Bs-events. The yearly frequency of intense storms (D_{st} <= -100 nT) changes in a similar way as the IMF Bs-events but with one year lag. While the moderate storms (-100 nT <= D_{st} <= -50 nT) show four significant peaks over the solar cycle with worse correlation with the IMF Bs-events. From a statistical perspective, the large-scale geomagnetic disturbances are well correlated with the southward component of the IMF.

Figure 4.4 shows the histograms of minimum SYM-H in terms of minimum Bz,

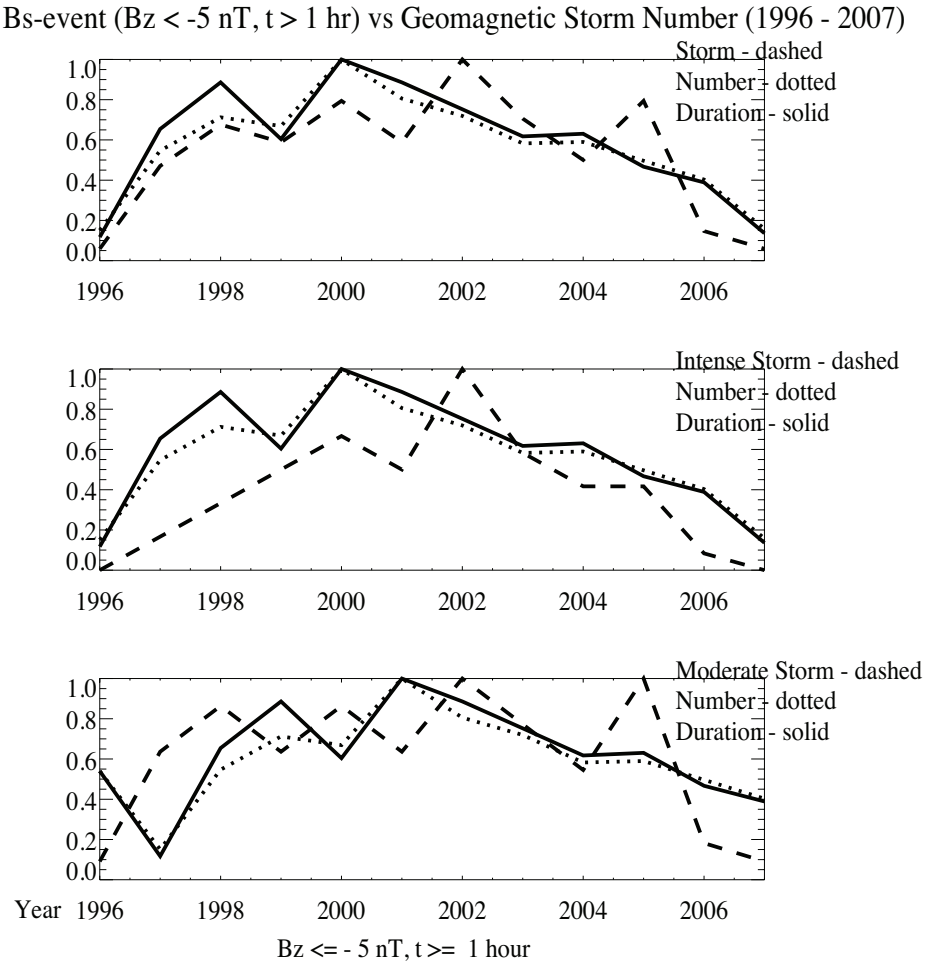

Figure 4.3: The yearly distribution (divided by the range of the value for each parameter) of the number and total duration of IMF Bs-events from 1996 - 2007, compared with the occurrence count of storms in total (top), intense storms (D_{st} <= -100 nT, middle), and moderate storm (-100 nT <= D_{st} <= -50 nT, bottom). The period of the events lasts at least 1 hour and the upper threshold of the Bz value is -5 nT.

duration of the events, integrated Bz, and average Vx*Bs (solar wind eastward electric field) for all the IMF Bs-events (Bz < -5 nT, t > 1 hour) in the period 1995 - 2010. The dark blue, light blue, yellow, and red bars represent the events in the four quartiles (0-25%, 25%-50%, 50%-75%, 75%-100%) of the absolute values of minimum SYM-H, respectively. It is shown that the events in the largest quartile (75% - 100%) of the minimum SYM-H value do not correspond to the largest quartile of the duration of the intervals significantly. The Spearman correlation coefficient between the distribution of minimum SYM-H and the duration is -0.32, minimum Bz 0.50, integrated Bz 0.46, eastward electric field -0.60, respectively. The coupling effect of solar wind velocity and IMF Bs plays the most important role in triggering geomagnetic storms.

Figure 4.5 shows the histograms of maximum AE (nT) in the same format as in Figure 4.4. It is presented that the distributions are similar as that for the minimum SYM-H, but more scattered. The Spearman correlation coefficient between the maximum AE value and the duration is 0.26, minimum Bz -0.44, integrated Bz -0.39, and eastward electric field 0.58. It is indicated that the southward component of IMF and solar wind electric field are more important as a trigger for geomagnetic storms than for substorms.

4.3 Earth's magnetospheric response to IMF Bs-event related with different types of solar wind transients

4.3.1 Case study: Geoeffectiveness of IMF Bs-events associated with different solar wind transients

As many studies have demonstrated that the other plasma/IMF parameters in the upstream solar wind also affect the Earth's magnetic field variations besides the southward component of IMF, we did a further study of the geoeffectiveness of the IMF Bs-events in terms of their association with different solar wind transient struc-

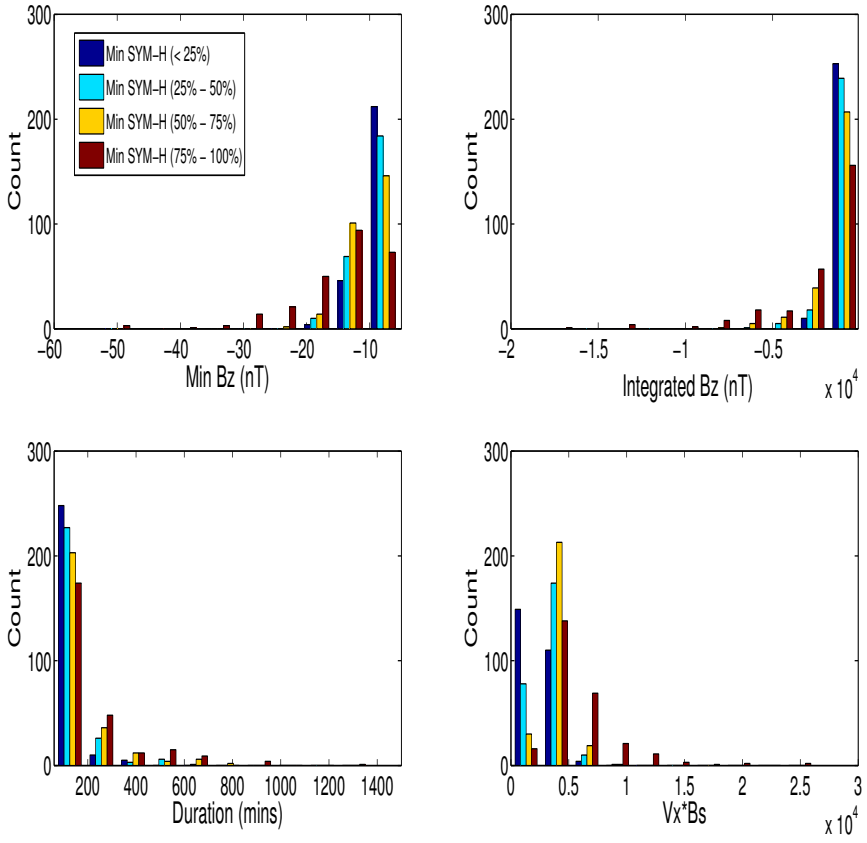

Figure 4.4: Histograms of minimum SYM-H (nT) in the 12 hours following all the IMF Bs-events (Bz < -5 nT, t > 1 hour) in terms of minimum Bz (top left), duration of the event (bottom left), integrated Bs (top right), average Vx*Bs (bottom right). The dark blue, light blue, yellow, and red bars represent the events in the four quartiles (0-25%, 25%-50%, 50%-75%, 75%-100%) of the absolute values of minimum SYM-H, respectively.

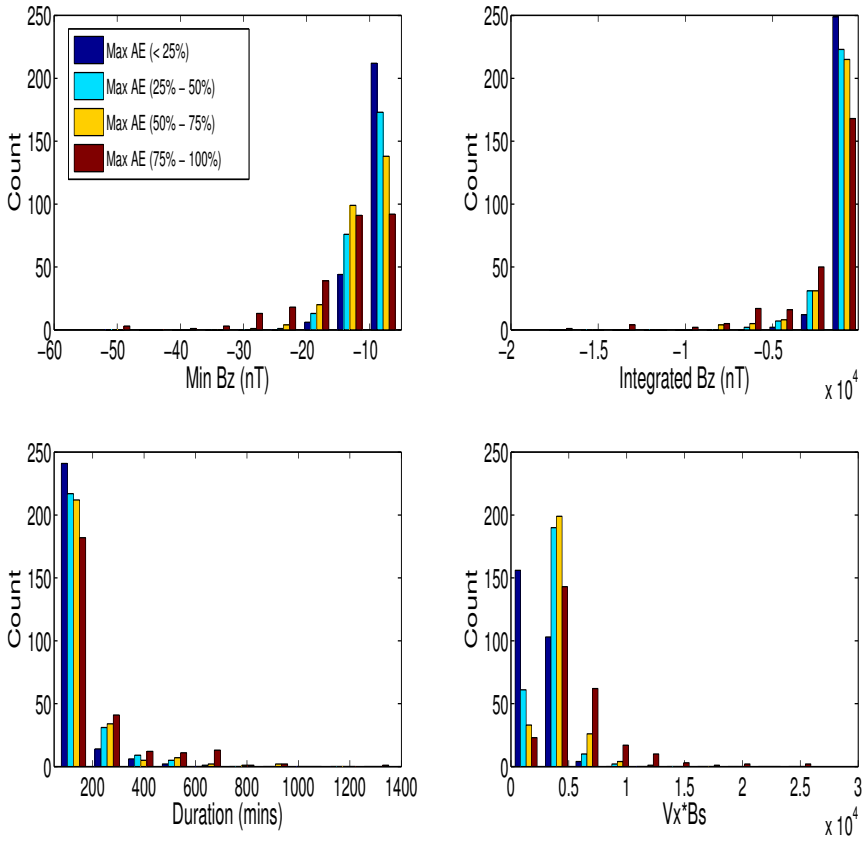

Figure 4.5: Histograms of maximum AE (nT) in the 12 hours following all the IMF Bs-events (Bz < -5 nT, t > 1 hour) in the same format as Figure 4.4.

tures.

Figure 4.6 shows the magnetic field and plasma measurements at 1 AU obtained from OMNI website (time shifted to the bow shock), and the geomagnetic activity indices for an IMF Bs-event associated with a MC on July 17-18 2005. The IMF Bs interval is marked by the two vertical lines. The whole MC structure started at $\sim$ 14:30 July 17 and ended at $\sim$ 11:00 July 18, while the embedded LALD southward IMF interval occupied about the posterior two third of it. The peak-to-valley value is about 12 nT for the magnetic field amplitude, and the z-component of IMF experiences the bipolar change with minimum Bz of -12 nT while the other two components alomst hold the same direction. The MC is in the expansion part of an ICME with a decreasing profile of the solar wind speed (Figure 4.6 (C)). The mean speed in the period between the dashed lines is about 415 km/s. Meanwhile, the plasma density shows a great increase by up to 5 times, and the dynamic pressure changes in the similar way as density. From Figure 4.6 (D), the AE index abruptly increases by 1200 nT about 2 hours after the start time of the IMF Bs-event denoted by the first vertical line. However, the SYM-H (panel (E)) shows sudden increases simultaneously with the increases in the dynamic pressure, and then rapid decrease to -80 nT - indicating a moderate geomagnetic storm.

Figure 4.7 illustrates the measurements of Earth's upstream solar wind conditions and corresponding geomagnetic indices for an ejecta-associated IMF Bs-event on March 28, 2001 in the same format as in Figure 4.6. The IMF Bs-event between the two vertical lines is from 11:40 - 13:30 with minimum value $\sim$ -13 nT. The magnetic field strength in panel (A) shows fluctuations in the interval of the IMF Bs-event while smooth decrease during the whole period. The solar wind for the whole 8 hours shows high-speed stream feature with a minimum value of 560 km/s that decreases by $\sim$ 60 km/s. The proton density and dynamic pressure also decrease by more than 3 times during the IMF Bs-event with some fluctuations. AE index in panel (E) shows

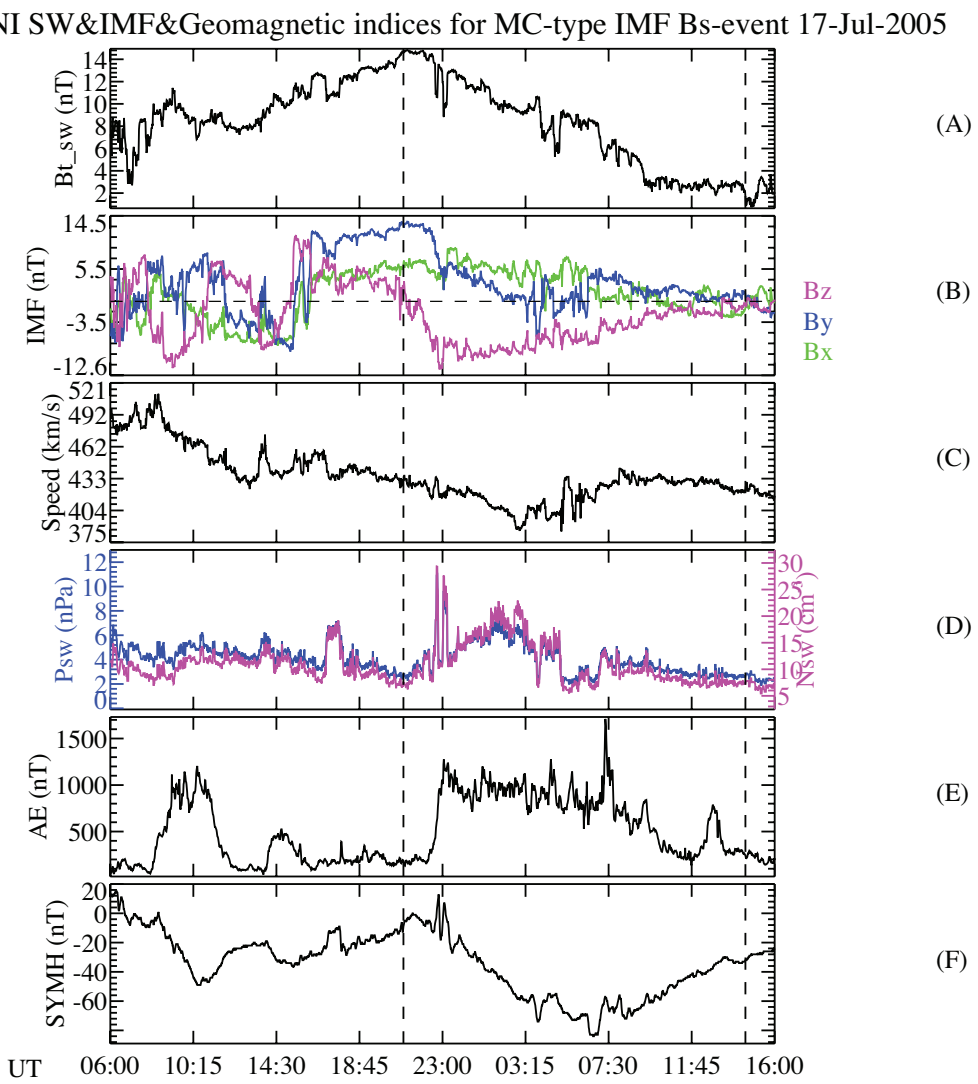

Figure 4.6: Measurements of magnetic field strength and components, solar wind bulk speed, dynamic pressure and density, geomagnetic AE index, and SYM-H index (A - F) based on near-Earth satellites and ground-based magnetometers for the MC-related IMF Bs-event in the period of 06:00:00 July 17 - 16:00:00 July 18, 2005. The IMF Bs interval is marked by the vertical dashed lines.

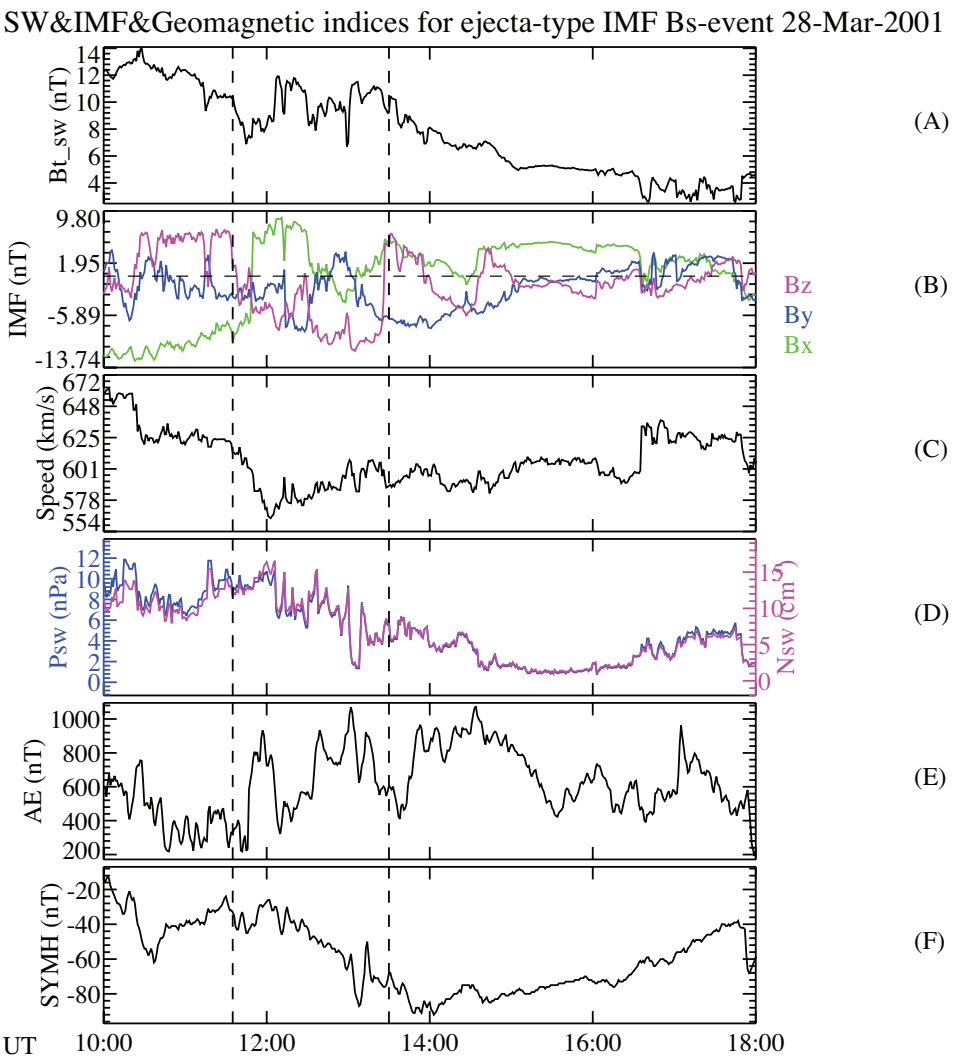

Figure 4.7: Measurements of solar wind plasma, IMF and geomagnetic indices for the IMF Bs-event related with a non-MC-ICME (ejecta) in the period of 10:00:00 - 18:00:00 March 28, 2001 in the same format as in Figure 4.1.

two sudden increases between the vertical lines from 200 nT to 900 nT, and 500 nT to 1000 nT, respectively, corresponding to the changes of the Bz component. However, the SYM-H index presents almost continuous decrease from -30 nT to -80 nT during the IMF Bs-event.

Figure 4.8 illustrates the same parameters for an IMF Bs-event related with a CIR (recurring SIR) in the period 00:00:00 - 20:00:00 on July 12, 2008 in the same format as in Figure 4.1. The vertical lines indicate that the IMF Bs-event starts

from 04:40 and ends around 08:00 with minimum Bz as -13 nT. Panel (C) indicates that the IMF Bs-event is embedded in the interaction region of the CIR with solar wind speed about 500 km/s prior to a large increase. The magnetic field is increasing during almost the whole IMF Bs-event from 9 nT to 14 nT, while the polarity of all the three components of the magnetic field stay unchanged. It is shown in panel (D) that the plasma density and dynamic pressure decreases slightly between the vertical lines. The AE index in panel (E) shows a jump about 2 hours before the IMF Bs-event, while it shows several fluctuations during the IMF Bs-event. The SYM-H index in panel (F) presents a decrease starting at the same time as the AE increase but shows continuous and smooth decrease from -20 nT to - 40 nT in the period of IMF Bs-event. The abrupt change of the two indices corresponds to a magnetic decrease in the solar wind.

Figure 4.9 shows the SW/IMF measurements and corresponding geomagnetic activity indices for an Alfvénic fluctuation related IMF Bs-event during 19:00:00 Nov 19, 2002 - 05:00:00 Nov 20, 2002. The IMF Bs interval is from 21:30 to 00:20 marked by the two vertical lines, showing a minimum value around -12 nT. It is shown from panels (A) and (C) that the magnetic field and solar wind speed amplitude does not change significantly but varies frequently in a similar way. The solar wind speed is varying around 400 km/s, indicating that the interval is not overlapping with a HSS. Meanwhile the solar wind dynamic pressure and density decreases overall for the period between the two lines but with fluctuations. The AE index in panel (E) experiences two significant increases during the IMF Bs-event from $\sim$ 0 nT to 650 nT, while the SYM-H starts to decrease continuously about half an hour after the start time of the IMF Bs-event from -10 nT to -40 nT.

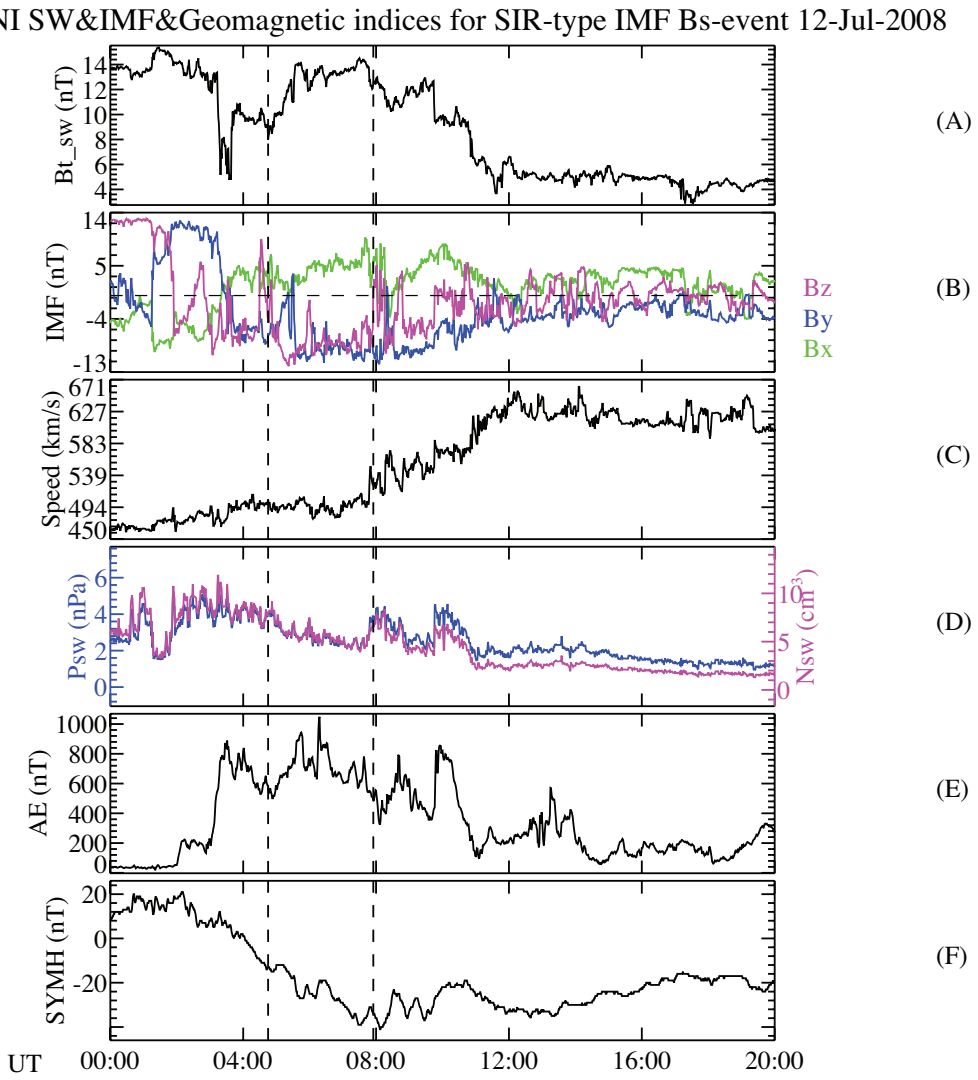

Figure 4.8: Measurements of solar wind plasma, IMF and geomagnetic indices for the IMF Bs-event related with a SIR in the period of 00:00:00 - 20:00:00 July 12, 2008 in the same format as in Figure 4.1.

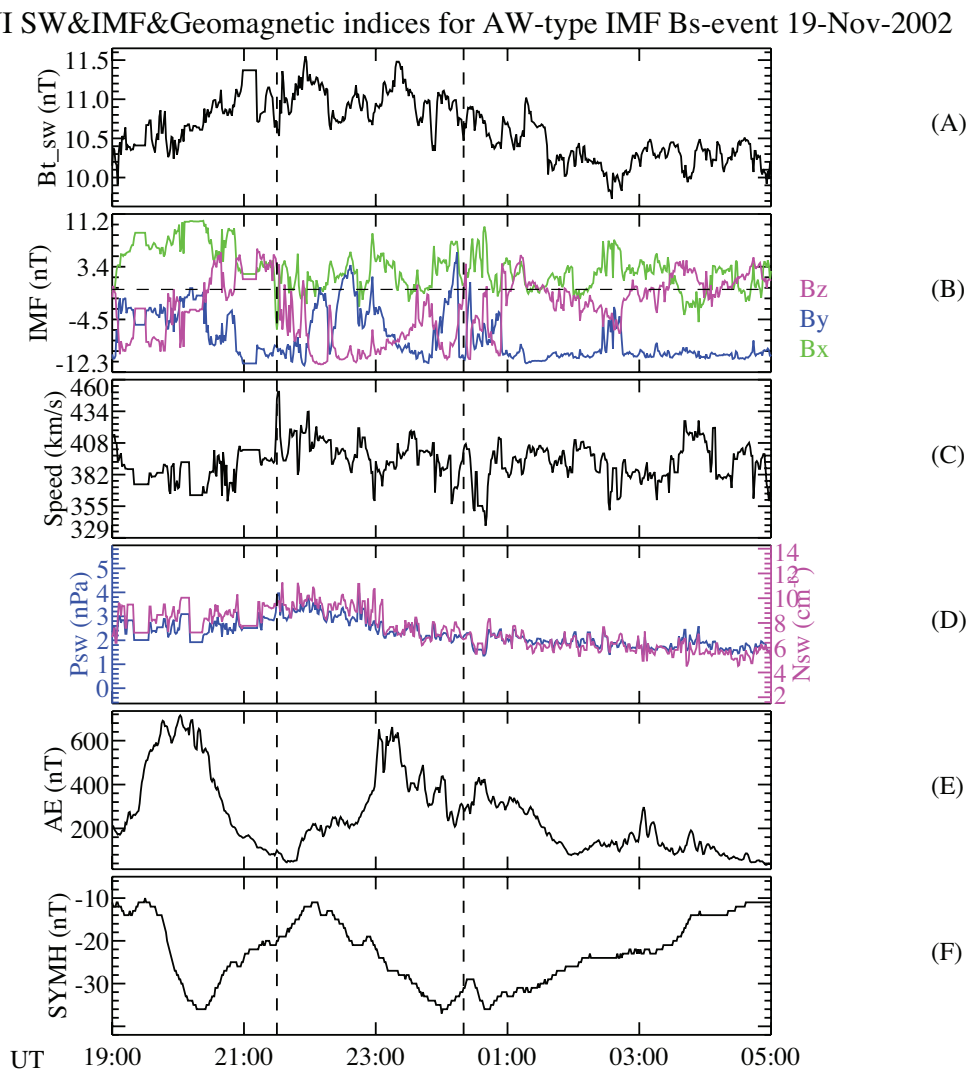

Figure 4.9: Measurements of solar wind plasma, IMF and geomagnetic indices for the Alfvénic fluctuation associated IMF Bs-event in the period of 19:00:00 November 19 - 05:00:00 November 20, 2002 in the same format as in Figure 4.1.

4.3.2 Statistical study: Geoeffectiveness of IMF Bs-events associated with different solar wind transients

In order to study the statistical effect of IMF Bs-events on the Earth's magnetospheric activities, we also analyzed the relationship between a set of geomagnetic activity indices and IMF Bs-events associated with different kinds of solar wind transient structures.

Figure 4.10 shows scatterplots of minimum SYM-H (nT) in terms of minimum Bz and duration for Bs events in different categories: (a) MC, (b) ejecta, (c) SIR, and (d) other. The threshold of the duration and Bs magnitude are 1 h and -10 nT. The color bar represent the minimum SYM-H values in the corresponding intervals (with the solar wind time shifted). The duration of MC-type Bs events (shown in Figure 4.10a) has the largest range from 1 h up to about 13 h, but the minimum Bz values are mostly distributed between -10 nT and -30 nT. The minimum SYM-H during the strongest magnetic storm is less than -450 nT while the duration and maximum magnitude of Bs is around 8.5 h and 50 nT, respectively. Over 70%/50% of the MC Bs events triggered a moderate/strong storm (SYM-H $<$ -50/-100 nT). From Figure 4.10b, the minimum Bz of ejecta-type Bs events extends to -76 nT, and the duration ranges up to 7 h. The greatest storm identified by the minimum SYM-H (-435 nT) is triggered by an ejecta with duration of 2.3 h and minimum Bz of -48.5 nT. Figure 4.10c shows that 86% of the SIR-type Bs events are distributed in the region -30 nT $<$ min(Bz) $<$ -10 nT, 1 h $<$ duration $<$ 4 h, while the most intense storm (SYM-H $<$ -200 nT) was related to a Bs event with most negative Bs intensity as -32 nT for about 6.5 h. For the Bs events that are not related with well-defined solar wind structures shown in Figure 4.10d, the most intense storm with a minimum SYM-H less than -200 nT was triggered by an event with minimum Bz around -30 nT and duration of 6.5 h. In the group unrelated with well-defined solar wind structure, intense magnetic storms occurred if either the duration of the Bs event was prolonged or the minimum

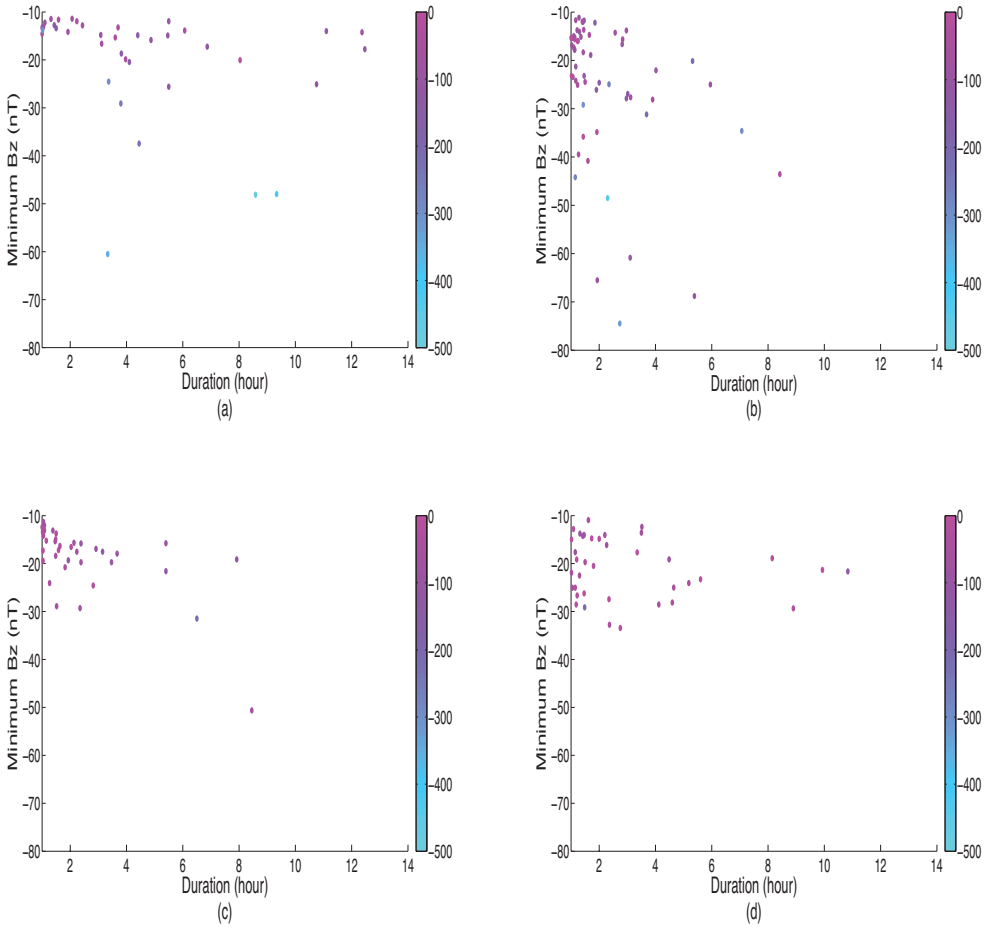

Figure 4.10: Scatterplots of minimum SYM-H (nT) in terms of minimum Bz and duration for Bs events in different categories: (a) MC, (b) ejecta, (c) SIR, and (d) other. The threshold of the duration and Bs magnitude are 1 h and 10 nT. The color codes show the minimum SYM-H values in the corresponding intervals.

Bz was more negative.

Figure 4.11 shows the minimum SYM-H (nT) and maximum AE (nT) from top to bottom for all the Alfvénic fluctuation related Bs-events (1998 April - 2004). The intervals of ground measurements start at the same universal time as the Alfvénic events but end 75 mins later than the Bs-events observed by ACE. The top panel shows that about one third of these events are followed by an interval of SYM-H less than -50 nT, indicating a geomagnetic storm. Around half of the events induce substorms, indicated by maximum AE greater than 1000 nT.

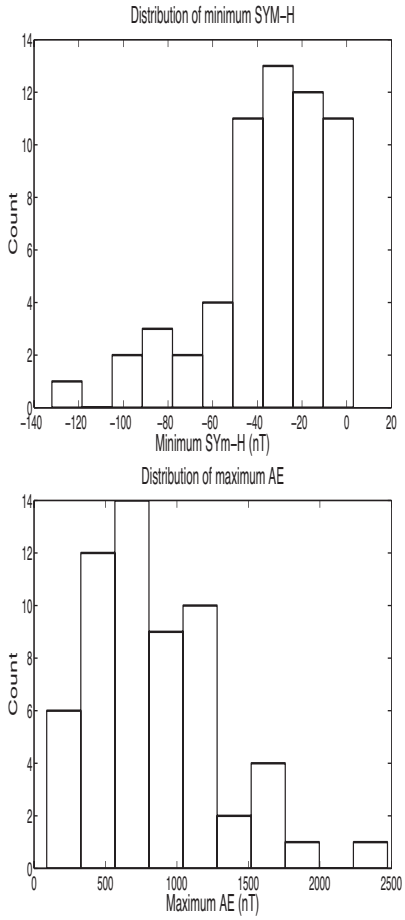

Figure 4.11: Histogram of minimum SYM-H (nT) and maximum AE (nT) from top to bottom for all the Alfvénic fluctuation related Bs-events (1998 April - 2004). The threshold of the duration and Bs magnitude of the Bs-events are 1 hour and -5 nT. The intervals of ground measurements start at the same universal time as but end 75 mins later than the Bs-events observed by ACE.

Figure 4.12, 4.13, 4.14 show the superposed epoch analysis for all the Bs-events (Bz < -5 nT, t > 1 hour) related with ICMEs and SIRs in the period of 1995 - 2004, and related with Alfvénic intervals during 1998 -2004 (*Zhang and Moldwin*, 2014) and (*Zhang et al.*, 2014). There are 227 events defined as ICME-type southward IMF-events, 198 cases categorized as SIR-type, and 56 events identified as Alfvénic Bs-events. We do not show or discuss results for shock related events since there are only a few events (11). Panel (A) in all the three figures present a decrease to or below -5 nT in IMF Bz at zero epoch time, while the median duration of strong Bs intervals for ICME-, SIR-, and Alfvénic type Bs-events last for about 4 hrs, 3 hrs, and 2 hrs, respectively until they cross the horizontal dashed line again. Panel (B) shows the magnetic field amplitude (Bt). There is a weak jump of all the three quartiles of Bt at the zero epoch time for all the different classes of structures. The profile of median Bt shows a gradual increase from 7.31 nT to 11.67 nT before the zero epoch time and then a decrease to 8.31 nT until the end of the 2-day profile for ICME-type Bs-events. The median value of total magnetic field increases by 100% from 5.59 nT during the first 24-hour of the profile and decreases to 7.4 nT for SIR-related Bs-events. Panel (C) shows that the average change of solar wind speed is insignificant for ICME-type and Alfvénic Bs-events but there are higher values for ICME events. For SIR-type Bs-events, there is a smooth increase from 350 km/s to about 470 km/s for the median values in Vsw throughout the 2 days. The proton density in panel (D) indicates an increase after the zero epoch followed by a decrease for all Bs-events except for the Alfvénic ones. The increase of Np starts about 4 hrs / 8 hrs before and ends at the zero epoch for ICME-/SIR- related Bs-intervals. Some cases, especially from the ICME Bs-event list, show large deviations from the main band of the statistical distribution at some epoch time points. This could be caused by the different timescales of these events, and/or different amplitudes of the variations during these intervals, and/or different background solar wind/IMF conditions. However, the trend of the change

of these parameters can be distinguished, which is the crucial result for studying the potential precursors of these strong southward IMF intervals.

4.4 Discussion and Conclusion

In order to comprehensively study the geoeffectiveness of the Bs events, we also investigated the maximum AE in terms of Bs duration and magnitude. The results are that the strongest storm and substorm are not associated with the same event except the ejecta-type Bs events. This may be due to the large expansion of the auroral oval to low latitudes and hence away from the higher-latitude AE stations. For large storms, we also note that great Bs events (t > 3 h, Bz < -10 nT) do not always induce large storms. This might be explained by *Kane* (2010a,b) who showed that the multivariate analysis of Bz and D_{st}, with AU, AL, and auroral particle precipitation index POES as additional indices, has higher correlation than Bz and only D_{st}, suggesting that the solar wind input energy is distributed to various channels of the Earth's magnetosphere in addition to the ring current. Another possible mechanism to support the observational result is that the preconditioning of the plasma sheet plays an important role in the response of the inner magnetosphere to solar wind forcing (*Kozyra et al.*, 2002; *Sergeev et al.*, 2014), and also that the frequency of the polarity change of IMF Bz significantly alters the state of the inner magnetosphere via buildup of different time scales of the process (*Liemohn et al.*, 2001). The distribution of solar wind energy into the Earth's magnetosphere will be examined by data-model comparison for the unusual Bs events in future work.

The result showing that MC, ejecta, and SIR drive storms in different ways is consistent with *Borovsky and Denton* (2006) who showed that CME-driven storms are brief with strong D_{st} while SIR-driven storms are of longer duration. In order to examine the other potential parameters in the solar wind that differentiate the geoeffects of MC, ejecta, and SIR, we obtained the average solar wind speed during

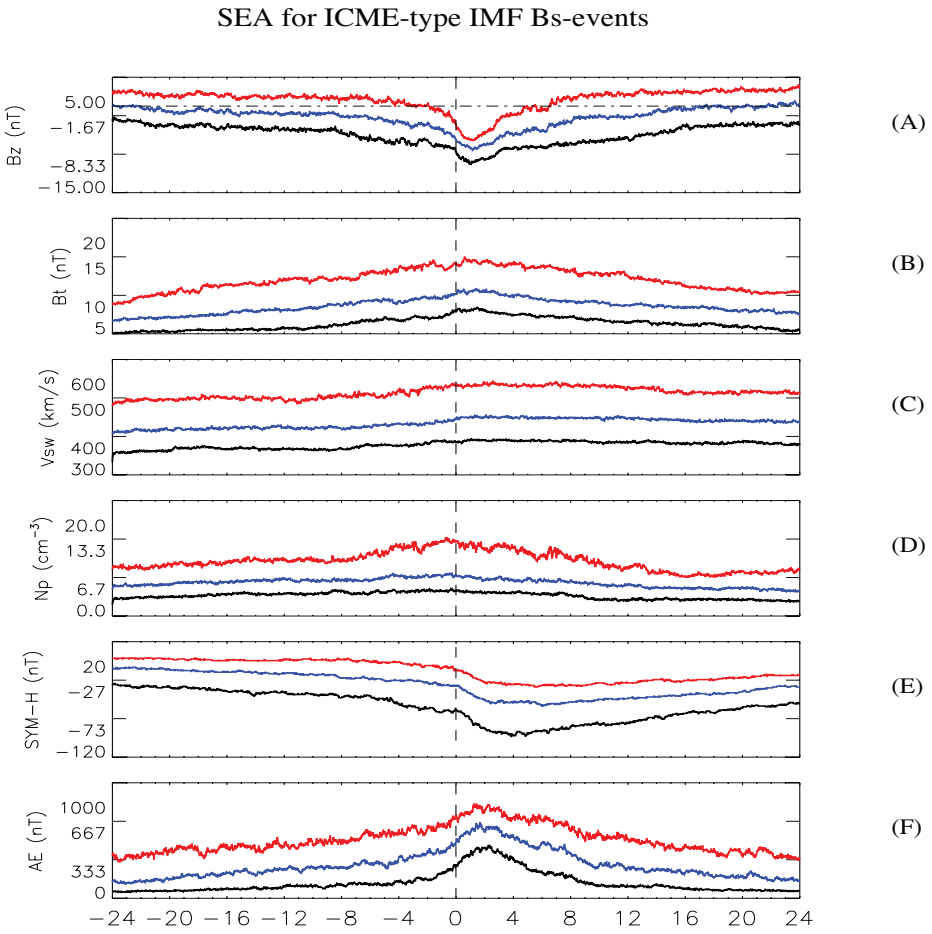

Figure 4.12: The superposed epoch analysis (SEA) of the IMF/SW parameters and geomagnetic activity indices (SYM-H and AE) from (A) through (F) for the IMF Bs-events (Bz < -5 nT, t > 1 hr) related with ICME. The epoch zero is set at the change of IMF Bz drops under -5 nT/-1 nT denoted by the dashed vertical line, and the duration is 48 hours. The red/blue/black are the temporal files of upper/middle/lower quartile of IMF Bz, IMF amplitude, solar wind speed, proton density from top to bottom panels. The horizontal dashed line marks the threshold as Bz = -5 nT.

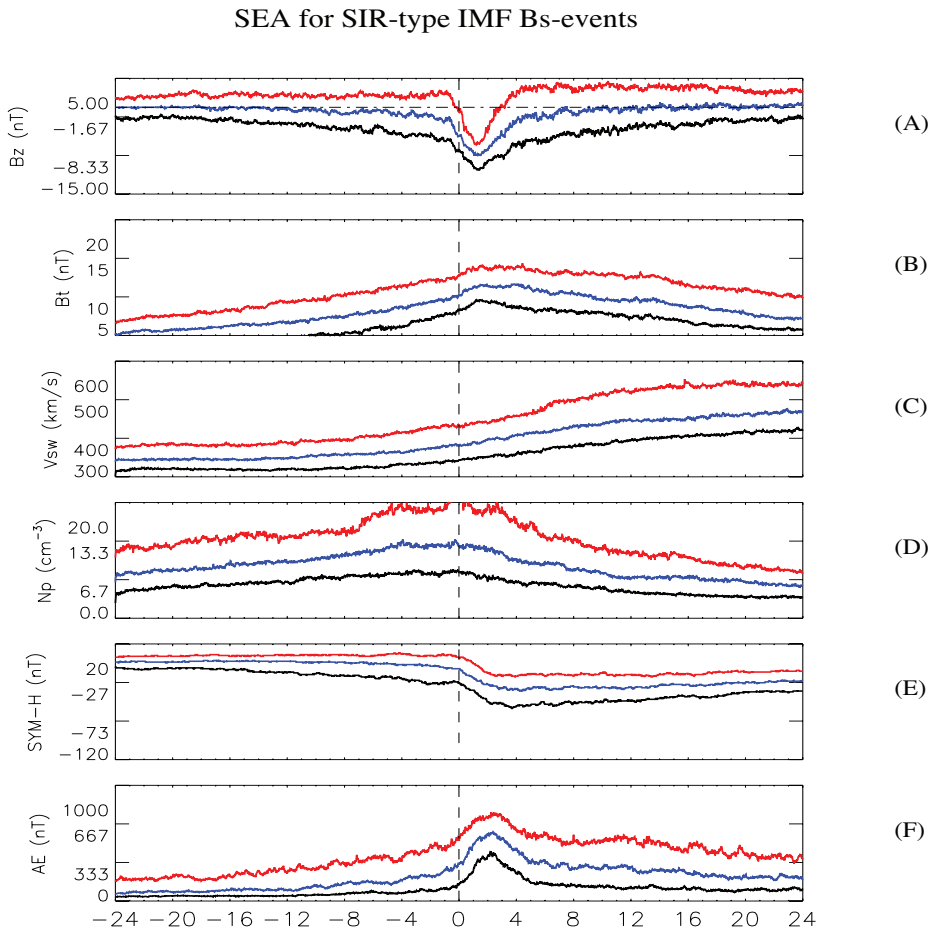

Figure 4.13: The same format as Figure 4.12 for all the 198 SIR- related Bs-intervals.

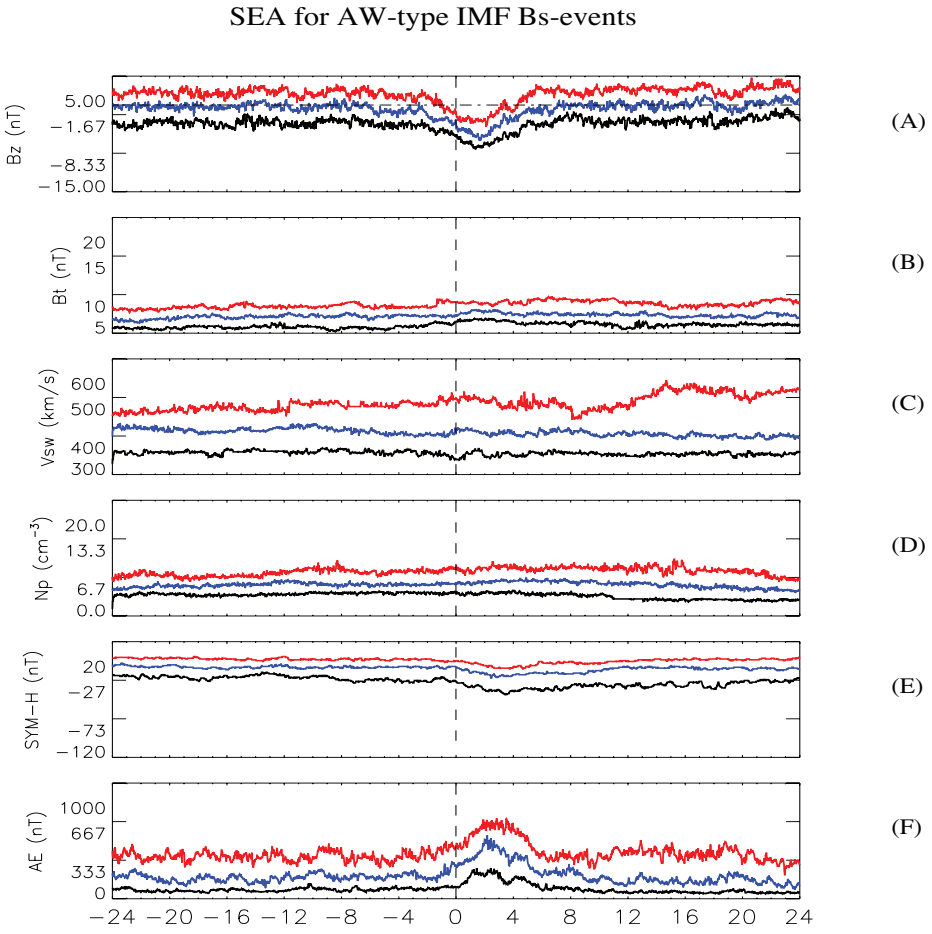

Figure 4.14: The same format as Figure 4.12 for all the 56 Alfvénic Bs-intervals in the period of 1998 - 2004.

the Bs events and found that MC Bs events have the largest mean flow speed (512 ± 195 km/s), ejecta Bs events average 436 ± 183 km/s, and 379 ± 89 km/s for SIR. It implies that the co-occurrence of high-speed solar wind in different types of Bs events account for the different behaviors of the Earth's magnetosphere.

We analyzed the storm activity index - SYM-H, and found that about 1/3 of the Alfvénic fluctuation related IMF Bs-events triggered storms (SYM-H < -50 nT). However, compared to Bs-events in other categories, Bs-events associated with Alfvénic fluctuations are a weaker source for triggering geomagnetic storms. During the Bs-events (t > 1 hour, Bz < -5 nT) from April 1998 to end of 2004 in our study, 123 storms occurred, 40% due to ICMEs, 44% due to SIRs, 5% by shocks, 1% by SMFR, and 10% due to Alfvénic solar wind. The differences of the contribution to triggering magnetic storms among different solar wind structure related Bs-events are their occurrence frequency and average solar wind speed (*Zhang and Moldwin*, 2014). While Alfvénic Bs-events are relatively weak in triggering geomagnetic storms, we have analyzed the ULF wave activity at the geosynchronous orbit (GEO) based on the magnetometer data from GOES satellites in response to the IMF Bs-event related with Alfvénic fluctuations shown in Figure 4.9. The magnetic fields are projected to the Mean Field-Aligned (MFA) coordinate system (*Takahashi et al.*, 1990), in which the parallel direction p is determined by 20-min sliding averaged magnetic field, the azimuthal direction a is parallel to the cross product of the p and the spacecraft position vector, and the radial direction r- completes the triad. For the case study, the magnetic field data are then filtered with the 150s-600s band-pass filter. Figure 4.15 shows the magnetic field measurements in Cartesian coordinates and the MFA coordinate filtered by the ULF Pc5 wave band for the IMF Bs-event associated with Alfvénic fluctuations. The period of the IMF Bs-event is 21:30 Nov 19 to 00:20 Nov 20. The local time marked at the bottom is calculated by using $LT = UT + Long/15$ based on the position of the satellites (left: GOES 8, right: GOES 10). During the

IMF Bs-event, the GOES 8 satellite was located at the dusk side (1600-2000LT) while GOES 10 at the afternoon side (1200 - 1600 LT). Figure 4.15 (left) shows during this event, Bx is changing from negative to positive, while the polarity of By and Bz stay unchanged. Though the total magnetic field does not change significantly between 21:00 - 02:00, the z- component of the magnetic field decreases from $\sim$ 90 nT to $\sim$10 nT. Strong ULF Pc5 waves have been triggered at 23:00UT, with largest amplitude of 24 nT (peak-valley-value) in the azimuthal component. However, the magnetic field measured by GOES 10 shown on the right does not present significant ULF Pc5 wave signature. It is indicated that the Alfvénic fluctuation related IMF Bs-events is a possible driver for large-scale ULF wave oscillations in the Earth's magnetosphere.

In conclusion, we have shown the relationship between the IMF Bs-events and the geomagnetic activity indices (SYM-H, AE, ULF wave), as well as the differences among the different types of related solar wind transients. We proposed that the southward component of IMF is more important in triggering geomagnetic storms than substorms. We also demonstrated that the plasma conditions embedded in different solar wind transients also affect the geomagnetic activity level during the IMF Bs-events. In the next chapter, we will discuss the possible improvements of the space weather forecasting system based on our studies.

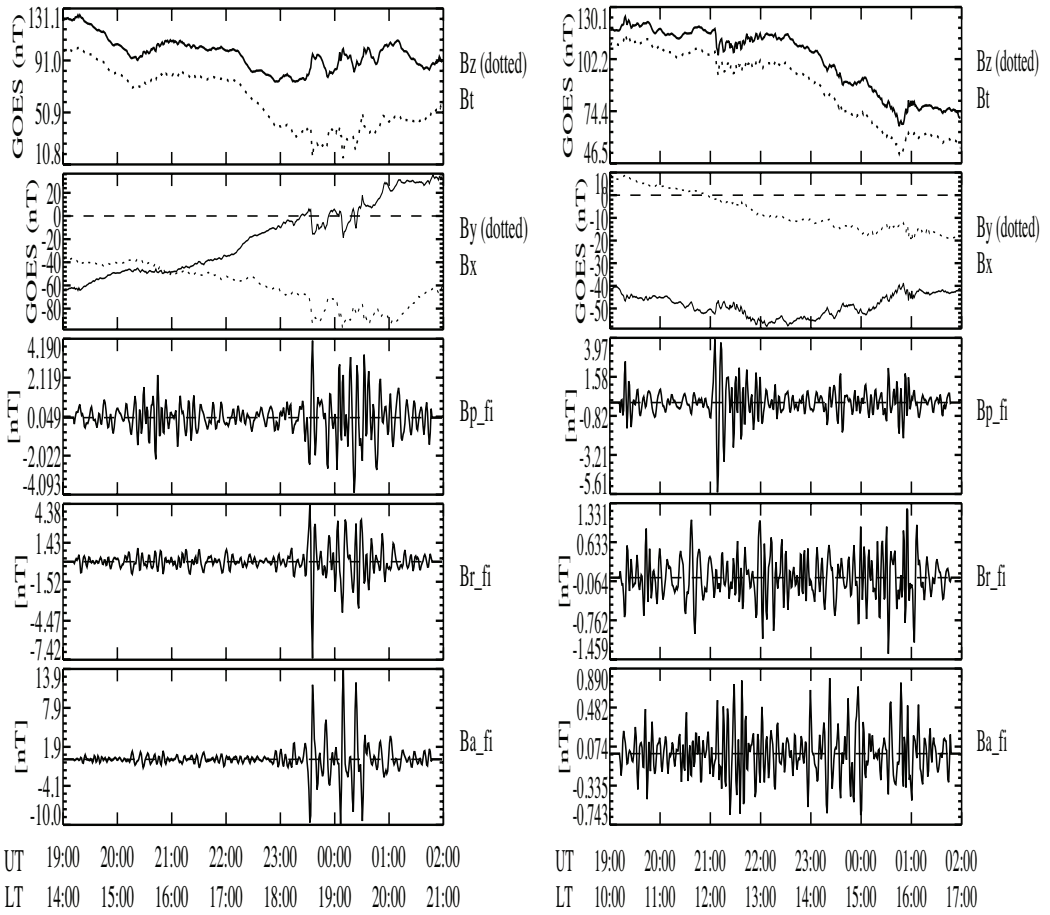

Figure 4.15: The measurements from GOES 8 (left) and GOES 10 (right) on Nov 19-20 2002. The magnetic field measured by GOES satellites is projected to the mean field-aligned (MFA) coordinate system. From top to bottom: the magnetic field amplitude (solid line) and Bz (dotted line), Bx (solid line) and By (dotted line), parallel, radial and azimuthal magnetic field components filtered by the 150s- 600s band-pass filter.

CHAPTER V

Improvement of space weather forecasting

5.1 Introduction

The structure of solar wind and the orientation of the interplanetary magnetic field (IMF) determine the level of geomagnetic activity, which is characterized by dramatic changes in the plasmasphere, radiation belts and the ionosphere. These changes impact the normal use of satellites, GPS signals, and even the electric power system. Extensive studies have shown that the southward component of IMF (southward IMF) is the predominant factor of the upstream driver. Figure 5.1 shows the comparison between the global two-temperature corona and inner heliosphere model and the observations at 1 AU from STEREO-A (STA, left), STEREO-B (STB, middle), and ACE (right), respectively. The cyan/red-dashed lines in the figure show the original observational data with a time resolution of 10 minutes/1 day (*Jin et al.*, 2012). There are many fine structures that cannot be captured by the steady-state MHD solutions. Figure 5.2 shows the comparison between in situ measurements observed by STA and simulation results for an extreme fast CME on July 23, 2012 based on a combined kinematic and MHD simulation model (*Liou et al.*, 2014). Constrained by the set up of the model that photospheric field is assumed to be in the radial direction at r=2.5R_S, the model cannot provide the realistic vectors of the magnetic field, which is true for all data-driven global MHD simulations (*Manchester et al.*, 2004; *Odstrcil*

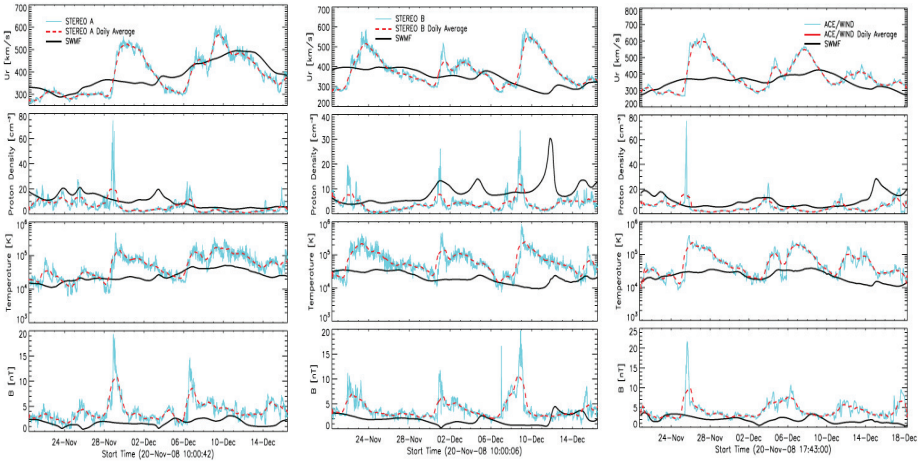

Figure 5.1: Comparison of STEREO A (left), STEREO B (middle), and ACE (right) observed solar wind speed, proton density, proton temperature, and magnetic field with the steady-state simulation from two-temperature model output for CR2077. (*Jin et al.*, 2012)

et al., 2005; *Wu et al.*, 2007; *Lugaz and Roussev*, 2011; *Shen et al.*, 2011). It is shown in Figure 5.2 that the arrival time of the sudden field increase, which indicates the shock front, matches well with the simulated field. However, there are differences in the flow structure, such as the small increases of solar wind speed and magnetic field prior to the shock in the observations do not appear in the simulation results. Though current heliospheric models have improved predictions of many observational parameters, these models do not predict or provide low-accuracy predictions of IMF Bz (*Jin et al.*, 2012; *Liou et al.*, 2014; *Shen et al.*, 2014). Thus the development of methods to provide accurate prediction of southward IMF in the near-Earth region is essential for the development of space weather models.

Based on in situ observations at 1 AU, previous studies have defined several solar wind transients that are potential triggers of geomagnetic disturbances, such as interplanetary coronal mass ejections (ICMEs), stream interaction regions (SIRs), and so on (*Denton et al.*, 2006; *Tsurutani et al.*, 2006, 2013). The different solar wind transients are identified by their different plasma and magnetic field signatures. *Zurbuchen and Richardson* (2006) summarized the observational signatures of magnetic

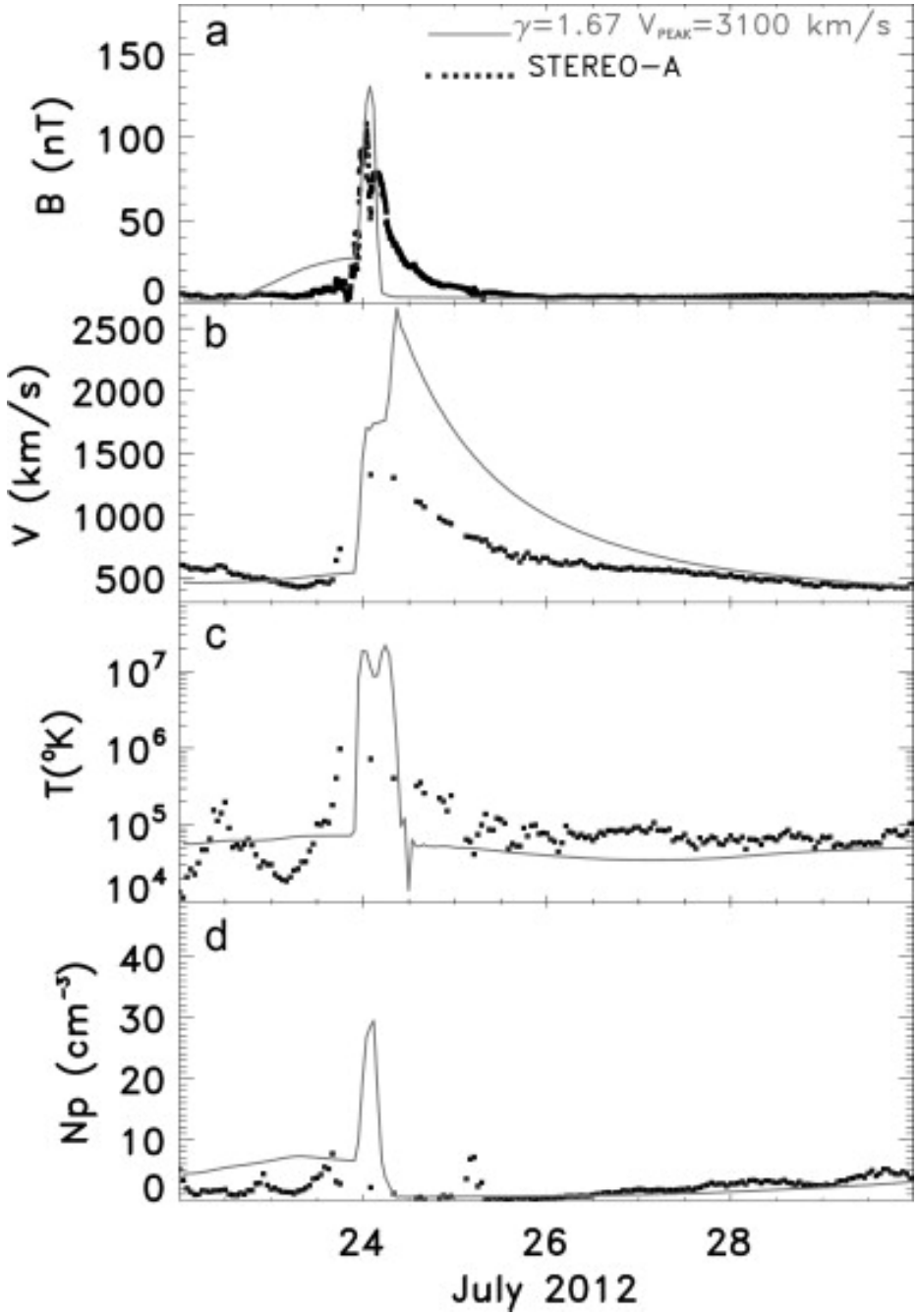

Figure 5.2: Comparison of simulated (gray lines) and STEREO-A observational (black dots) data for (a) total magnetic field strength, (b) solar wind bulk flow speed, (c) temperature, and (d) the proton number density. Plasma data gaps exist on and around day 206 (July 24) of year 2012 due to instrument saturation. The simulation suggests that the second peak in the magnetic intensity is associated with a reverse shock. (*Liou et al.*, 2014)

cloud ICMEs, which are an enhancement (> 10 nT) of magnetic field amplitude, along with smooth rotation of its polarity, and also a decreasing velocity/density profile. *Jian et al.* (2006a) did a statistical study of SIRs during 1995 - 2004 and concluded that the averaged peak pressure of an SIR is 176 ± 6 pPa, and the averaged speed increase is 230 ± 5 km/s. In our previous studies *Zhang and Moldwin* (2014) and *Zhang et al.* (2014), we identified long-duration and large-amplitude IMF Bz south intervals and categorized them based on the type of solar wind transient they were associated with. (See chapters III and IV)

McPherron and Siscoe (2004) applied the concept of air mass climatology to solar wind for probabilistic forecasting of geomagnetic indices. They used the stream interface (the interface within a corotaing compression region) as "marker", which is identified by a bipolar deflection of solar wind flow in the east-west (EW) direction. They set the polarity change of the EW flow deflection as the zero epoch time and carried out superposed epoch analysis of solar wind/IMF parameters and analysis of cumulative probability distribution functions for geomagnetic index ap for corotating interaction regions in 1995. Here we perform a follow-up study of *McPherron and Siscoe* (2004), focusing on the southward component of IMF as a marker. Although many studies have shown the correlation between magnetospheric activity and multiple solar wind/IMF parameters, the southward IMF is still the most important, and worst predicted component. Thus it is important to study the solar wind and IMF behavior as well as geomagnetic activity before and during the southward IMF intervals to learn more about their precursors and effects. We include more types of solar wind transients such as ICMEs, SIRs, and Alfvénic events, and also extend the analysis to geomagnetic indices like SYM-H, AE and ULF wave power and nearly a complete solar cycle of ICME- and SIR- related events (1995 - 2004) for a comprehensive study of solar wind-magnetosphere interaction.

Following in this chapter, we discuss the probabilistic forecasting analysis tech-

nique and the potential use of in situ and remote measurements for predicting the emergence and strength of IMF Bs-events.

5.2 Probabilistic forecasting analysis of geomagnetic indices for IMF Bs-events

In order to study the statistical effect of IMF Bs-events on the Earth's magnetosphere, we analyzed the relationship between a set of geomagnetic activity indices and IMF Bs-events associated with different kinds of solar wind transient structures using the probabilistic forecasting technique (*McPherron and Siscoe*, 2004). Our methodology is described as follows:

(1) We extract the 12-hour data before and after the zero epoch time for all the events since a preliminary analysis shows that most features of solar wind/IMF - magnetosphere variations occur in the -12 to 12 hour intervals around the zero epoch time. We then compare the averaged value of Vsw, Ey, Np, dynamic pressure (Psw) during each of the 12-hour intervals and their median values for all the events. We examined the distribution of the solar wind parameters to understand how best to statistically characterize them. We found that the solar wind speed is Gaussian-like and the proton density is a log-normal distribution. Also our dataset covers the southward IMF events for seven years (Alfvénic events) and ten years (ICME and SIR events). Thus the median values are reasonable baselines to distinguish the higher and lower level of the specific parameters. We choose these solar wind parameters since they are considered as important components for geomagnetic activity, and they are the parameters provided by current heliospheric models. These cases are categorized into different classes, such as fast/slow, large/small dynamic pressure variation, or high/low density, by dividing the distribution into two parts above and below the median. We then calculate the cumulative probability of the minimum SYM-H index

value during the two 12-hour periods, which gives the probability that the absolute value of minimum SYM-H will exceed the absolute value on the abscissa.

(2) Calculate the cumulative probability in the same way as step (1) for AE index, but value shows the probability of the maximum AE index greater than a given value.

(3) The 1-min geosynchronous magnetic field data available from GOES (*Singer*, 1996) are also projected to the Mean Field-Aligned (MFA) coordinate system (*Takahashi et al.*, 1990; *Zong et al.*, 2007), in which the parallel direction p is determined by 20-min sliding averaged magnetic field, the azimuthal direction is parallel to the cross product of the (p) and the spacecraft position vector, and the radial direction (r) completes the triad. Then the magnetic field data are filtered with the 150 s-600 s band-pass filter (ULF Pc 5 wave frequency band), and we use the maximum value of the filtered magnetic field magnitude for the 12-hour prior and 12-hour after the zero epoch time for each event in the three categories (ICME, SIR, Alfénic) to represent the amplitude of the ULF wave activity. *Sanny et al.* (2007) found a local time dependence of ULF wave power, which varies by at most one order of magnitude during strong magnetic storms. However, the variation pattern of the ULF wave power shows to be a two-cycle sinusoidal function, while the peaks of the two cycles ($\sim$ 12-hour interval) change by at most half an order (the wave amplitude change at most a quarter order). Thus the maximum value of the ULF wave amplitude in a 12-hour interval in our analysis well represents the strength of ULF wave activity at geosynchronous orbit.

Figure 5.3 presents the cumulative probability distribution function for the SYM-H index, which gives the probability that SYM-H will be smaller than the ordinate. The curves are based on data recorded during 12 hours before (more northward) and after (when Bz > -5 nT or more "northward") the zero epoch illustrated in Figure 412-4.14.. SYM-H at value of -50 nT is marked by the vertical line, which is widely used as the threshold of a geomagnetic storm. For all types of Bs-intervals except

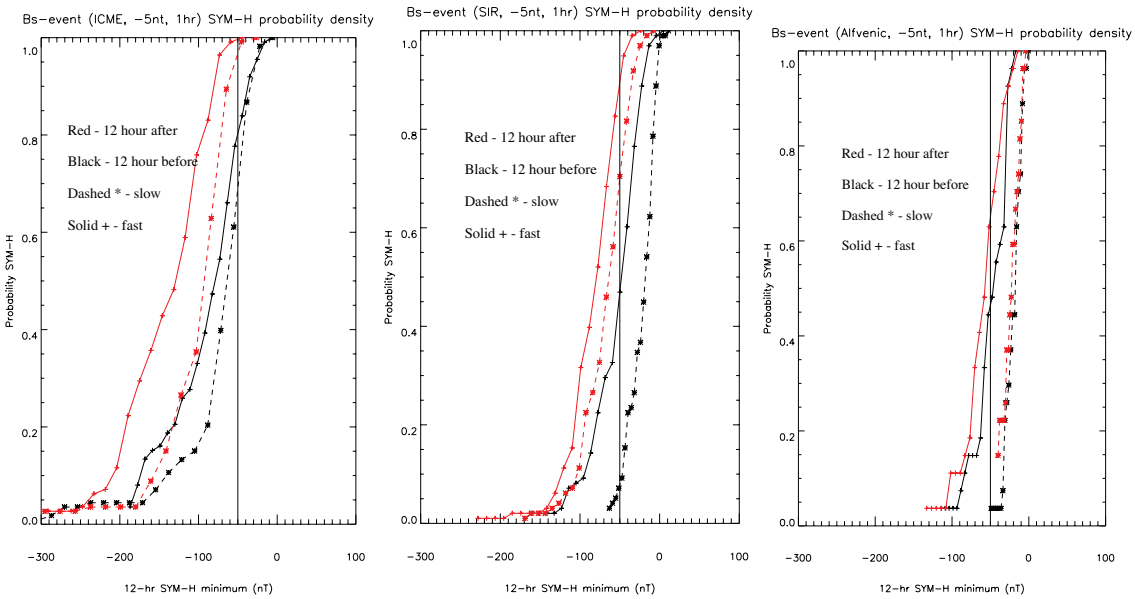

Figure 5.3: Probabilistic curves for SYM-H for 12 hours before (black) and after (red) the zero epoch of southward IMF-intervals associated with different solar wind structures. Each case shows two curves corresponding to high and low solar wind speed. The solid/dashed line is for events in which the solar wind speed is faster/slower than the median speed for all cases. The vertical line marks the SYM-H value of -50 nT.

Alfvénic events, the probability that SYM-H will be below a given value is greater after the zero epoch than before the zero epoch. Within either 12-hour interval, high Vsw conditions are more geoeffective than slow Vsw conditions for ICME- and SIR-related events. However for Alfvénic Bs-intervals, the fast solar wind before the zero epoch leads to higher probability of geomagnetic storms than intervals with slow solar wind after the zero epoch. The data shows that fast solar wind intensifies geomagnetic storms, while the strong southward IMF is the key for triggering such activity, except for Alfvénic events.

Figure 5.4 shows the difference between high and low proton density in terms of the probability to trigger geomagnetic storms in the same format as Figure 5.3. For the ICME-type Bs intervals, the cumulative probability function for low density conditions are above the high density conditions when minimum SYM-H is less negative than -60 nT during either of the 12 hour windows. For the Bs intervals related with

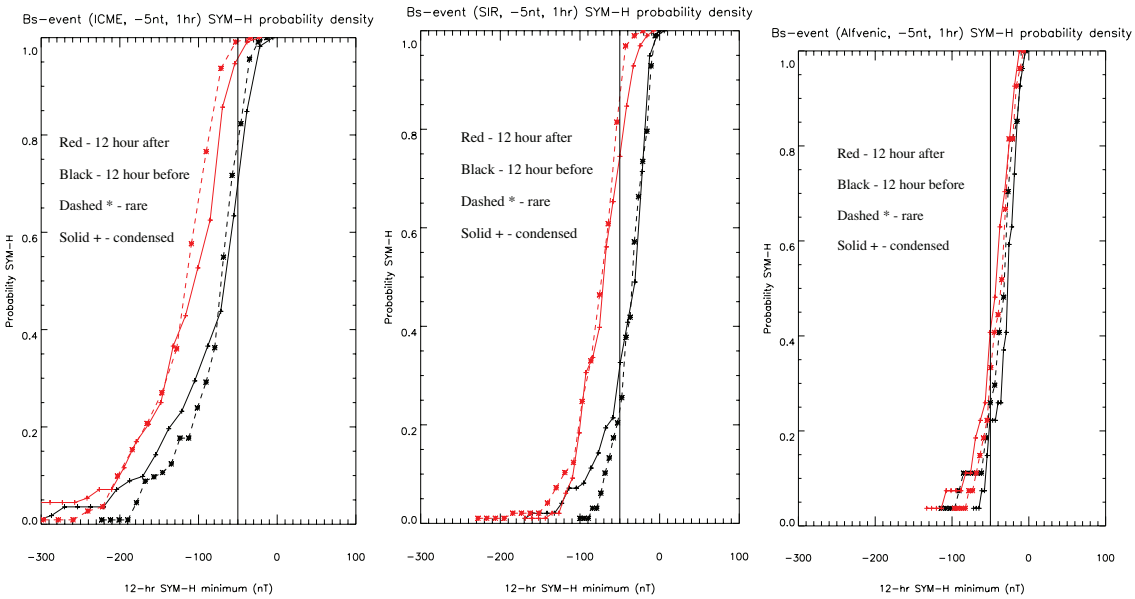

Figure 5.4: The same format as Figure 5.3 but showing the impact of high or low proton density.

SIR, the low proton density condition is more likely to trigger a stronger geomagnetic storm during the whole 24 hour period, which is the same for Alfvénic Bs events (though the PDF are very similar). However, like the effect of Vsw, the probability function of low proton density before the zero epoch overlaps with the high density conditions after the zero epoch for Alfvénic events. This indicates that solar wind density does not intensify geomagnetic activity significantly, or correlate with SYM-H well, suggesting that it impacts the magnetosphere differently than solar wind speed.

The comparison of AE index distribution functions between conditions of fast and slow solar wind during the 12-hour intervals before and after the turning of IMF to more southward is illustrated in Figure 5.5. The format is the same as Figure 5.3, but the function shows the probability of AE exceeding the ordinate. AE at value of 1000 nT is marked by the vertical line, which is often taken as the threshold of a geomagnetic substorm. It shows that the distribution function for fast solar wind always has a greater AE than slow solar wind during both 12-hour intervals for all kinds of Bs-events, which is the same as the SYM-H. However, fast solar wind during

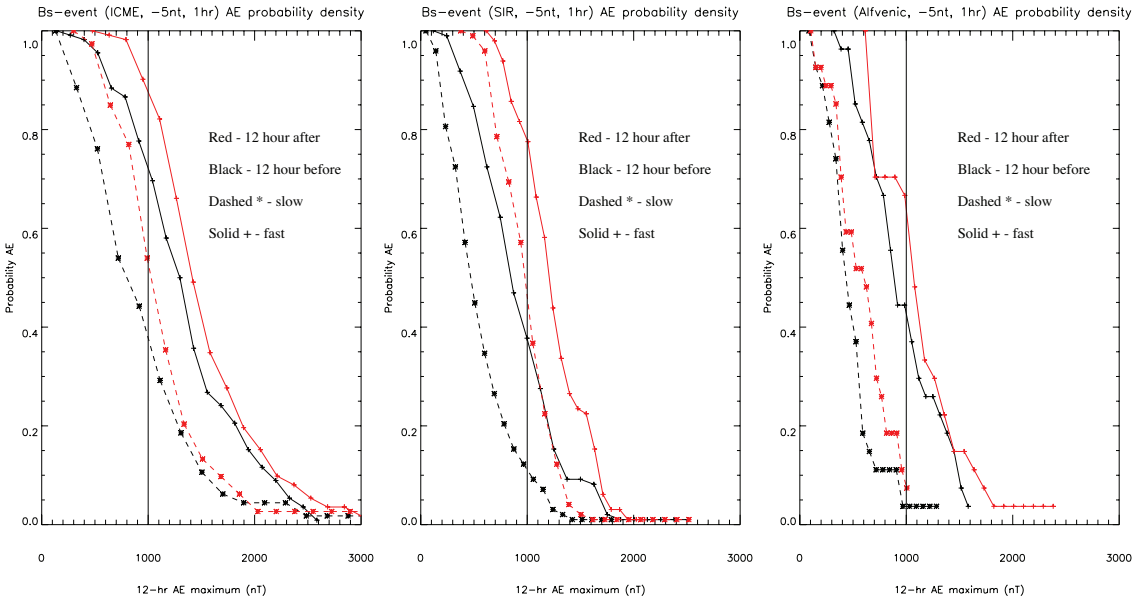

Figure 5.5: The same format as Figure 5.3 but for cumulative probability distribution of AE index.

the 12-hour interval before the zero epoch time presents higher occurrence probability of larger AE than the slow solar wind during the 12-hour interval after that for all type of Bs intervals, except that the two curves almost overlap for SIR-type Bs-events. It is suggested that fast solar wind is important in inducing and amplifying geomagnetic substorms for most of the cases, but strong southward IMF is not necessarily the key.

We also performed analysis of Ultra Low Frequency (ULF) wave amplitude at geosynchronous orbit using GOES data. Figure 5.6 illustrates the cumulative probability of the maximum amplitude of the magnetic field in ULF wave frequency band (1.6 - 6.7 mHz) for different degrees of Psw variability, in the same format as Figure 5.3. It shows that for all types of Bs-events, the higher variability of Psw is related with larger ULF wave amplitude in both 12-hour windows. For the SIR-type and Alfvénic Bs-events, the larger perturbation of Psw during the more northward interval (12 hours before) has lower probability to induce more intense ULF wave activity than the weaker perturbation of Psw during the more southward interval (12 hours after). But for the ICME-related Bs-events, larger deviation of Psw during the more

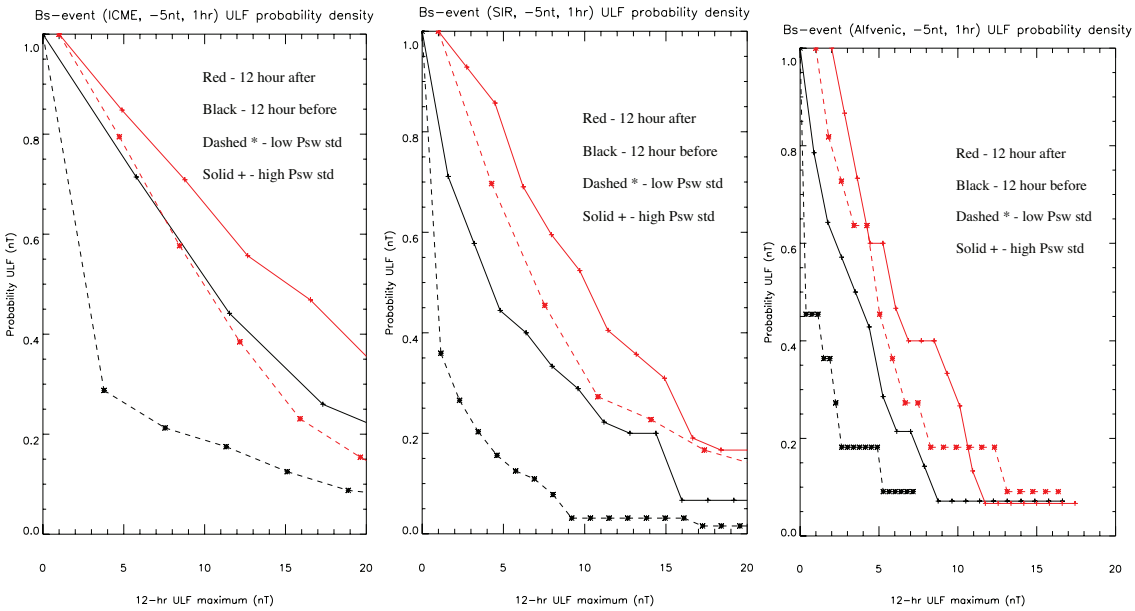

Figure 5.6: The same format as Figure 5.3 but for cumulative probability distribution of the maximum value of total magnetic field in ULF wave frequency band (1.6 - 6.7 mHz) measured by GOES satellite, in terms of the standard deviation of solar wind dynamic pressure (Psw).

northward IMF period is even more associated with stronger perturbations of ULF waves in the magnetosphere than lower Psw deviations during the more southward IMF interval. We also tested the relationship between the median value of Psw and ULF wave activity, and obtained similar results. However the probability of high ULF wave amplitudes are enhanced for weak Psw compared to strong Psw during the 12-hours after the zero epoch time for SIR-type Bs-events. These results suggest that the variability of solar wind dynamic pressure (rather than absolute value) plays the most significant role in inducing intense ULF wave activity in Earth's magnetosphere, however the strong southward IMF associated with solar wind transients is more likely to trigger geomagnetic storms as well as important in intensifying ULF wave amplitude in this frequency band.

5.3 Potential improvements of space weather forecasting depending on in situ and remote sensing measurements

Vrsnak et al. (2007) investigated the relationship between the coronal hole (CH) area/position and physical characteristics of the associated corotating high-speed stream (HSS) in the solar wind at 1 AU using the remote imaging and in situ data in the period DOY 25 - 125 of 2005 including a weak CME. They found a significant correlation between the daily averaged CH parameters and the solar wind parameters, which could be used for predicting the solar wind speed, proton density for several days in advance in periods of low CME activity. Their forecast technique is based on monitoring fractional areas covered by CHs in the meridional slices as shown in Figure 5.7. They presented that the solar wind speed is predictable with the highest accuracy, for which the difference of the peak value between the prediction and observation is up to 10%.

We have shown in chapter III that the low-latitude coronal hole (LLCH) with adjacent active region or brightened features is the potential source region of corotating interaction region (CIR) with large-amplitude, long-duration IMF Bs-events, thus we did a further study of the evolution of the LLCH and the adjacent active structures. We tracked a LLCH with adjacent AR that is evolving and diminishes in the end from January 2, 2008 to March 2, 2008. Figure 5.8 presents the EUV images taken by STEREO satellites for almost three solar rotations. The panels on the left are measurements from STB on Jan 2, Jan 29, and Feb 24 from top to bottom, respectively. The panels on the right are obtained by STA on Jan 5, Feb 1, and Feb 28 from top to bottom. The LLCH presented in these panels is the source region of several CIRs observed by in situ satellites. It is shown that the CH is expanding over time while the nearby active region is weakened and almost diminishes in the bottom panels.

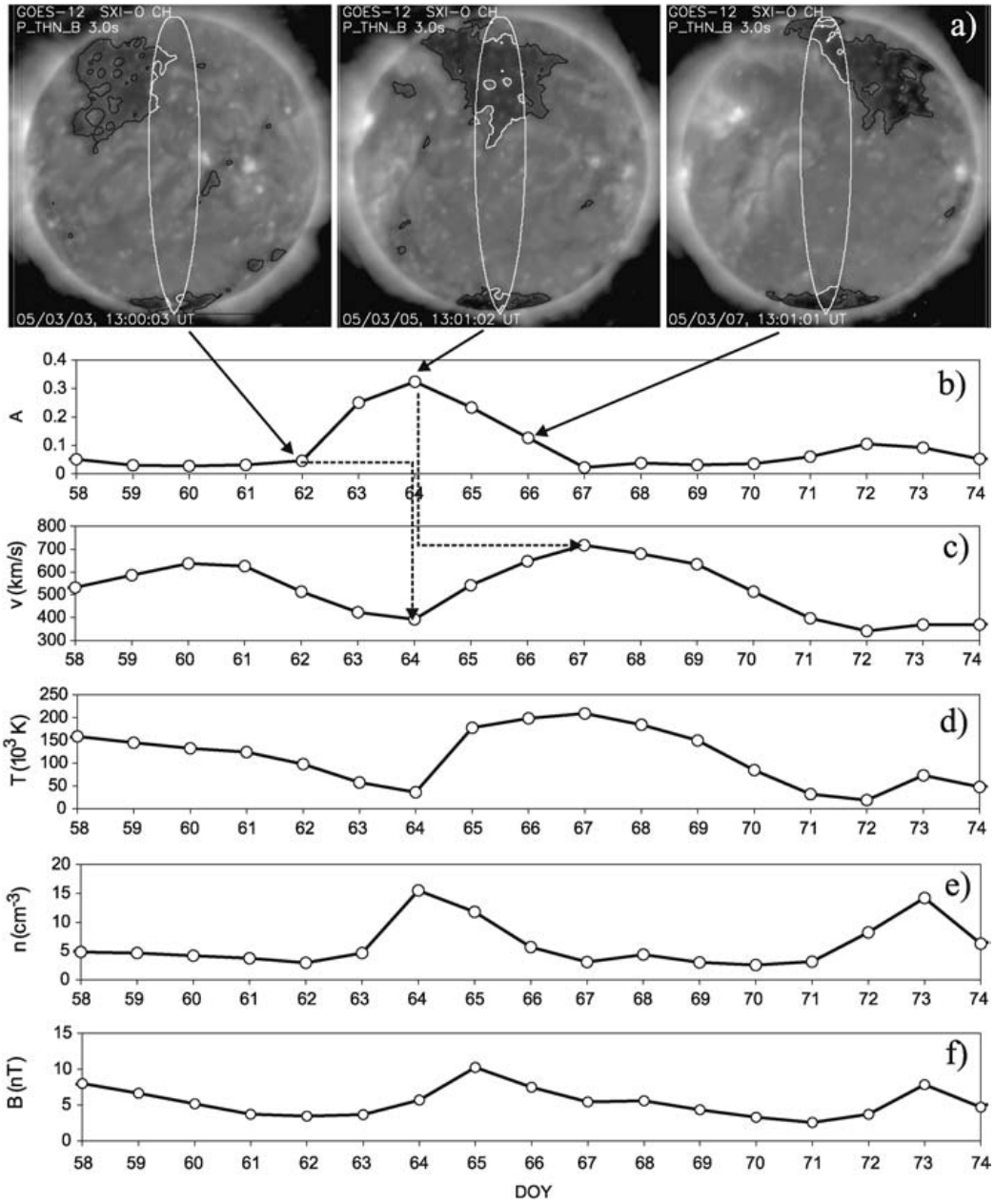

Figure 5.7: a) Transition of a large coronal hole over the solar disc recorded by GOES-SXI. The considered meridional slice [10°, 10°] is outlined in white. The derived coronal hole boundaries inside the slice are also outlined in white. The coronal hole boundaries outside the slice are indicated in black. b) Daily measurements of the CH fractional area A in the M slice ([-10°, 10°], depicted in a). c) - f) ACE daily averages of the solar wind parameters: flow velocity v, proton temperature T , density n, and magnetic field strength B. The x-axis represents DOY for 2005. Bold arrows connect images with the corresponding CH measurements. Dashed lines outline the time lag between a CH measurement and the corresponding 1 AU effect. (*Vrsnak et al.*, 2007)

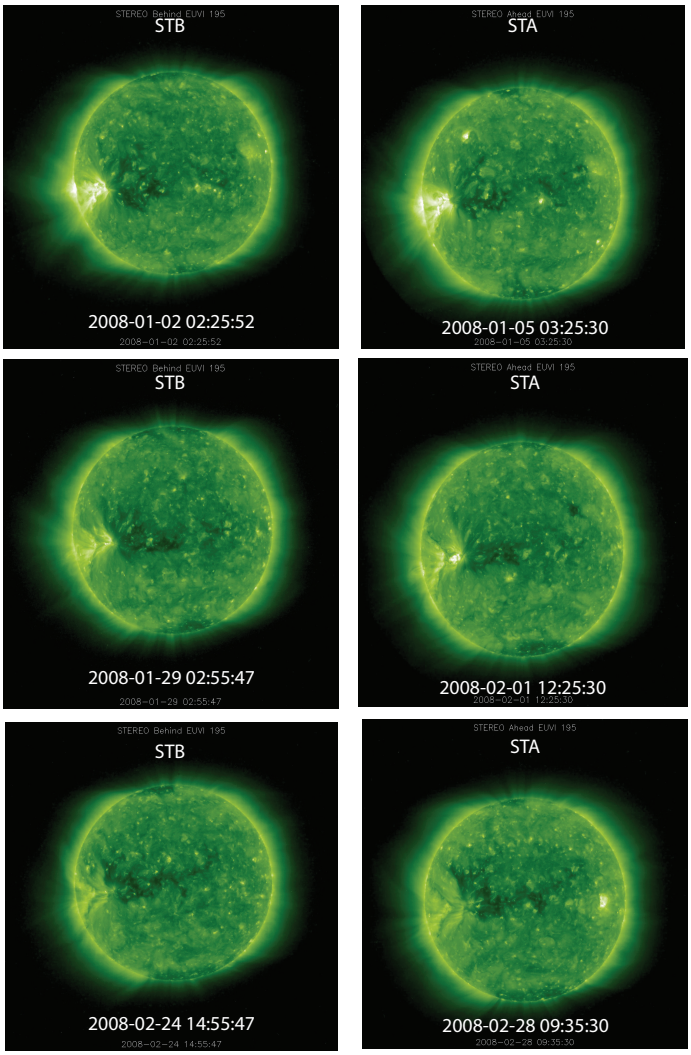

Figure 5.8: The EUV images taken by STEREO satellites for almost three solar rotations. The panels on the left are measurements from STB on Jan 2, Jan 29, and Feb 24 from top to bottom, respectively. The panels on the right are obtained by STA on Jan 5, Feb 1, and Feb 28 from top to bottom.

Figure 5.9 presents the plasma and magnetic field measurements from STB, ACE, STA (left to right) for a CIR observed on Jan 3, 2008 by STB and Jan 6 by STA ejected from the LLCH shown in the first panel in Figure 5.8. It is illustrated that the solar wind speed is increasing from $\sim$ 300 km/s to 600 km/s based on the observations from all the three satellites. However, the density decreases from 40 cm^{-3} to below 10 cm^{-3} for ACE and STA measurements, while from 25 cm^{-3} to 5 cm^{-3} for STB. These features match well with the definition of CIR based on in situ satellite measurements. The top panels show that the total magnetic field has a peak in the period with peak-valley-value about 20 nT at all the three satellites. From the blue line in the second panel on the left, it is shown that there is a southward IMF interval with minimum Bz below -10 nT lasting for about 2 hours observed by STB. From the ACE observation in the middle, it is presented that the IMF Bs-event also occurred with similar parameters corresponding to the same period of the CIR - solar wind speed is increasing. STA measurements on the right show two IMF Bs intervals with minimum Bz about -10 nT for 2 hours.

Figure 5.10 illustrates the SW/IMF parameters from STEREO and ACE during the CIR corresponding to the LLCH observed by STB on Jan 29 and STA on Feb 1 after a solar rotation from Figure 5.9. The change of the amplitude for solar wind speed and density is similar as in Figure 5.9, however the compressed region (increased density) is thinner. The density measurement from ACE before 16:00:00 on Jan 31 is not available, thus the abrupt jump is not realistic. The magnetic field does not show a significant peak as in Figure 5.9, but a flattened maximum value slightly weaker than the peak in Figure 5.9. The southward IMF interval is shown in STB measurements with minimum Bz below -10 nT for about 1 hour, while the IMF Bs-event observed by ACE is weakened with the minimum Bz about -5 nT, which is also shown in STA observations on the right.

Figure 5.11 shows the SW/IMF parameters from STEREO and ACE during the

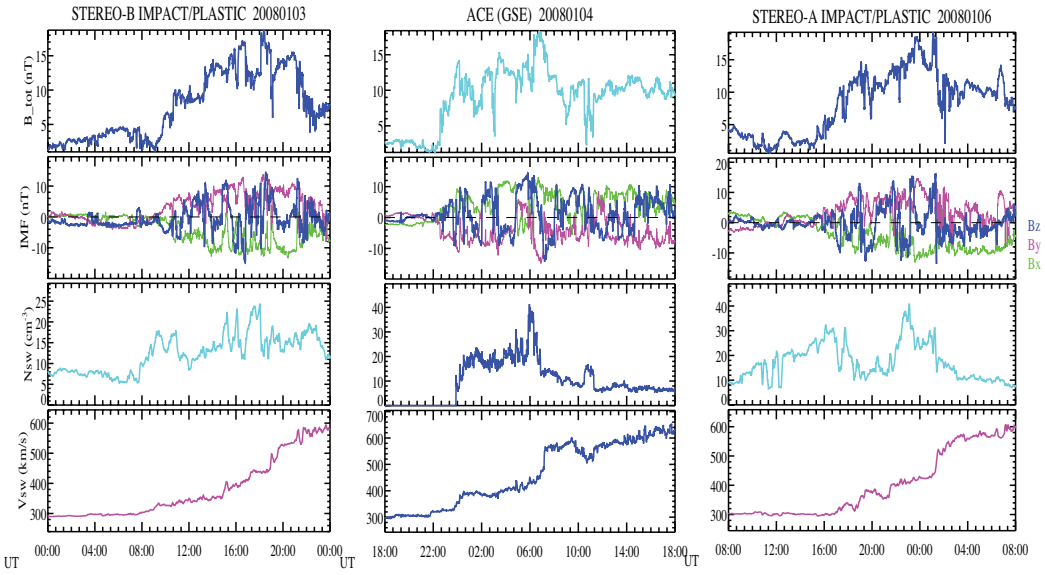

Figure 5.9: Measurements of IMF amplitude, IMF vectors, solar wind density, and solar wind speed (from top to bottom) from STB, ACE and STA during the CIRs ejected from the LLCH in the EUV image taken by STB on Jan 2 and STA on Jan 5, 2008 in the top panel in Figure 5.8. The duration is one day for all the three satellites. The zero value of Bz is marked by the horizontal dashed line in the second panel.

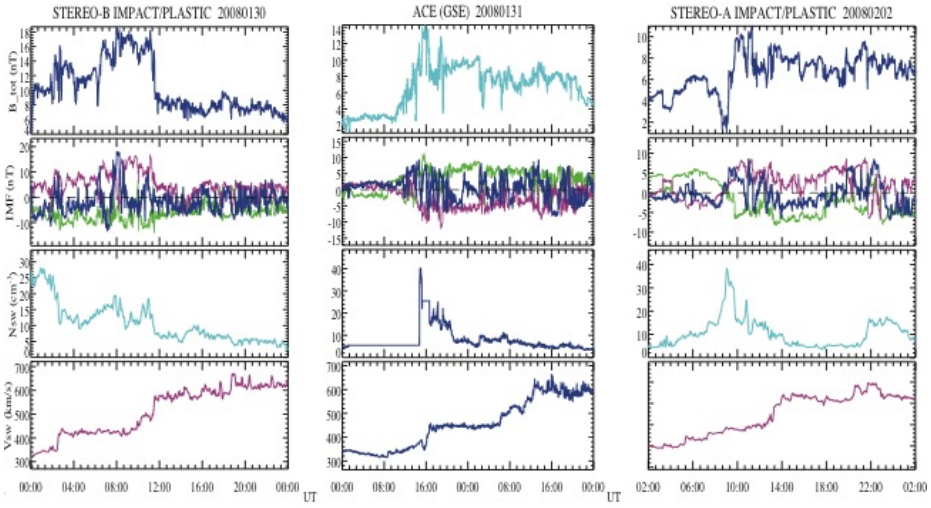

Figure 5.10: The measurements of IMF/SW from STB, ACE, and STA for the CIR corresponding to the LLCH shown in the second panel in Figure 5.8 in the same format as Figure 5.9. It is noted that the duration for the ACE observation is 2 days here.

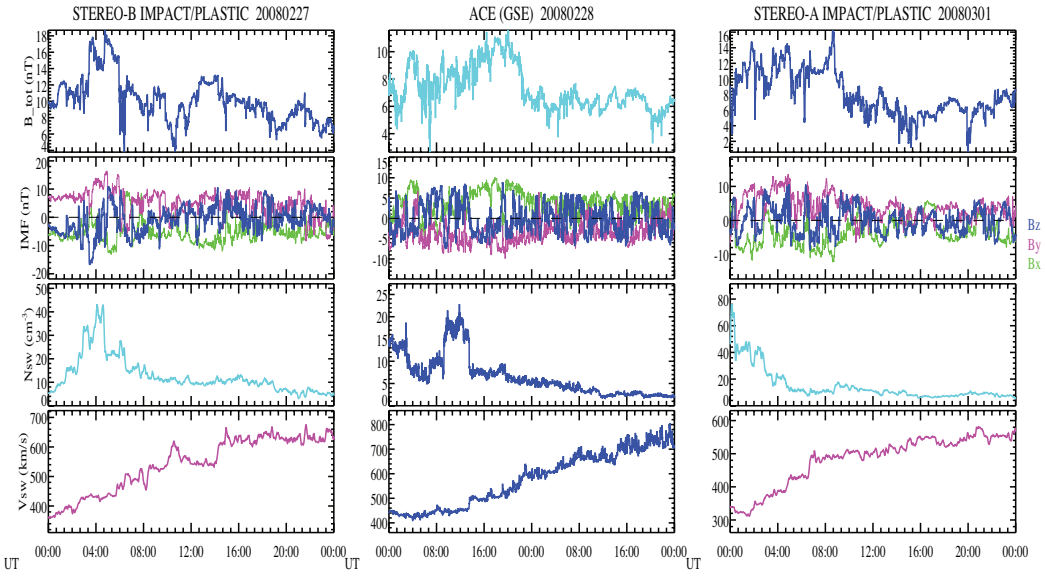

Figure 5.11: The measurements of IMF/SW from STB, ACE, and STA for the CIR corresponding to the LLCH shown in the bottom panel in Figure 5.8 in the same format as Figure 5.9. It is noted that the duration for the ACE observation is 2 days here.

CIR corresponding to the LLCH observed by STB on Feb 24 and STA on Feb 28 after a solar rotation from Figure 5.10. The change of solar wind speed observed by STEREO is similar as in Figure 5.8 and Figure 5.9, however the speed changes from 400 km/s to 800 km/s measured at ACE for this CIR. While the density peak measured by ACE is only 20 cm^{-3}, the maximum value of the density at STB is over 40 cm^{-3} and that at STA is about 80 cm^{-3}. Simultaneously, the total magnetic field shows a great increase at all three satellites. From the blue lines in the second panel in the middle and on the right, it is shown that the IMF Bs-events observed by ACE and STA are even weaker than that in Figure 5.10.

Comparing Figures 5.8 - 5.11, we suggest that the occurrence and intensity of the AR adjacent to the LLCH are important factors for the emergence and intensity of the IMF Bs-events observed at 1 AU. Besides the geometric parameters of the LLCH, such as the area, the longitudinal and latitudinal expansion are also effective to the IMF Bs-events. Since the LLCH is often a long-lasting phenomena that can

be seen in solar images obtained by STEREO satellites, and it is possible to track the evolution of the active region, the further study of this relationship is of great potential to improve the space weather forecasting system.

5.4 Conclusions

The statistical analysis of the IMF/SW parameters and the geomagnetic activity indices using the probabilistic forecasting technique shows that solar wind parameters affect the Earth's magnetosphere in different ways, also different regions of geomagnetic field respond to the same solar wind parameters in different ways. Like weather forecasts, this technique provides a tool for predicting the occurrence rate of geomagnetic activity with intensity level based on a combination of various solar wind quantities, obtainable from either measurements or models. We also showed that the occurrence and intensity of the active region adjacent to the LLCH, as well as the geometric parameters of the LLCH are important factors to the intensity of the IMF Bs intervals observed at 1 AU, especially at the near-Earth region.

CHAPTER VI

Conclusion and Discussion

6.1 Conclusions

This thesis provides a comprehensive study about the source, evolution, and properties of non-Parker-spiral IMF and its role on geomagnetic activity. This systematic study includes direct observational data analysis, theoretical development, and predictive modeling to obtain an insightful understanding of the southward IMF intervals.

In chapter 2, we analyzed the data from multiple satellites - Helios, Ulysses, WIND, ACE, and STEREO for solar cycle 22 - 24, and concluded that the emergence of the non-Parker-spiral is not from random fluctuations of the solar wind or IMF, but physical mechanisms in the solar atmosphere or interaction in the interplanetary medium. We also pointed out that the moderate and strong IMF Bs-events are well correlated with the yearly profile of SSN, but not for the weak IMF Bs intervals. Moreover, we have investigated the the spatial distribution of IMF Bs-events by comparing the statistical analysis of data from different satellites and find that the non-Parker-spiral component of IMF is decreasing faster than inversely proportional to the radial distance from the Sun, It implies that the sources of some large-scale IMF Bs-events could be processes like reconnection in the local interplanetary medium or solar wind transients expanding in a similar way as CMEs in the interplanetary region.

In chapter 3, we have examined the relationship between the southward IMF intervals and different types of solar wind transients to identify the sources of this component. Comparing the in situ and remote sensing observations, we have also proposed the potential sources of the LALD southward IMF events not discussed in the literature. We have find that:

1. The major contribution to the LALD IMF Bs events is from solar wind transients (MC, ISMFR, ejecta, SIR, Alfvénic fluctuations).

2. Most of the LALD IMF Bs intervals unrelated with these structures show a discontinuity or slow-mode shock at both or either boundary.

2. There are some events identified as ICME or SIR based on our criteria but missing from previous published lists, which also contribute to the occurrence of LALD IMF Bs-events. Ion charge state data are good indicators of the source region of the solar wind based on the analysis of in situ measurements.

3. The Alfvén fluctuations carrying LALD Bs intervals in our study originate as perturbations in the magnetic field on the Sun and propagate outward. If Alfvén waves in the solar wind have different source regions in the solar corona, which in turn affect their efficiency in accelerating the solar wind, the differences will be manifeste in different spectra and plasma properties in the solar wind at further heliocentric distance.

4. The low-latitude coronal hole (LLCH) with nearby solar activities in the closed magnetic field configuration, such as active region (AR) and bright loops, is the solar source of LALD IMF Bs intervals related with CIR.

In chapter 4, we performed the analysis of the correlation between the LALD IMF Bs-events and the geomagnetic activity indices, and the effect of their association with different kinds of solar wind transient structures on the geomagnetic disturbance level. We suggested that the strongest storms and substorms are not associated with the same event except the ejecta-type Bs events, and that for large storms, we also note

that great Bs events (Bz < -10 nT, t > 3 hrs) do not always induce large storms. We also pointed out that MC, ejecta, and SIR drive storms in different ways, which is consistent with *Borovsky and Denton* (2006) that CME-driven storms are brief with strong D_{st} while SIR-driven storms are of longer duration, and that the co-occurrence of high-speed solar wind in different types of Bs events account for the different behaviors of the Earth's magnetosphere. We also demonstrated that while Alfvénic Bs-events are relatively weak in triggering geomagnetic storms, they are possible drivers of large-scale ULF wave oscillations in the Earth's magnetosphere.

In chapter 5, we described the probabilistic forecasting technique for predicting the geoeffectiveness of LALD IMF Bs-events. We also discussed the potential improvement of predicting the occurrence and intensity of IMF Bs-events using in situ and solar remote observations. We showed that solar wind parameters affect the Earth's magnetosphere in different ways, also different regions of geomagnetic field respond to the same solar wind parameters in different ways. We suggest that this technique provides a tool for predicting the occurrence rate of geomagnetic activity with intensity level based on a combination of various solar wind quantities, obtainable from either measurements or models. We also propose that the occurrence and intensity of the active region adjacent to the LLCH, as well as the geometric parameters of the LLCH are important factors in determining the intensity of the IMF Bs intervals observed at 1 AU, which could be utilized to improve the current space weather forecasting system.

6.2 Future work

Throughout this work, we have reported the initial findings of the statistical features, potential sources and geoeffectiveness of non-Parker-spiral component of IMF using in situ and remote sensing observations from multiple satellites. The availability of continuous in situ data from upcoming missions, such as Solar Orbiter and Solar

Probe Plus, has made it possible to answer key questions regarding the evolution of IMF Bs intervals in the passage from the solar atmosphere through the interplanetary medium to the near Earth environment.

We have mentioned in chapter 3 that most of the LALD IMF Bs intervals unrelated with these solar wind transients began or ended with a discontinuity or slow shock. *Burlaga* (1970) suggested that most discontinuities originate within 0.8 AU and do not evolve appreciably between 0.8 AU and 1.0 AU, other than those generated from the interaction of fast and slow streams near 1 AU. *Whang et al.* (1998) and *Gosling et al.* (2006) also proposed that local, quasi-stationary reconnection occurs relatively frequently in the solar wind and produces Petschck-type exhausts, which could in turn form slow shocks. *Vasquez et al.* (2007) surveyed the small magnetic field discontinuities of Bartels rotation 2286 and found that most discontinuities come from Alfvénic turbulence. A further investigation of the discontinuity features at the boundary of IMF Bs-events is expected to provide more information about the solar sources of the IMF Bs intervals.

The natural extension of this work includes the exploration the measurements of solar wind ion charge state for the IMF Bs-events that are not identified to be related with any type of solar wind structures. As mentioned in chapter 3, the plasma features, such as proton density, velocity, temperature, could be affected by the interplanetary medium conditions along the way from the Sun to the satellites, however the heavy ion charge state is the only property that would almost keep the information of the solar origin of the plasma observed at in situ. Thus it will be possible to determine the solar source of the large-amplitude, long-duration IMF Bs-events that have not been categorized yet in our list.

In chapter 5, we presented the relationship between the LLCH-AR feature on the Sun and the occurrence of large-amplitude, long-duration IMF Bs-events at 1 AU. The next logical step is to further analyze the imaing data for the quantitative

information of the evolution of the LLCH and nearby ARs/bright loops over more solar rotations, and compare with the in situ observations of the IMF Bs-events. It is expected that the quantitative correlation between the phenomena on the Sun and observed by in situ satellites will be obtained as a tool for predicting the occurrence of large-amplitude, long-duration IMF Bs-events related with CIRs.

One additional project that would have a great impact to the general space weather community, is a more robust regression model between the solar wind/IMF parameters, or even the solar imaging data, and the geomagnetic activity indices. Besides the basic linear regression model (Pearson's linear regression) we used in the current study, the more advanced techniques for regression, such as generating mediate parameters, weighting on parameters, could potentially improve the forecast ability of the space weather events.

BIBLIOGRAPHY

BIBLIOGRAPHY

Akasofu, S. I. (1968), Polar and Magnetospheric Substorms, *D. Reidel, Norwell, Mass.,*.

Akasofu, S. I. (1979), A Search for the Interplanetary Quantity Controlling the Develoment of Geomagnetic Storms, *Royal Astronomical Society, Quarterly Journal*, *20*, 119–137.

Akasofu, S. I. (2002), The development of the auroral substorm, *Planet. Space Sci.*, *12*, 273–282.

Arnoldy, R. L. (1971), Signature in the Interplanetary Medium for Substorms, *J. Geophys. Res.*, *76*, 5189–5201.

Bame, S. J., J. R. Asbridge, W. C. Feldman, E. E. Fenimore, and J. T. Gosling (1978), SOLAR WIND HEAVY IONS FROM FLARE-HEATED CORONAL PLASMA, *Sol. Phys.*, *62*, 179–201.

Belcher, J. W., and L. Davis (1969), Large-Amplitude Alfvén Waves in the Interplanetary Medium: Mariner 5, *J. Geophys. Res.*, *74*.

Belcher, J. W., and L. Davis (1971), Large-amplitude Alfvén waves in the interplanetary medium, 2, *J. Geophys. Res.*, *76*, 3534–3563.

Borovsky, J. E. (2008), Flux tube texture of the solar wind: Strands of the magnetic carpet at 1 AU?, *J. Geophys. Res.*, *113*.

Borovsky, J. E., and M. H. Denton (2006), Differences between CME-driven storms and CIR-driven storms, *J. Geophys. Res.*, *111*.

Borrini, G., J. T. Gosling, S. J. Bame, W. C. Feldman, and J. M. Wilcox (1981), Solar wind helium and hydrogen structure near the heliospheric current sheet: A signal of coronal streamers at 1 AU, *J. Geophys. Res.*, *86*, 4565–4573.

Borrini, G., J. T. Gosling, S. J. Bame, and W. C. Feldman (1982), Helium abundance enhancements in the solar wind, *J. Geophys. Res.*, *87*, 7370–7378.

Bothmer, V., and R. Schwenn (1994), ERUPTIVE PROMINENCES AS SOURCES OF MAGNETIC CLOUDS IN THE SOLAR WIND, *Space Sci. Rev.*, *70*, 215–220.

Burch, J. L. (1972), Preconditions for the triggering of polar magnetic substorms by storm sudden commencements, *J. Geophys. Res.*, *28*, 5629–5632.

Burlaga, L. F. (1970), Discontinuities and shock waves in the interplanetary medium and their interaction with the magnetosphere, *NASA-TM-X*, *x-692-70-154*.

Burlaga, L. F., and J. M. Turner (1976), Microscale 'Alfvén Waves' in the Solar Wind at 1 AU, *J. Geophys. Res.*, *81*.

Burlaga, L. F., R. P. Lepping, and K. W. Behannon (1982), Large-Scale Variations of the Interplanetary Magnetic Field: Voyager 1 and 2 Observations Between 1-5 AU, *J. Geophys. Res.*, *87*, 4345–4353.

Burlaga, L. F., R. M. Skoug, C. W. Smith, D. F. Webb, T. H. Zurbuchen, and R. Reinard (2001), Fast ejecta during the ascending phase of solar cycle 23: ACE observations, 1998 - 1999, *J. Geophys. Res.*, *106*.

Burton, R. K., R. L. McPherron, and C. T. Russell (1975), An empirical relationship between interplanetary conditions and Dst, *J. Geophys. Res.*, *80*, 4204–4214.

Cane, H. V., and I. G. Richardson (2003), Interplanetary coronal mass ejections in the near-Earth solar wind during 1996-2002, *J. Geophys. Res.*, *108*.

Cartwright, M. L., and M. B. Moldwin (2008), Comparison of small-scale flux rope magnetic properties to large-scale magnetic clouds: Evidence for reconnection across the HCS?, *J. Geophys. Res.*, *113*, A09,105.

Chapman, S. (1919), Theories of Mangetic Storms, *The Observatory*, *42*, 196–206.

Choi, Y., Y.-J. Moon, S. Choi, J.-H. Baek, S. S. Kim, K.-S. Cho, and G. S. Choe (2009), Statistical Analysis of the Relationships among Coronal Holes, Corotating Interaction Regions, and Geomagnetic Storms, *Sol. Phys.*, *254*, 311–323.

Coleman, P. J. (1967), WAVE-LIKE PHENOMENA IN THE INTERPLANETARY PLASMA: MARINER 2, *Planet. Space Sci.*, *15*, 953–973.

Coleman, P. J., and R. L. Rosenberg (1971), North-South Component of the Interplanetary Magnetic Field, *J. Geophys. Res.*, *76*(13).

Crooker, N. U., C.-L. Huang, S. M. Lamassa, D. E. Larson, S. W. Kahler, and H. E. Spence (2004), Heliospheric plasma sheets, *J. Geophys. Res.*, *109*.

Davis, T. N., and M. Sugiura (1966), Auroral electrojet activity index ae and its universal time variations, *J. Geophys. Res.*, *71*, 785–801.

Denton, M. H., J. E. Borovsky, R. M. Skoug, M. F. Thomsen, B. Lavraud, M. G. Henderson, R. L. McPherron, J. C. Zhang, and M. W. Liemohn (2006), Geomagnetic storms driven by ICME- and CIR-dominated solar wind, *J. Geophys. Res.*, *111*.

Dessler, A. J. (1967), Solar Wind and Interplanetary Magnetic Field, *Rev. Geophys.*, *5*, 1–41.

Dungey, J. W. (1954), *Electrodynamics of the outer atmospheres*, Rep. 69, Ions. Res. Lab. Pa. State Univ., Unversity Park.

Dungey, J. W. (1961), Interplanetary Magnetic Field and the Auroral Zones, *Phys. Rev. Lett.*, *6*, 47–48.

Eastwood, J. P., P. Brown, T. M. O. nad B. J. Whiteside, P. Fox, N. Adeli, T. J. Beek, C. M. Carr, and N. Barnes (2014), Magnetic field measurements from a solar sail platform with space weather applications, *Advances in* S*olar* S*ailing*, pp. 185 – 200.

Ebert, R. W., M. A. Dayeh, M. I. Desai, and G. M. Mason (2012), COROTATING INTERACTION REGION ASSOCIATED SUPRATHERMAL HELIUM ION ENHANCEMENTS AT 1 AU: EVIDENCE FOR LOCAL ACCELERATION AT THE COMPRESSION REGION TRAILING EDGE, *The Astrophys. J.*, *749*, 73 – 86.

Echer, E., and W. D. Gonzalez (2004), Geoeffectiveness of interplanetary shocks, magnetic clouds, sector boundary crossings and their combined occurrence, *Geophys. Res. Lett.*, *31*.

Fairfield, D. H., and J. L. J. Cahill (1966), Transition Region Magnetic Field and Polar Magnetic Disturbances, *J. Geophys. Res.*, *71*(1), 155–169.

Feng, H.-Q., D.-J. Wu, C.-C. Lin, J.-K. Chao, L. C. Lee, and L. H. Lyu (2008), Interplanetary small- and intermediate-sized magnetic flux ropes during 1995-2005, *J. Geophys. Res.*, *113*, 12,105.

Feng, H.-Q., J.-K. Chao, L. H. Lyu, and L. C. Lee (2010), The relationship between small interplanetary magnetic flux rope and the substorm expansion phase, *J. Geophys. Res.*, *115*, A09,108.

Fenimore, E. E. (1980), Solar wind flows associated with hot heavy ions, *The Astrophys. J.*, *234*.

Forbush, S. E., S. P. Duggal, M. A. Pomerantz, and C. H. Tsao (1982), Random fluctuations, persistence, and quasi-persistence in geophysical and cosmical periodicities: A sequel, *Reviews of* G*eophysics*, *20*, 971–976.

Forsyth, R. J., et al. (2006), ICMEs in the inner heliosphere: Origin, evolution and propagation effects, *Space Sci. Rev.*, *123*.

Gloeckler, G., L. A. Fisk, S. Hefti, N. A. Schwadron, T. H. Zurbuchen, F. M. Ipavich, J. Geiss, P. Bochsler, and R. F. Wimmer-Schweingruber (1999), Unusual composition of the solar wind in the 2-3 may 1998 CME observed with SWICS and ACE, *J. Geophys. Res.*, *26*, 157 – 160.

Gonzalez, W. D., J. A. Joselyn, Y. Kamide, H. W. Kroehl, G. Rostoker, B. T. Tsurutani, and V. M. Vasyliunas (1994), What is a geomagnetic storm?, *J. Geophys. Res.*, *99*, 5771–5792.

Gonzalez, W. D., B. T. Tsurutani, P. S. McIntosh, and A. L. Gonzales (1996), Coronal Hole-Active Retion-Current Sheet (CHARCS) association with intense interplanetary and geomagnetic activity, *Geophys. Res. Lett.*, *23*, 2577–2580.

Gonzalez, W. D., B. T. Tsurutani, and A. de Gonzalez (1999), INTERPLANETARY ORIGIN OF GEOMAGNETIC STORMS, *Space Sci. Rev.*, *88*, 529–562.

Gosling, J. T., V. Pizzo, and S. J. Bame (1973), Anomalously Low Proton Temperature in the Solar Wind following Interplanetary Shock Waves-Evidence for Magnetic Bottles?, *J. Geophys. Res.*, *78*, 2001–2009.

Gosling, J. T., J. R. Asbridge, S. J. Bame, W. C. Feldman, and R. D. Zwickl (1980), Observations of large fluxes of he^+ in the solar wind following an interplanetary shock, *J. Geophys. Res.*, *85*.

Gosling, J. T., G. Borrini, J. R. Asbridge, S. J. Bame, W. C. Feldman, and R. T. Hansen (1981), CORONAL STREAMERS IN THE SOLAR-WIND AT 1-AU, *J. Geophys. Res.*, *86*, 5438 – 5448.

Gosling, J. T., D. N. Baker, S. J. Bame, W. C. Feldman, R. D. Zwickl, and E. J. Smith (1987), Bidirectional Solar Wind Electron Heat Flux Events, *J. Geophys. Res.*, *92*, 8519–8535.

Gosling, J. T., S. Eriksson, and R. Schwenn (2006), Petschek-type magnetic reconnection exhausts in the solar wind well inside 1 au: Helios, *J. Geophys. Res.*, *111*.

Green, J. C., T. G. Onsager, T. P. O'Brien, and D. N. Baker (2004), Testing loss mechanisms capable of rapidly depleting relativistic electron flux in the earth's outer radiation belt, *J. Geophys. Res.*, *109*, A12,211.

Guarnieri, F. L. (2005), A Study of the Interplanetary and Solar Origin of High Intensity Long Duration and Continuous Auroral Activity Events, *UNPE*.

Hada, T., and C. F. Kennel (1985), Nonlinear evolution of slow waves in the solar wind, *J. Geophys. Res.*, *90*, 531–535.

He, J.-S., E. Marsch, C.-Y. Tu, L.-J. Guo, and H. Tian (2010), Intermittent outflows at the edge of an active region - a possible source of the solar wind, *Astronomy & Astrophysics*, *516*, A14.

Heelis, R. A., et al. (2009), Behavior of the o+/h+ transition height during the extreme solar minimum of 2008, *Geophys. Res. Lett.*, *36*.

Henderson, M. G., G. D. Reeves, R. D. Belian, and J. S. Murphree (1996), Observation of magnetospheric substorms occurring with no apparent solar wind/IMF trigger, *J. Geophys. Res.*, *101*, 10,773–10,791.

Henke, T., J. Woch, R. Schwenn, U. Mall, G. Gloeckler, R. von Steiger, R. J. Forsyth, and A. Balogh (2001), Ionization state and magnetic topology of coronal mass ejections, *J. Geophys. Res.*, *106*, 10,597–10,613.

Heppner, J. P. (1955), Note on the occurrence of world-wide sscs during the onset of negative bays at college, alaska, *J. Geophys. Res.*, *60*, 29–32.

Hirshberg, J., and D. S. Colburn (1969), interplanetary field and geomagnetic variations - a unified view, *Planet. Space Sci.*, *17*, 1183–1206.

Hirshberg, J., S. J. Bame, and D. E. Robbins (1972), SOLAR FLARES AND SOLAR WIND HELIUM ENRICHMENTS: JULY 1965 - JULY 1967, *Sol. Phys.*, *23*, 467–486.

Hochedez, J.-F., A. Zhukov, E. Robbrecht, R. V. der Linden, D. Berghmans, P. Vanlommel, A. Theissen, and F. Clette (2005), Solar weather monitoring, *Ann. Geophys.*, *23*, 3149–3161.

Horwitz (1985), The substorm as an internal magnetospheric instability: Substorms and their characteristic time scales during intervals of steady interplanetary magnetic field, *J. Geophys. Res.*, *90*, 4164–4170.

Howard, T. (2011), *Interaction* W*ith the* E*arth and* O*ther* P*lanets: C*ontribution to* S*pace* W*eather*, vol. 376, 211-225 pp., Coronal Mass Ejections.

Hu, Q., and B. U. O. Sonnerup (2002), Reconstruction of magnetic clouds in the solar wind: Orientations and configurations, *J. Geophys. Res.*, *107*, 1142–1156.

Hundhausen, A. J., C. B. Sawyer, L. House, R. M. E. Illing, and W. J. Wagner (1984), Coronal Mass Ejections Observed during the Solar Maximum Mission - Latitude Distribution and Rate of Occurrence, *J. Geophys. Res.*, *89*, 2639–2646.

Huttunen, K. E. J., H. E. J. Koskinen, and R. Schwenn (2002), Variability of magnetospheric storms driven by different solar wind perturbations, *J. Geophys. Res.*, *107*, 201–208.

Jacobs, J. A., Y. Kato, S. Matsushita, and V. A. Troitskaya (1964), Classification of geomagnetic micropulsations, *J. Geophys. Res.*, *69*, 180–181.

Jian, L. K., C. Russell, J. G. Luhmann, and R. M. Skoug (2006a), PROPERTIES OF STREAM INTERACTIONS AT ONE AU DURING 1995-2004, *Sol. Phys.*, *239*, 337–392.

Jian, L. K., C. Russell, J. G. Luhmann, and R. M. Skoug (2006b), PROPERTIES OF INTERPLANETARY CORONAL MASS EJECTIONS AT ONE AU DURING 1995-2004, *Sol. Phys.*, *239*, 393–436.

Jin, M., et al. (2012), A GLOBAL TWO-TEMPERATURE CORONA AND INNER HELIOSPHERE MODEL: A COMPREHENSIVE VALIDATION STUDY, *The Astrophys. J.*, *745*.

Jurac, S., J. C. Kasper, J. D. Richardson, and A. J. Lazarus (2002), Geomagnetic disturbances and their relationship to Interplanetary shock parameters, *Geophys. Res. Lett.*, *29*, 7831–7839.

Kane, R. P. (2010a), Relationship between the geomagnetic Dst(min) and the interplanetary Bz(min) during cycle 23, *Planet. Space Sci.*, *58*, 392–400.

Kane, R. P. (2010b), Scatter in the plots of Dst(min) versus Bz(min), *Planet. Space Sci.*, *58*, 1792–1801.

Kavanagh, A., and M. Denton (2007), High-speed solar-wind streams and geospace interactions, *Ann. Geophys.*, *48*, 24–26.

Khrabrov, A. V., and B. U. O. Sonnerup (1998), *DeHoffmann-Teller analysis*, 221-248 pp., *Analysis Methos for Multi-Spacecraft Data*.

Kilpua, E. K. J., et al. (2009), Multispacecraft observations of magnetic clouds and their solar origins between 19 and 23 may 2007, *Sol. Phys.*, *254*, 325–344.

Kivelson, M. G., and C. T. Russell (1995), *Introduction to space physics*, Cambridge university press.

Klecker, B., et al. (2006a), Energetic particle observations, *Space Sci. Rev.*, *123*, 217–250.

Klecker, B., et al. (2006b), Energetic particle observations, *Space Sci. Rev.*, *123*, 217–250.

Ko, Y.-K., J. C. Raymond, T. H. Zurbuchen, P. Riley, J. M. Raines, and L. Strachan (2006), ABUNDANCE VARIATION AT THE VICINITY OF AN ACTIVE REGION AND THE CORONAL ORIGIN OF THE SLOW SOLAR WIND, *The Astrophys. J.*, *646*, 1275–1287.

Kojima, M., K. Fujiki, T. Ohmi, M. Tokumaru, A. Yokobe, and K. Hakamada (1999), Low-speed solar wind from the vicinity of solar active regions, *J. Geophys. Res.*, *104*, 16,993–17,003.

Kozyra, J. U., M. W. Liemohn, C. R. Clauer, A. J. Ridley, M. F. Thomsen, J. E. Borovsky, J. L. Roeder, V. K. Jordanova, and W. D. Gonzalez (2002), Multistep Dst development and ring current composition changes during the 46 June 1991 magnetic storm., *J. Geophys. Res.*, *107*.

Lepping, R. P., L. F. Burlaga, and J. A. Jones (1990), Magnetic field structure of interplanetary magnetic clouds at 1 AU, *J. Geophys. Res.*, *95*, 11,957–11,965.

Lepri, S. T., and T. H. Zurbuchen (2004), Iron charge distributions as an indicator of hot ICMEs: Possible sources and temporal and spatial variations during solar maximum, *J. Geophys. Res.*, *109*.

Lepri, S. T., T. H. Zurbuchen, L. A. Fisk, I. G. Richardson, H. V. Cane, and G. Gloeckler (2001), Iron charge distribution as an identifier of interplanetary coronal mass ejections, *J. Geophys. Res.*, *106*, 29,231–29,238.

Liemohn, M. W., J. U. Kozyra, M. F. Thomsen, J. L. Roeder, G. Lu, J. E. Borovsky, and T. E. Cayton (2001), The dominant role of the asymmetric ring current in producing the stormtime dst*, *J. Geophys. Res.*, *106*, 10,883.

Lindsay, G. M., C. T. Russell, and J. G. Luhmann (1995), Coronal mass ejection and stream interaction region characteristic and their potential geomagnetic effectiveness, *J. Geophys. Res.*, *10*, 16,999–17,013.

Lindsay, G. M., J. G. Luhmann, C. T. Russell, and J. T. Gosling (1999), Relationships between coronal mass ejection speeds from coronagraph images and interplanetary characteristics of associated interplanetary coronal mass ejections, *J. Geophys. Res.*, *104*, 12,515–12,523.

Liou, K., C.-C. Wu, D. Murray, S.-T. Wu, N. Rich, S. Plunkett, L. Simpson, C. D. Fry, and K. Schenk (2014), Global simulation of extremely fast coronal mass ejection on 23 july 2012, *Journal of Atmospheric and Solar-Terrestrial Physics.*, *121*, 32–41.

Liu, Y., J. D. Richardson, and J. W. Belcher (2005), A statistical study of the properties of interplanetary coronal mass ejections from 0.3 to 5.4 AU, *Planet. Space Sci.*, *53*, 3–17.

Lopez, R. E., M. Wiltberger, S. Hernandez, and J. G. Lyon (2004), Solar wind density control of energy transfer to the magnetosphere, *Geophys. Res. Lett.*, *31*.

Low, B. C. (1996), Solar activity and the corona (invited review), *Sol. Phys.*, *167*, 217–265.

Lugaz, N., and I. I. Roussev (2011), Numerical modeling of interplanetary coronal mass ejections and comparison with heliospheric images, *Journal of Atmospheric and Solar-Terrestrial Physics.*, *73*, 1187–1200.

Lyons, L. R. (1995), A new theory for magnetospheric substorms, *J. Geophys. Res.*, *100*, 19,069–19,081.

Lyons, L. R. (1996), Substorms: Fundamental observational features, distinction from other disturbances, and external triggering, *J. Geophys. Res.*, *101*, 13,011–13,026.

Manchester, W., T. Gombosi, I. Roussev, A. Ridley, D. Zeeuw, I. Sokolov, K. Powell, and G. Toth (2004), Modeling a space weather event from the Sun to the Earth: CME generation and interplanetary propagation, *J. Geophys. Res.*, *109*.

Marsch, E., and C.-Y. Tu (1990), Spectral and Spatial Evolution of Compressible Turbulence in the Inner Solar Wind, *J. Geophys. Res.*, *95*, 11,945–11,956.

Mason, G. M., M. I. Desai, U. Mall, A. Korth, R. Bucik, T. T. von Rosenvinge, and K. D. Simunac (2009), *In situ* Observations of CIRs on STEREO, *textscwind*, and ACE During 2007 - 2008, *Sol. Phys.*, *256*, 393 – 408.

Matthaeus, W. H., and M. L. Goldstein (1982), Measurement of the Rugged Invariants of Magnetohydrodynamic Turbulence in the Solar Wind, *J. Geophys. Res.*, *87*, 6011–6028.

McComas, D. J., B. E. Goldstein, J. T. Gosling, and R. M. Skoug (2001), Ulysses' Second Orbit: Remarkably Different Solar Wind, *Space Sci. Rev.*, *97*, 99–103.

McComas, D. J., et al. (2000), Solar wind observations over ulysses' first full polar orbit, *J. Geophys. Res.*, *105*, 10,419–10,433.

McIntosh, S. W., B. D. Pontieu, M. Carlsson, V. Hansteen, P. Boerner, and M. Goossens (2011), Alfvénic waves with sufficient energy to power the quiet solar corona and fast solar wind, *Nature*, *475*, 477–480.

McPherron, R. L., and G. Siscoe (2004), Probabilistc forecasting of geomagnetic indices using solar wind air mass analysis, *Space Weather*, *2*.

Moldwin, M. B., S. Ford, R. Lepping, J. Slavin, and A. Szabo (2000), Small-scale magnetic flux ropes in the solar wind, *Geophys. Res. Lett.*, *27*, 57–60.

Montgomery, M. D., J. R. Asbridge, S. J. Bame, and W. C. Feldman (1974), Solar wind electron temperature depressions following some interplanetary shock waves: Evidence for magnetic merging?, *J. Geophys. Res.*, *69*, 3103–3110.

Neugebauer, M., and C. W. Snyder (1966), Mariner 2 Observations of the Solar Wind 1. Average Properties, *J. Geophys. Res.*, *71*, 4469–4484.

Newell, P. T., T. Sotirelis, K. Liou, C.-I. Meng, and F. J. Rich (2007), A nearly universal solar windmagnetosphere coupling function inferred from 10 magnetospheric state variables, *J. Geophys. Res.*, *112*.

O'Brien, T. P., and R. L. McPherron (2000), An empirical phase space analysis of ring current dynamics: Solar wind control of injection and decay, *J. Geophys. Res.*, *105*.

O'Brien, T. P., R. L. McPherron, and D. Sornette (2001), Which magnetic storms produce relativistic electrons at geosynchronous orbit, *J. Geophys. Res.*, *106*, 15,533–15,544.

Odstrcil, D., V. Pizzo, and C. Arge (2005), Propagation of the 12 May 1997 interplanetary coronal mass ejection in evolving solar wind structures, *J. Geophys. Res.*, *110*.

Owens, M. J., T. S. Horbury, R. T. Wicks, S. L. McGregor, N. P. Savani, and M. Xiong (2014), Ensemble downscaling in coupled solar wind-magnetosphere modeling for space weather forecasting, *Space Weather*, *12*, doi:10.1002/2014SW001,064.

Palmroth, M., T. I. Pulkkinen, P. Janhunen, and C.-C. Wu (2003), Stormtime energy transfer in global MHD simulation, *J. Geophys. Res.*, *108*(A1).

Parker, E. N. (1958), Dynamics of the Interplanetary Gas and Magnetic Fields, *The Astrophys. J.*, *128*, 664.

Parker, E. N. (1965), Dynamical theory of the solar wind, *Space Sci. Rev.*, *4*, 666–708.

Prestes, A., N. R. Rigozo, E. Echer, and L. E. A. Vieira (2006), Spectral analysis of sunspot number and geomagnetic indices (1868-2001), *Journal of Atmospheric and Solar-Terrestrial Physics.*, *68*, 182–190.

Pulkkinen, T. I., M. Palmroth, E. I. Tanskanen, P. Janhunen, H. E. J. Koskinen, and T. V. Laitinen (2006), New interpretation of magnetospheric energy circulation, *Geophys. Res. Lett.*, *33*.

Ragot, B. R. (2006), DISTRIBUTION OF MAGNETIC FIELD ORIENTATIONS IN THE TURBULENT SOLAR WIND, *The Astrophys. J.*, *651*, 1209–1218.

Rathore, B. S., S. C. Kaushik, R. S. Bhadorin, K. K. Parashar, and D. C. Gupta (2012), Sunspots and geomagnetic storms during solar cycle-23, *Indian J. Phys.*, *86*, 563–567.

Richardson, I. G., and H. V. Cane (1995), Regions of abnormally low proton temperature in the solar wind (1965-1991) and their association with ejecta, *J. Geophys. Res.*, *100*, 23,397–23,412.

Richardson, I. G., and H. V. Cane (2010), Near-earth Interplanetary Coronal Mass Ejections During Solar Cycle 23 (1996 - 2009): Catalog and Summary of Properties, *Sol. Phys.*, *264*, 189–237.

Richardson, I. G., G. Wibberenz, and H. V. Cane (1996), The relationship between recurring cosmic ray depressions and corotating solar wind streams at <=1 AU: IMP 8 and Helios 1 and 2 anticoincidence guard rate observation, *J. Geophys. Res.*, *101*, 13,483–13,496.

Richardson, I. G., J. E. Mazur, and G. M. Mason (1998), A comparison of recurrent energetic ion enhancements observed at Ulysses and at 1 AU by IMP 8 and SAMPEX: Ulysses launch until following the first north polar passage, *J. Geophys. Res.*, *103*, 2115–2129.

Rosenberg, R. L., and J. P. J. Coleman (1980), Solar cycle-dependent north-south field configurations observed in solar wind interaction regions, *J. Geophys. Res.*, *85*, 3021–3032.

Rouillard, A., et al. (2009), A Multispacecraft Analysis of a Small-Scale Transient Entrained by Solar Wind Streams, *Sol. Phys.*, *256*, 307–326.

Russell, C. T., J. G. Luhmann, and L. K. Jian (2010), How unprecedented a solar minimum?, *Rev. Geophys.*, *48*, RG2004.

Sahraoui, F., M. L. Goldstein, P. Robert, and Y. V. Khotyaintsev (2009), Evidence of a Cascade and Dissipation of Solar-Wind Turbulence at the Electron Gyroscale, *Physical Review Letter*, *102*, 231,102.

Sakao, T., et al. (2007), Continuous Plasma Outflows from the Edge of a Solar Active Region as a Possible Source of Solar Wind, *Science*, *318*, 1585–1588.

Samson, J. C., and K. L. Yeung (1986), Some generalizations on the method of superposed epoch analysis, *Planet. Space Sci.*, *34*, 1133–1142.

Sanny, J., J. A. Tapia, D. G. Sibeck, and M. B. Moldwin (2002), Quiet time variability of the geosynchronous magnetic field and its response to the solar wind, *J. Geophys. Res.*, *107*.

Sanny, J., D. Judnick, M. B. Moldwin, D. Berube, and D. G. Sibeck (2007), Global profiles of compressional ultraslow frequency wave power at geosynchronous orbit and their response to the solar wind, *J. Geophys. Res.*, *112*.

Schwadron, N. A., and D. J. McComas (2004), The Sheared Sub-Parker Spiral, AGU F*all* M*eeting*, *Abstracts*.

Schwadron, N. A., D. J. McComas, H. A. Elliott, G. Gloeckler, J. Geiss, and R. von Steiger (2005), Solar wind from the coronal hole boundaries, *J. Geophys. Res.*, *110*.

Schwenn, R. (1996), An essay on terminology, myths, and known facts: Solar transient, flare, cme, driver gas, piston, bde, magnetic cloud, shock wave, geomagnetic storm, *Astropysics and Space Science*, *243*, 187–193.

Schwenn, R., H. Rosenbauer, and K.-H. M'uhlh'auser (1980), Singly-ionized helium in the driver gas of an interplanetary shock wave, *Geophys. Res. Lett.*, *7*, 201–204.

Schwenn, R., A. D. L. E. Huttunen, and W. D. Gonzalez (2005), The association of coronal mass ejections with their effects near the Earth, *Ann. Geophys.*, *23*, 1033–1059.

Sergeev, V. A., D. A. Sormakov, and V. Angelopoulos (2014), A missing variable in solar wind-magnetosphere-ionosphere coupling studies, *Geophys. Res. Lett.*, *41*, 8215–8220.

Sheeley, J. N. R., J. W. Harvey, and W. C. Feldman (1976), CORONAL HOLES, SOLAR WIND STREAMS, AND RECURRENT GEOMAGNETIC DISTURBANCES: 1973-1976, *Sol. Phys.*, *49*, 271–278.

Shen, F., X. Feng, S. Wu, C. Xiang, and W. Song (2011), Three-dimensional MHD simulation of the evolution of the April 2000 CME event and its induced shocks using a magnetized plasma blob model, *J. Geophys. Res.*, *116*, A04,102.

Shen, F., C. Shen, J. Zhang, P. Hess, Y. Wang, X. Feng, H. Cheng, and Y. Yang (2014), Evolution of the 12 July 2012 CME from the Sun to the Earth: Data-constrained three-dimensional MHD simulations, *J. Geophys. Res.*, *119*.

Singer, H. J. (1996), Monitoring space weather with the goes magnetometers, *Proc. SPIE*, *2812*, 299–308.

Skoug, R. M., J. T. Gosling, J. T. Steinberg, D. J. McComas, C. W. Smith, N. F. Ness, Q. Hu, and L. F. Burlaga (2004), Extremely high speed solar wind: 29-30 october 2003, *J. Geophys. Res.*, *109*.

Smith, E. J., and J. H. Wolf (1976), Observations of interaction regions and corotating shocks between one and five au pioneers 10 and 11, *Geophys. Res. Lett.*, *3*, 137.

Snekvik, K., E. Tanskanen, E. Kilpua, and D. Pérez-Suárez (2013), Alfvénic intervals in the solar wind at 1 AU 1995-2011, *Geophysical Research Abstracts*, *15*.

Sonnerup, B. U. O., and M. Scheible (1998), *Minimum and Mmaximum Vvariance Aanalysis*, 185-220 pp., *Analysis Methos for Multi-Spacecraft Data*.

Sonnerup, B. U. O., H. Hasegawa, W.-L. Teh, and L.-N. Hau (2006), Grad-Shafranov reconstruction: An overview, *J. Geophys. Res.*, *111*.

Stewart, B. (1861), On the great magnetic disturbance which extended from August 2 to september 7, 1859 as recorded by photography at the Kew Observatory, *Phil. Trans. Roy. Soc. Lond.*, *11*.

Takahashi, K., and A. Y. Ukhorskiy (2008), Timing analysis of the relationship between solar wind parameters and geosynchronous pc5 amplitude, *J. Geophys. Res.*, *113*, A12,204.

Takahashi, K., R. W. McEntire, A. T. Y. Lui, and T. A. Potemra (1990), Ion flux oscillations associated with a radially polarized transverse Pc 5 magnetic pulsation, *J. Geophys. Res.*, *95*, 3717–3731.

Tian, H., Y. Shuo, Q.-G. Zong, J.-S. He, and Q. Yu (2010), Signatures of magnetic reconnectionat boundaries of interplanetary small-scale magnetic flux ropes, *The Astrophys. J.*, *720*, 454–464.

Tóth, G., D. L. D. Zeeuw, T. I. Gombosi, W. B. Manchester, A. J. Ridley, I. V. Sokolov, and I. I. Roussev (2007), Sun-to-thermosphere simulation of the 28-30 october 2003 storm with the space weather modeling framework, *Space Weather*, *5*.

Tsurutani, B. T. (2000), *Solar/interplanetary plasma phenomena causing geomagnetic activity at Earth*, 273+ pp., Proc. International School of Physics "Enrico Fermi" Course CXLII.

Tsurutani, B. T., and W. D. Gonzalez (1987), The cause of high intensity long-duration continuous *AE* activity (HILDCAAs): Interplanetary Alfvén wave trains, *Planet. Space Sci.*, *35*, 405–412.

Tsurutani, B. T., W. D. Gonzalez, Y. Kamide, and J. K. Arballo (2013), The Interplanetary Causes of Magnetic Storms: A Review, in Magnetic Storms (eds B. T. Tsurutani, W. D. Gonzalez, Y. Kamide and J. K. Arballo), *American Geophysical Union*.

Tsurutani, B. T., et al. (2006), Corotating solar wind streams and recurrent geomagnetic activity: A review, *J. Geophys. Res.*, *11*, A07S01.

Tu, C.-Y., and E. Marsch (1993), A Model of Solar Wind FLUCTUATIONS With Two Components: Alfvén Waves and Convective Structures, *J. Geophys. Res.*, *98*, 1257–1276.

Tu, C.-Y., and E. Marsch (1995), MHD structures, waves and turbulence in the solar wind: Oobservations and theories, *Space Sci. Rev.*, *73*, 1–210.

Unti, T. W. J., and M. Neugebauer (1968), Alfvén Waves in the Solar Wind, *Phys. F*luids, *11*.

Vasquez, B. J., V. I. Abramenko, D. K. Haggerty, and C. W. Smith (2007), Numerous small magnetic field discontinuities of bartels rotation 2286 and the potential role of Alfvénic turbulence, *J. Geophys. Res.*, *112*, A11,102.

Vassiliadis, D., I. R. Mann, S. F. Fung, and X. Shao (2007), Ground Pc3Pc5 wave power distribution and response to solar wind velocity variations, *Planet. Space Sci.*, *55*, 743–854.

Vrsnak, B., M. Temmer, and A. M. Veronig (2007), Coronal Holes and Solar Wind High-Speed Streams: I. Forecasting the Solar Wind Parameters, *Sol. Phys.*, *240*, 315–330.

Wang, C., D. Du, and J. D. Richardson (2005), Characteristics of the interplanetary coronal mass ejections in the heliosphere between 0.3 and 5.4 AU, *J. Geophys. Res.*, *110*.

Wang, Y. M., N. R. Sheeley, D. G. Socker, R. A. Howard, and N. B. Rich (2000), The dynamical nature of coronal streamers, *J. Geophys. Res.*, *105*, 25,133–25,142.

Watermann, J., G. S. Bust, J. P. Thayer, T. Neubert, and C. Coker (2009a), Models of Solar Wind Structures and Their Interaction with the Earths Space Environment, *Space Sci. Rev.*, *147*, 233–270.

Watermann, J., R. Vainio, J. Lilensten, A. Belehaki, and M. Messerotti (2009b), The State of Space Weather Scientific ModelingAn Introduction, *Space Sci. Rev.*, *147*, 111–120.

Weigel, R. S., T. Detman, E. J. Rigler, and D. N. Baker (2006), Decision theory and the analysis of rare event space weather forecasts, *Space Weather*, *4*.

Whang, Y. C., D. Larson, R. P. Lin, R. P. Lepping, and A. Szabo (1998), Plasma and magnetic field structure of a slow shock: Wind observations in interplanetary space, *Geophys. Res. Lett.*, *25*, 2625–2628.

Wu, C.-C., C. Fry, S. Wu, M. Dryer, and K. Liou (2007), Three-dimensional global simulation of ICME propagation from the Sun to the heliosphere: 12 May 1997 solar event, *J. Geophys. Res.*, *112*, A09,104.

Yermolaev, Y. I., I. G. Lodkina, N. S. Nikolaeva, and M. Y. Yermolaev (2011), Statistical study of interplanetary condition effect on geomagnetic storms: 2. Variations of parameters, *Cosmic Research*, *49*, 21–34.

Zhang, X.-Y., and M. B. Moldwin (2014), The source, statistical properties and geoe ffectiveness of long-duration southward interplanetary magnetic field intervals, *J. Geophys. Res.*, *119*, 658–669.

Zhang, X.-Y., M. B. Moldwin, and M. Cartwright (2012), The geo-effectiveness of interplanetary small-scale magnetic flux ropes, *Journal of Atmospheric and Solar-Terrestrial Physics.*, *95-96*, 1–14.

Zhang, X.-Y., M. B. Moldwin, J. T. Steinberg, and R. M. Skoug (2014), Alfvén waves as a possible source of long-duration, large-amplitude, and geoeffective southward imf, *J. Geophys. Res.*, pp. 3259–3266.

Zhao, L., T. H. Zurbuchen, and L. A. Fisk (2009), Global distribution of the solar wind during solar cycle 23: ACE observations, *Geophys. Res. Lett.*

Zhou, X., and B. T. Tsurutani (2001), Interplanetary shock triggering of nightside geomagnetic activity: Substorms, pseudobreakups, and quiescent events, *J. Geophys. Res.*, *106*, 18,957–18,967.

Zong, Q.-G., et al. (2007), Ultralow frequency modulation of energetic particles in the dayside magnetosphere, *Geophys. Res. Lett.*, *34*, L12,105.

Zurbuchen, T. H., and I. G. Richardson (2006), In-Situ Solar Wind and Magnetic Field Signature of Interplanetary Coronal Mass Ejections, *Space Sci. Rev.*, *123*, 31–43.

Zurbuchen, T. H., et al. (2000), On the origin of microscale magnetic holes in the solar wind, *J. Geophys. Res.*, *106*, 16,001–16,010.

Zwickl, R. D., J. R. Asbridge, S. J. Bame, W. C. Feldman, J. T. Gosling, and E. J. Smith (1983), Plasma properties of driver gas following interplanetary shocks observed by ISEE-3, *in Solar Wind Five, edited by M. Neugebauer,* NASA Conf. Publ., *2280*, 711.